# Ready For Take-off: Scaled Flight Testing

## An investigation into influence of scaling on the aerodynamic properties

J.J. van Gorcum

April 2017

Delft University of Technology


TU Delft Delft University of Technology

Challenge the future

# PREFACE

Looking back on my years in Delft, I can look back to a fantastic time. During the past years I have had the opportunity to develop various different skills, both as an engineer and on other levels. I can honestly say that I have had many unique experiences that I will remember the rest of my life.

First of all, I want to thank my supervisors prof.dr.ir. Leo Veldhuis and ir. Nando van Arnhem for helping stay on the right track and provide feedback where and when needed.

Next, I want to thank my parents and family, for supporting me to pursue not only this challenging study but also many extra-curricular activities. I want to thank my girlfriend for the additional support she gave my throughout my graduation project. I also want to thank my friends; those that I had when I started and those who I met along the way, for sharing all these great experiences with me. Last but not least, I want to thank my friends of my 'afstudeerkamer' and the friends (Rob, Morten and Stefan) who have helped me with my thesis, by either giving me new insights or reading it.

*Delft, 10 April 2017*

The cover illustration is of the NASA PTERA Scaled Flight Testing Model, from NASA Photos `https://www.nasa.gov/sites/default/files/thumbnails/image/ed15-325-20.jpg`

# ABSTRACT

Atmospheric free flight scaled flight testing is an affordable way to investigate the dynamic properties of an aircraft, while enabling a wider range of test possibilities than a windtunnel. Worldwide several different scaled flight testing programs exist, most with a focus on dynamic flight testing. It is known that scaling has an effect on the flow properties and thus the aerodynamic properties. This can be important when new aircraft configurations are tested, for example a new tail configuration. This research is the first step into the development of a scaled flight testing model and as such will highlighted the difficulties and discrepancies which will be faced when scaling is performed. This study has the objective of investigating the effect of scaling on the aerodynamic properties and of the flow field at the tail location, with the focus on take-off conditions.

The full scale case is a regional aircraft, the ATR72, with an unswept and slightly tapered wing. The scaled case is 14.7% geometric scaled. Froude and dynamic scaling determine the velocity and masses. The scale factor was decided on by a maximum wing span, which still allows the model to be manageable in operations. A distinction is made between the clean wing and the wing with flap. The wing with flap includes a 15° slotted Fowler flap.

The analysis of the aerodynamic properties is split between the clean wing and the wing with an additional surface in the form of a flap. The aerodynamic properties investigated were the lift, moment and drag curve, and the maximum lift coefficient. The clean wing was analysed using a quasi-3D analysis called Q3D, which is a combination of a vortex-lattice method (AVL) and a vortex panel method (XFOIL). A modification of XFOIL, called RFOIL, is used to analyse the difference in maximum lift coefficient between the airfoil of the scaled and full scale case. RFOIL is selected because of the better results near stall. The wing with flap is investigated using a vortex lattice method, in this case again AVL, where the airfoil with flap is investigated using the Euler-solver MSES. Finally the maximum lift coefficient for the wing with flap is analysed with the semi-empirical Pressure Difference Rule. The Pressure Difference Rule states that there is a ratio between the peak pressure and the trailing edge pressure, on a surface, at which maximum lift occurs. The methods are limited in their incorporation of viscous effects, the 2D-analysis tools (XFOIL, RFOIL and MSES) only include viscous effects in the small boundary layer region. AVL does not include viscous effects directly, but only via a correction factor for the lift-curve slope. However, the results found in literature using these methods are satisfactory.

An analysis of the wake field is done using methods developed by the ESDU. The wake properties of both the scaled as well as the full scale are calculated using semi-empirical models and use a simplification where to place the vortex sheet. The dimensions and velocity loss of the wake itself can be calculated using either a method by ESDU or a method by Schlichting. Results showed that both these methods provided similar solutions.

The scaling of the wing proves to change the aerodynamic properties and the similarity is no longer present for all the investigated aerodynamic properties. For both the wing with and without flap this is the case. The clean wing shows a difference for the lift coefficient of up to 60% with respect to the full scale wing for equal angle of attack, the moment coefficient is off by up to 30%. The drag coefficient of the clean wing shows difference up to 73% with respect to the full scale wing for a fixed lift coefficient. The 2D maximum lift coefficient is reduced by 33%. The wing with flap shows a difference in lift coefficient, for fixed angle of attack, of up to 37% and the lift distribution tends towards more outboard loading. The maximum lift of the wing with flap sees a reduction of approximately 29%. These differences are mainly due to Reynolds number effects, the Mach number effects are only minimal on the lift coefficient. Due to the limits on the selected methods the exact magnitude of the difference found can not be guaranteed, but the trends in the found differences are certain.

A basis for this is found in the different boundary layer properties, the scaled wing exhibits a thicker boundary layer, leading to a decambering effect, and laminar separation bubbles are found to occur. Both the clean and wing with flap shows more outboard loading for the scaled wing.

The scaled wing exhibits a thicker wake, with a larger velocity loss. The wake of the scaled wing is 46% wider than the full scale case and has a 32% higher velocity deficit. The scaled wing with flap shows an increase of 14% in the wake thickness and 19% in velocity deficit. The difference between the full and scaled

clean wing is thus larger than the difference between the full and scaled wing with flap. The reason for difference between the full and scaled wing can be found in the increased drag (coefficient) of the scaled wing. The reason behind the larger increase in wake for the clean wing is due to the fact that the difference in drag coefficient between the full and scaled case is larger for the clean wing than for the wing with flap.

An investigation to minimize the differences between the full and scaled wing is done. It is decided to change the airfoil shape. Due to the numerical difficulties that are found when using the tools for the wing with flap, this optimization is only performed on the clean wing. The input of the optimization is the shape of the airfoil, which is parameterized using the Class/Shape Transformation (CST). The objective is based on the differences between the full scale and scaled values for the lift, moment and drag coefficient at two different angles of attack. The optimization is performed using a combination of a genetic algorithm, in order to fully capture the whole design space, and a SQP-algorithm in order to ensure a (local) minimum. Besides the airfoil shape alteration the wing is also given an incidence angle, in order to reduce the differences found.

Improvements are visible for the optimized airfoil, on all the aerodynamic properties. Difference between the full and scaled case are reduced to a maximum of 11% for lift coefficient and 5.5% for moment coefficient, at a fixed angle of attack. The 2D maximum lift coefficient is improved by 22% compared to the scaled case. The optimized airfoil shapes tends towards a thinner airfoil and thus an investigation into solely optimizing the thickness of the airfoil is also done. This also proves to give better results than the original airfoil, however, not as good as the shape optimized airfoils. It showed a slight improvement for the lift and moment coefficients. The maximum lift coefficient was improved by only 5%. This thinner profile was also investigated in the configuration with a flap, but here it proved to decrease the performance of the airfoil with flap.

The difference between the full and scaled case can be reduced by an optimization. If an optimization is to be done, it must be done on the whole of configurations and flight conditions. As the next step into a development of a scaled flight test model, the exact extend of tests must be determined, only then can it be investigated how scaling affects the results of testing. No direct solutions exist to completely overcome the gap between the full and scaled aerodynamic properties of a flight testing model, however airfoil shape optimization does provide a better similarity.

# CONTENTS

# LIST OF FIGURES

# LIST OF TABLES

# NOMENCLATURE

## LATIN SYMBOLS

| | | |
|---|---|---|
| a | Speed of sound | [m/s] |
| AR | Aspect ratio | [-] |
| b | Wake width | [m] |
| c | Chord | [m] |
| $\overline{c}$ | Mean Aerodynamic Chord | [m] |
| $C_D$ | Drag coefficient, 3D | [-] |
| $c_d$ | Drag coefficient, 2D | [-] |
| $c_f$ | Friction coefficient | [-] |
| $C_L$ | Lift coefficient, 3D | [-] |
| $c_l$ | Lift coefficient, 2D | [-] |
| $C_M$ | Moment coefficient, 3D | [-] |
| $c_m$ | Moment coefficient, 2D | [-] |
| $C_p$ | Pressure coefficient | [-] |
| FR | Froude number | [-] |
| g | Gravitational acceleration | $[m/s^2]$ |
| h | height | [m] |
| I | Inertia | $[kgm^2]$ |
| l | length | [m] |
| L | Lift | [N] |
| m | Mass | [kg] |
| M | Mach number | [-] |
| n | Scaling factor | [-] |
| q | Dynamic pressure | $[N/m^2]$ |
| r | Distance | [m] |
| Re | Reynolds number | [-] |
| S | Surface area | $[m^2]$ |
| s | Semi-span | [m] |
| V | Velocity | $[m/s]$ |
| W | Weight | [N] |
| w | Body width | [m] |
| x | x-coordinate | [m] |
| y | y-coordinate | [m] |
| z | z-coordinate | [m] |

## GREEK SYMBOLS

| | | |
|---|---|---|
| $\alpha$ | Angle of attack | [degree] |
| $\delta$ | Boundary layer thickness | [-] |
| $\delta^*$ | Displacement thickness | [-] |
| $\epsilon$ | Downwash angle | [degree] |
| $\eta$ | Normalized y-coordinate | [-] |
| $\Gamma$ | Vortex strength | $[m^2/s]$ |
| $\gamma$ | Vortex strength per unit length | $[m/s]$ |
| $\Lambda$ | Sweep angle | [degree] |
| $\lambda$ | Taper ratio | [-] |
| $\nu$ | Kinematic viscosity | $[m^2/s]$ |
| $\phi$ | Velocity potential | [-] |

| | | |
|---|---|---|
| $\rho$ | Air density | $[kg/m^3]$ |
| $\theta$ | Momentum thickness | [-] |
| $\xi$ | Normalized x-coordinate | [-] |
| $\zeta$ | Normalized z-coordinate | [-] |

## SUBSCRIPTS

| | |
|---|---|
| 0 | Zero-lift |
| F | Full Scale |
| f | Flap |
| h | Horizontal tail |
| M | Model |

# 1

# INTRODUCTION

With the advent of new aircraft configurations, such as body mounted ducted fans, wind tunnels alone do not suffice as a proof-of-concept. Wind tunnels are limited in their space for doing free flight testing. Doing tests with a large aircraft, the size of a full airliner, comes with great risk, not only a financial risk but also health and safety risks. Scaled flight testing, with unmanned remote piloted vehicles can fill the gap between wind tunnel and full scale testing. This chapter will start by giving the motivation for scaled flight testing, followed by some issues encountered when scaling is performed. Then the research objective and the corresponding research questions are posed. After that an overview of some examples of scaled flight test models are given. Finally, the chapter is concluded by setting the scope for the current study and giving an outlook on the rest of the thesis.

## 1.1. MOTIVATION

Scaled flight testing is an affordable way to test novel technologies in conditions analogous to the full-scale, real life application. When comparing scaled flight testing to wind tunnel tests or full-scale tests, each have their own advantages and disadvantages. It can be said that wind tunnel and sub scale free flight testing complement each other [1].

Compared to full scale testing, scaled free flight testing seems to provide an advantage in both safety and economic sense. As the scaled flight testing model is unmanned human lives are not directly at risk, when testing high risk novel technologies and procedures [2].

Whereas a scaled flight testing campaign may cost in the order of of $100,000, the full-scale testing program can cost up to $ 100 million [3]. Also the time-span in which these test programs can be realized is much shorter for scaled flight testing, months compared to years.

Figure 1.1 shows a comparison between different testing techniques, on five different grading scales, for flight dynamics research. Here IEP denotes the Innovative Evaluation Platform (see Section 1.3.4), which is a scaled flight testing model, SACSO is an active suspension technique, used in a wind tunnel, and B20 is a small scale flight test facility. Both the B20 and SACSO are operated by ONERA, the French aerospace laboratory [4]. Of main interest here is the comparison between the IEP, Wind Tunnel and Full Scale Aircraft. As expected, the full scale aircraft is the best in technical performance, but the costs are significant. For this comparison the IEP outperforms the wind tunnel mainly on costs, but shows some worse performance in operability. Overall the small scale aircraft here is expected to deliver (slightly) better technical results at a lower cost than the wind tunnel.

The aforementioned advantages is what piqued the interest of the faculty of Aerospace Engineering at the Delft University of Technology (DUT), to start an investigation into the development of their own scaled flight testing model.

## 1.2. EFFECT OF SCALING ON AERODYNAMIC PROPERTIES

With the change in size of scaled flight testing model also come different flight conditions, the velocity and altitude at which the model flies will be different. This can be due to regulations or operational limits. The change in flight conditions cause a change in the flow properties at which the model operates. Interesting quantities to look at in this regard are the Reynolds and Mach number. Both are dimensionless quantities

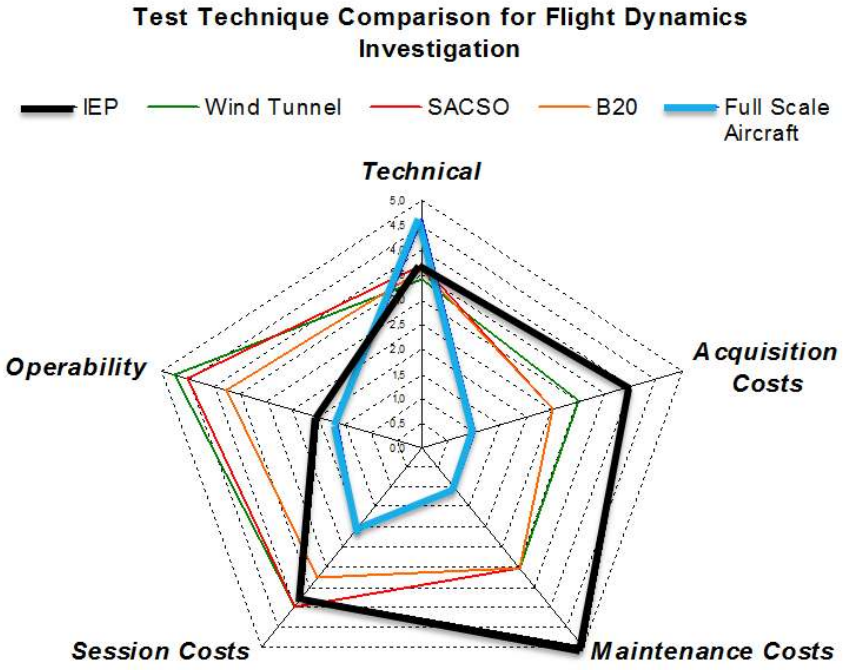


Figure 1.1: Comparison of different testing techniques on five different criteria [4]

that describe the state of the flow, making them relevant for comparison across various scales. The Reynolds number relates the ratio of inertia to viscous forces. The Mach number is the ratio between the velocity of the object and the velocity of sound in the medium.

Figure 1.2 shows the influence of different flow conditions on the dimensionless aerodynamic properties of a wing, such as lift ($C_L$) and drag ($C_D$) coefficient. With a change in the flow conditions, as indicated by the Reynolds number, the aerodynamic properties shown here are not constants. For the Mach number the aerodynamic coefficients are neither constant, as will be discussed in Section 2.2. The difference in lift, drag and moment coefficient will have an influence on the flight performance of the scaled aircraft, when compared to the full scale aircraft. When looking at the graphs in Figure 1.2 it is visible that the maximum lift of a scaled aircraft will be different and thus that tests involving maximum lift will produce different results. Figure 1.2b indicates that an aircraft at smaller scale will experience a higher drag coefficient and thus will need more thrust. This difference will be distinct for each combination of wing and scale factor. Many of the mentioned scaled flight testing models, from the coming section, are used for flight dynamics testing, however, little research is known into the aerodynamic properties of these models. Most studies only take geometric and dynamic scaling into account.

Figure 1.2c shows the effects of Mach on the 2D lift coefficient, until a certain Mach number, 0.85 in this case, the lift coefficient increases.

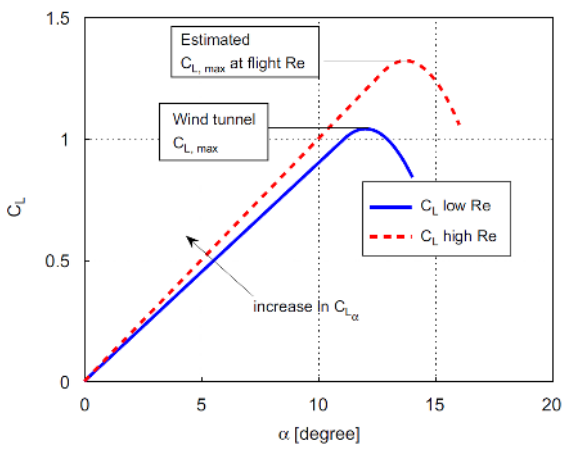


(a) Effect of Reynolds Number on lift coefficient [5]

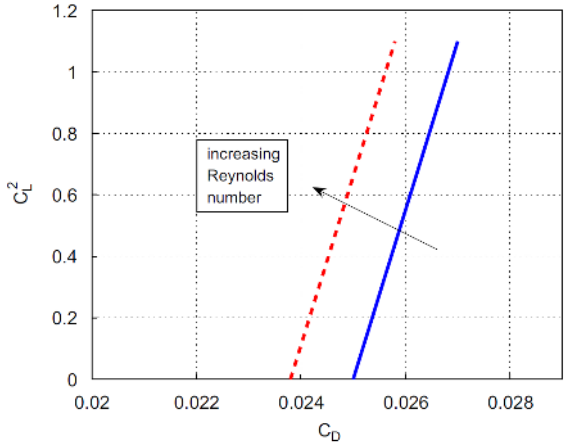


(b) Effect of Reynolds Number on drag coefficient [5]

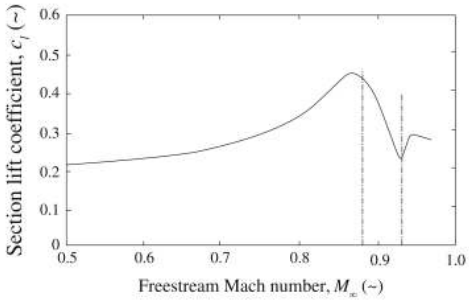


(c) Effect of Mach Number on lift coefficient [6]

Figure 1.2: Effect of Reynolds and Mach number on lift and drag coefficients

## 1.3. HISTORY AND EXAMPLES OF SCALED FLIGHT TESTING

Scaled flight testing is not a new technique, however in recent years it has seen an increase in activity, due to the reduction in size of the sensor and control equipment. Worldwide several different scaled free-flight testing models have been developed, with different program goals. A distinction can be made between directly scaling an aircraft for a sub scale model or having a subscale technology demonstrator. For both these types examples are discussed in the subsections below.

### 1.3.1. BRIEF HISTORY OF FREE-FLIGHT TESTING

Scaled free-flight testing is not a novel testing technique, it has been a practice dating back to (before) 1927, when NACA wrote (one of the) first articles on dynamically scaled flight testing [7]. Dynamic scaling entails getting properties important for dynamic response of an aircraft, the same for the full and scaled case. These properties are usually the masses and inertias. The emphasis here was still on doing unpowered tests on dropped models, in order to predict the performance of airplane models. The paper described correct mass and center of gravity representation. In the late 1920s and 1930s free-flight testing was initially done with the intent of understanding tailspin better, which was done in hangars. After the space in these hangars turned out to be too limited, the spin research was relocated to vertical windtunnels.

In the 1950s outdoor drop model tests were resumed, with more sophisticated models which now included remote control for the control surfaces. However, due to the inherent quicker reaction times of smaller vehicles, several pilots were required for the control; one for pitch, one for yaw and one for roll. In the 1960s this capability was expanded with powered free-flight models. Since the 1970s NASA expanded their testing facilities to also include powered free flight models, which is still being done to this day.

With the improvement of measuring and control equipment, due to the decrease in size of such electronics, scaled flight testing has in recent years become more attractive as a link between windtunnel testing and full-scale testing [1].

### 1.3.2. AIRSTAR

The Airborne Subscale Transport Aircraft Research (AirSTAR) is an unmanned 5.5% dynamically scaled aircraft, by NASA Langley Research Center [8]. It is based on the generic transport model (GTM), which is a concept transport aircraft, to which the AirSTAR will be compared. The dimensions of both the GTM and the AirSTAR can be found in Table 1.1. Two models were made, the T1 and the T2. Both the models have the properties as in Table 1.1, however the T2 had a lighter airframe, which allowed for more flexibility in the onboard measuring equipment. An image of the AirSTAR is shown in Figure 1.3. The main goal of the AirSTAR program is to test in-flight control upset prevention & recovery, this is why the correct dynamically scaling of the inertias and masses is very important.

The aircraft is piloted from a dedicated mobile operations station (truck) and has flown on a remote airstrip, within visual range [9]. The flight computer, which has all the control algorithms, is left on the ground in the mobile operating station, this allows for quickly implementing new algorithms in operational conditions [2].

Table 1.1: Data for the GTM and the AirSTAR [2, 8, 9]

| | **GTM** | **AirSTAR** |
|---|---|---|
| *Property* | *Value* | |
| Span $[m]$ | 37.80 | 2.08 |
| Length $[m]$ | 44.5 | 2.44 |
| Mass $[kg]$ | 90718 | 22.50 |
| Roll Inertia $[kgm^2]$ | $3.6 \cdot 10^6$ | 1.8 |
| Airspeed $[m/s]$ | 143.1 | 33.53 |
| Altitude $[m]$ | 3962 | 304.8 |

Figure 1.3: The AirSTAR model aircraft [2]

### 1.3.3. AREA-I PTERA

In cooperation with NASA the American company Area-I, Inc. designed and built the Prototype-Technology-Evaluation and Research Aircraft (PTERA). The PTERA is a 11% scaled model of a Boeing 737, designed to test advanced aerodynamic treatments and to validate aero-efficiency, aeroelasticity, control and dynamics, structures and acoustics [10]. The PTERA was designed to be modular and is designed to accommodate various different configurations. The PTERA has different dimensions and masses for different configurations, as can be seen in Table 1.2. Currently the PTERA aircraft is in use by NASA's Armstrong Flight Test Center, where it is being flown to collect flight data, which can then be made open to the public. Figure 1.4 shows a picture of the PTERA in flight.

The PTERA is also be used as a basis for a technology demonstrator for high-lift concepts, the Cruise-Efficient Extreme-STOL-Capable Demonstrator UAV (CEETA) [11]. STOL stands for Short Take-off and Landing. This aircraft aims to use over-the-wing powered lift in combination with circulation control, in the form of leading-edge and trailing edge blowing, to achieve STOL capabilities, without impacting the cruise capabilities too much. Over-the-wing powered lift will be achieved by using an exhaust hood to redirect the flow from the over-wing mounted turbojet engine and the blowing on the wing is done using an axillary power unit (APU), which will be mounted in the fuselage.

Figure 1.4: The PTERA during test flight [10]

Table 1.2: Characteristics for the PTERA BL and GMATT [10]

| | **BL** | **GMATT** |
|---|---|---|
| *Property* | *Value* | |
| Scale Factor | 0.11 | 0.16 |
| Span $[m]$ | 3.44 | 3.75 |
| Length $[m]$ | 3.66 | 5.18 |
| Maximum Take-off Weight $[kg]$ | 90.71 | 130.2 |
| Payload $[kg]$ | 18.14 | 68 *(including fuel)* |

### 1.3.4. IEP

The IEP (or Innovative Evaluation Platform) is part of the NACRE (New Aircraft Concept REsearch) European program. It has been designed as a sub-scale test platform, with three main focus points: the identification of stability and control parameters, the noise assessment, the analysis of different recovery procedures in the case of hazardous flight conditions [12]. The model is designed to be modulair, such that different configurations can be tested without too much rebuilding. The model was sized based on Froude scaling of a full scale aircraft, the availability of commercial off-the-shelf (COTS) jet engines and practical operation aspects. These practical operation aspects include the visibility of the ground pilot, since it must be visible at all times and during the first flights no further than 1000m away from the observer. [12]

The IEP has a length and wingspan of $4.5m$, a reference surface area of $1.8m^2$ and a take-off gross weight of $145kg$. The IEP is based on the Pro-Green Aircraft(PGA), as defined in the NARCRE program. The PGA is a 200 passenger tube-and-wing reference aircraft, with different possible engine configurations. [12]

In 2010 the IEP was gearing up for flight testing, unfortunately however, after a mishap during the first taxi tests the model was damaged and it was no longer possible to complete flight tests during the NACRE program. [13]

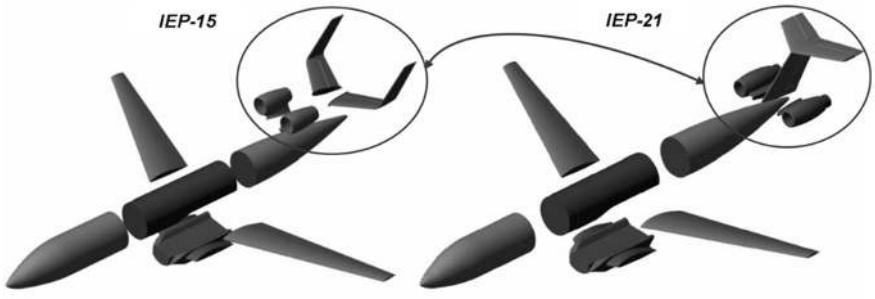


Figure 1.5: A 3D drawing of two different IEP configurations [13]

### 1.3.5. SCALED JOINED WING CONCEPT

The Boeing Joined Wing SensorCraft (JWSC) is a high altitutde, long endurance (HALE) conceptual UAV. It is designed to be an intelligence, surveillance and reconnaissance platform, with an innovative joined wing concept. A $1/9^{th}$ scale model is constructed to explore the aeroelastic response of the joined wing design [14]. Since aeroelasticity is the focal point of this research, aeroelastic similarity must exist between the model and the full scale aircraft. Two methods are proposed for the scaling, namely with respect to span, air density and velocity or with respect to span, air density and maximum take-off weight (MTOW). After a trade-off it is found using the method for scaling with respect to the MTOW opposed to the velocity, that the speed and mass will turn out to be too high, around $149m/s$ and $260kg$, versus $29m/s$ and $93kg$. Thus it is determined that the model will be scaled with respect to the span, air density and velocity [14].

Since aeroelasticity is the focus of this project, it is interesting to note the different methods used in obtaining aeroelastic similarity. If the material properties are scaled, along with the structure, the dynamic response of the structure will be similar [15], this does mean using a different material which may not always be available. Because it is not possible to reproduce the exact same internal structure in this study, due to fact that it is classified and manufacturing difficulties, a different method must be used. It is proposed to achieve aeroelastic similarity by first matching (static) linear elastic response and then the (dynamic) modal response [14], by the distribution of discrete masses along the wings. First flight tests were done on a geometrically scaled model, to do a test of concept [16]. Finally the aircraft was flown, where further measurements were done. Here it was found that it was possible to get agreement of the aeroelastic frequency, however for the aeroelastic damping it proved not possible [17].

Figure 1.6: The Joined Wing Sensor Craft concept [14]

### 1.3.6. X-48B

The X-48B scaled blended wing body is a cooperation between NASA, Boeing and the US Air Force Research Laboratories. The X-48B is a 8.5% scaled aircraft designed to test the stability and control characteristics of the blended wing body. The blended wing body is a radical new design over the conventional tube-and-wing, which is commonly used. The X-48B is shown in Figure 1.7, as can be seen the distinction between the fuselage and the wings is more difficult to make. A blended wing body promises some advantages: high internal volume, aerodynamic and structural efficiency and lower noise. [18]

The X-48B is built from composites and is flown from a ground operating system, with the pilot controlling the aircraft with the use of an on-board camera, the aircraft was commonly accompanied by a chase plane. Data on the X-48B can be found in Table 1.3. During several (39 total) test flights the X-48B's flight envelope and novel control laws were tested [18].

### 1.3.7. CONCLUSION

In the past chapter several different small (scale) flying test beds have been discussed. In Table 1.4 an overview of the dimensions and goals of different testing programs can be found. Out of these programs of most interest are the IEP and PTERA, since they both have similar research goals and configuration as the scaled flight test model, to be designed. While the PTERA will have a version which is focussed on aerodynamic testing,

Table 1.3: Data for the Boeing/NASA X-48B [18]

| *Property* | Value |
|---|---|
| Scale Factor | 0.085 |
| Span $[m]$ | 6.22 |
| Thrust $[kN]$ | 0.69 |
| Maximum Take-off Weight $[kg]$ | 227 |
| Maximum Velocity $[m/s]$ | 60.83 |

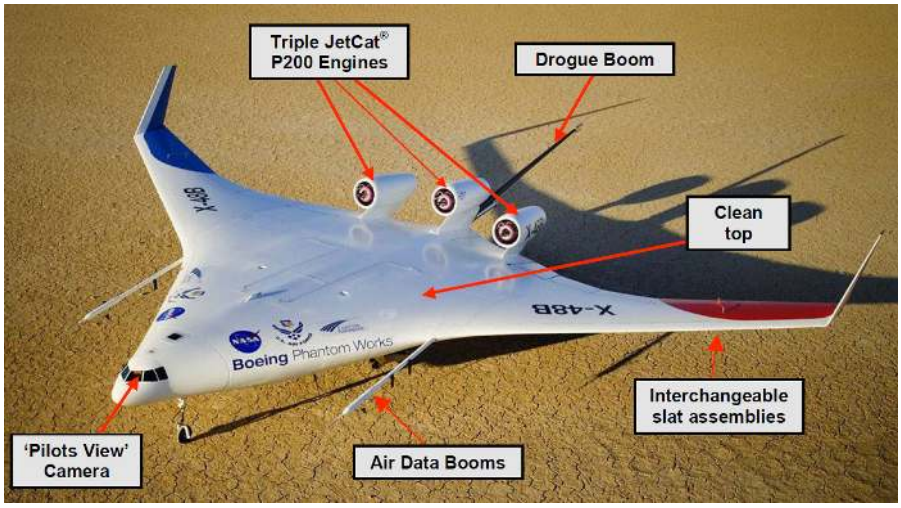


Figure 1.7: The X48B [18]

no data is known about how they are to work with the change in flow conditions and the influence on the results.

None of the mentioned programs include, in their studies, the effect of the change in flight conditions on their test results. Thus while these programs serve as a good reference, their results must be analysed with this fact in mind.

Table 1.4: Overview of the different small scale flying testbeds

| **Program** | *AirSTAR* | *AREA-I PTERA* | *IEP* | *Scaled Joined Wing Concept* | *X-48B* |
|---|---|---|---|---|---|
| **Timeframe** | 2005-now | 2013-now | 2005-2010 | 2007-now | 2007-2013 |
| **Scale** [-] | 0.055 | 0.11-0.16 | n/a | 0.111 | 0.085 |
| **Span** $[m]$ | 2.08 | 3.44-3.75 | 4.5 | | 6.22 |
| **MTOW** $[kg]$ | 22.5 | 90.71-130.2 | 145 | 93 | 227 |
| **Goals** | | | | | |
| **Dynamic Scaled** | ✓ | ✓ | ✓ | ✓ | ✓ |
| **Modular Configuration** | | ✓ | ✓ | | |
| **Novel Concepts** | | Possible | ✓ | ✓ | ✓ |
| **Upset Recovery** | ✓ | ✓ | Possible | Possible | ✓ |
| **Aeroelasticity** | | Possible | | ✓ | |
| **Noise** | | Possible | ✓ | | Possible |

## 1.4. RESEARCH QUESTIONS AND OBJECTIVES

The possible advantages for scaled flight testing are apparent, especially for flight dynamics and upset recovery testing. Differences between a scaled and full scale model will be present, as has been explored before.

There is, however, an uncertainty in just how significant these differences are. Of interest in this study is looking at flight dynamics testing and the influence of the aerodynamic properties on that. One of the consequences of this is that it is desirable to have similar lift and moment coefficients at the same angle of attack. The dynamic response of the aircraft is also important, thus the masses and inertia must also be properly scaled. When looking at flight outside of the normal flight envelope, such as upset recovery, it is also important to have similar maximum lift coefficients.

Another topic of interest, which is closely linked to this, is the influence scaling has on the flow properties at the tail, since the tail has an important influence on the stability and control. This also means and unconventional propulsion incorporation such as tail-mounted ducted fans could be of interest. The region of the flight envelope in which this investigation is done will be the critical flight condition of take-off.

Since the work performed during the master thesis is limited, only the first step towards the design of a scaled flight testing model is made. This means that only investigation is done into the phenomena at play and no design is yet made. The following research objective has been formulated for this master's thesis:

*Investigation the effect of scaling on the aerodynamic properties and of the flow field at the tail location, with the focus on take-off conditions.*

To fulfil this objective a research question has been set, along with several sub-questions. The main research question is:

*How is the design of a scaled atmospheric flight testing model, with the focus on dynamic flight tests, of a regional type of aircraft influenced by scaling effects on the wing and the wake at the tail?*

The following sub questions are posed:

1. What are the relevant scaling laws and how can they be implemented?
2. What are the methods that can be used to investigate the aerodynamic properties?
3. What is the influence of scaling on a wing with high-lift devices?
4. What does the flow field at the tail typically look like?
5. To what extent can the scaled wing be modified in order to better represent the full scale wing?

## 1.5. SCOPE OF CURRENT STUDY

This study will thus investigate the effects of scaling on aerodynamic properties and the flow field at the tail region. As noted before, the interaction between scaling and those properties are very dependent on the configuration chosen. This is why it is important to set a scope to which this study will be limited. These limitations were set to keep the workload manageable and in correspondence with the research direction of the department of Flight Performance and Propulsion.

The focus will be on a small regional type aircraft, which operates at low subsonic Mach numbers. The initial focus will be on the take-off conditions. Section 2.6 has a more complete description of the used flight conditions and geometry. A brief investigation will also be done on how the design will perform in the cruise conditions. This type of aircraft and these flight conditions will minimize the effect of the differences in Mach number, as the Mach number of the full scale case is already relatively low.

Furthermore, the research conducted in this study will focus mainly on the analysis of the wing and, for the most part, exclude the effects of the body. This is done in order to simplify the initial research into the effects of scaling.

### 1.5.1. WAKE SURVEY PLANE

In order to assess the influence of scaling on the wake a 'wake survey plane' has been defined. This wake survey plane is an imaginary surface in the y-z plane, placed at the x-location of the horizontal tail. This allows for an analysis of how scaling influences the flow here, without having to know what kind of tail configuration is used. For example, instead of a conventional horizontal and vertical tail, propulsion with integrated control surfaces could be placed here. Figure 1.9 has a rending of what such an unconventional propulsion integration could look like. An illustration of the wake survey plane is given in Figure 1.8. In Figure 1.8a it can

be seen that it spans the width of the horizontal tail and has half the same dimension in z (vertical) direction. Figure 1.8b shows the longitudinal location of the wake-survey plane.

Figure 1.8 also has the coordinate system as used here. It is a right hand system, with the origin at the quarter chord point. Figure 1.8b shows the origin of the coordinate system above the aircraft, whereas the origin is on the wing, this is done for clarity.

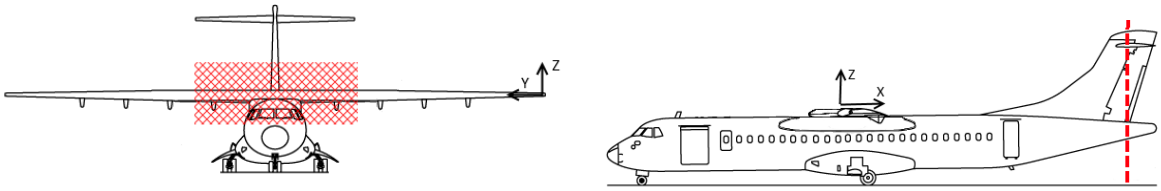


(a) Front view of the wake survey plane

(b) Side view of the wake survey plane

Figure 1.8: The wake survey plane

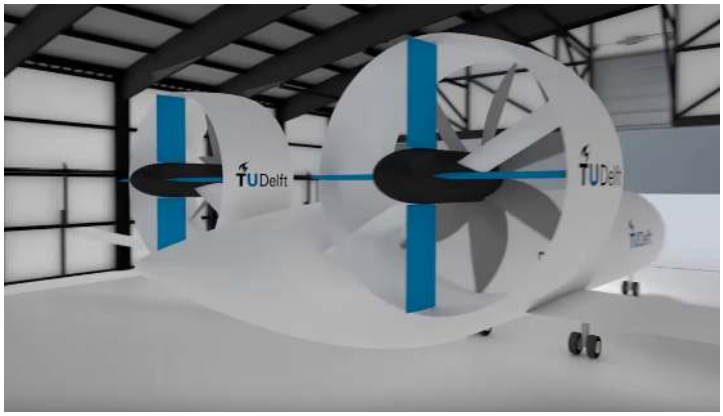


Figure 1.9: Example of unconventional tail configuration, the DUUC [19]

## 1.6. OUTLINE OF THESIS

This thesis can be split into four main parts, first there is an introduction into scaled flight testing and a theoretical background in Chapter 2. After that, the methods which are used for the analysis (Chapter 3), wake (Chapter 4) and optimization (Chapter 5) are given. In the next part the results are given. First the results of the analysis in Chapter 6, next the results of the wake in Chapter 7 and finally, the results of the optimization are given in Chapter 8. This thesis is concluded with a conclusion and recommendations in Chapter 9.

# 2

# ASPECTS OF SCALED FLIGHT TESTING

This chapter will give a background on the phenomena occurring when scaling is performed and gives background about the analysis methods used. First the different methods of scaling are discussed. Next, in Section 2.2, the influence of scaling on the aerodynamic properties is further explored and a basis for this is investigated in the boundary layer, in Section 2.3. Section 2.4 has the requirements for similitude on which the scaled wing will be analysed. Section 2.5 has a brief introduction on longitudinal static stability, in order to do a first assessment of scaling on the dynamics of an aircraft. Section 2.6 introduces the use case used in this thesis and how the scaling is applied here. The conclusion of this chapter can be found in Section 2.7.

## 2.1. DIFFERENT SCALING PHILOSOPHIES

In order to be able to produce correct results with a scaled flight test model, the scaling most be done such that certain properties are similar. Which properties must be similar, depend on the goal of the testing program; testing for flight dynamics impose different requirements than testing for aeroelasticity only. The following chapter will highlight relevant dimensionless quantities which are used in scaling to ensure similarity. Depending on the situation and the topic which is to be researched, different dimensionless quantities must match.

### 2.1.1. GEOMETRIC SCALING

The first and most important similarity is that of geometric similarity. This states that the outer dimensions, thus aerodynamic shape, must match. The formal definition is given in Equation (2.1), $n$ is the scaling factor, $L$ is an arbitrary length and $_M$ and $_F$ denote the model and full scale respectively. This geometric scaling factor usually forms the basis of the further scaling effort.

$$n_L = \frac{l_M}{l_F} \tag{2.1}$$

### 2.1.2. FROUDE SCALING

The Froude number is a dimensionless number which relates inertial and gravitational effects. The Froude number is especially relevant for banking flight, where a similar Froude number ensures an equal bank angle and load factor [20]. Froude scaling refers to scaling the model to keep the Froude number equal for the full-scale and the model. The Froude number is given in Equation (2.2), where $V$ is the flow velocity, $l$ is characteristic length.

$$FR = \frac{V^2}{lg} \tag{2.2}$$

For Froude scaling the ratio between the Froude number of the full scale and the sub scale must be unity. As can be seen, the Reynolds number and the Froude number both share the terms for the velocity and the length, but they scale differently. Thus for an atmospheric free flight model it is almost impossible to have similar Reynolds and Froude number, compared to the full scale aircraft.

When doing tests on the flight dynamic behaviour of a scaled aircraft, Froude similarity is important. Figure 2.1 shows the importance of keeping the Froude number the same, when looking at dynamic response, shown are the response of the full scale case, Froude scaled and non-Froude scaled case.

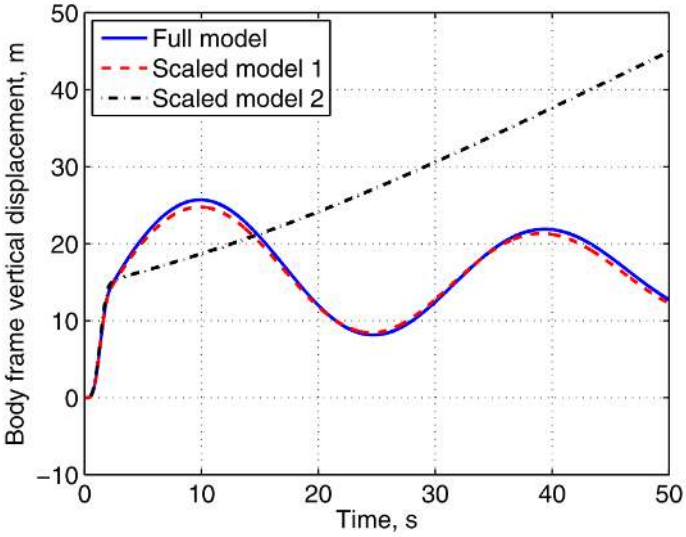


Figure 2.1: The effect of Froude scaling on dynamic behaviour [21]

### 2.1.3. DYNAMIC SCALING

Dynamic scaling is done with the aim to scale the dynamic properties of the model. This means that the weight, inertia and control system responses must be scaled that the dynamic response of the model corresponds to the full scale aircraft. This is of interest when tests are being done on, for example, flight mechanics, control allocation and upset recovery. [8, 22]

The similitude requirement for level flight require that the lift coefficients of both aircraft are equal. Equation (2.3) shows that the lift coefficient can be rewritten to be dependent on the Froude number and a factor of mass, density and length. If the Froude number is matched and lift similarity is desired, then the mass scales with a factor $l^3$ [20].

$$C_L = W/0.5\rho V^2 S = 2\left(\frac{m}{\rho S\bar{c}}\right)\left(\frac{g\bar{c}}{V^2}\right) = f\left(\frac{m}{\rho l^3}, \frac{gl}{V^2}\right) \tag{2.3}$$

For dynamic response the inertia of an object is also important. To get a relation for this the expression relating the moment coefficient to the mass moment of inertia is given in Equation (2.4), here $\dot{q}$ is the dimensionless dynamic pressure. Where $C_M$ can be rewritten as in Equation (2.5). Thus if the similarity of the moment is required, the inertia scales with a factor $l^5$ [20].

$$I\dot{q} = C_M 0.5\rho V^2 S\bar{c} \tag{2.4}$$

$$C_M = 2\left(\frac{I}{\rho S\bar{c}^3}\right)\left(\frac{\dot{q}\bar{c}^2}{V^2}\right) = f\left(\frac{I}{\rho l^5}\right)\left(\frac{\dot{q}l^2}{V^2}\right) \tag{2.5}$$

### 2.1.4. REYNOLD SCALING

Reynolds number is a well known parameter in aerodynamics and aerospace engineering. In order to preserve dynamic similarity in the flow itself, amongst others, the ratio of inertia to viscous forces (i.e the Reynolds number) must be in proportion. In practice this means keeping the Reynolds number the same. The transition of flow, the boundary layer conditions and separation of the airflow are functions of Reynolds number.

The Reynolds number has an important influence on configurations where separation or transitions determine the aerodynamic characteristics. Configurations where flow separation or transitions is fixed, such as sharp edges or vortex generators, are influenced less by the change in flow properties and thus Reynolds

number. However for configurations where the transition and separation points are important, for example with natural laminar flow wings, the Reynolds number becomes very relevant.

The definition of the Reynolds number is given in Equation (2.6), here $V$ is the velocity of the object with respect to the flow, $l$ is the characteristic length of the object in the flow, i.e. the travelled length in the fluid.

$$Re = \frac{Vl}{\nu} \tag{2.6}$$

In order to ensure excellent aerodynamic similarity the Reynolds number must be the same. If it assumed that the length is no longer the same, that means either the velocity or the viscosity of the flow must change. With windtunnels this is normally achieved cryogenic windtunnels, however for free flight this poses a challenge and can be said to be the import important technical issue in free-flight testing [1].

### 2.1.5. MACH SCALING

Mach number is the ratio between the velocity of the object and the velocity of sound in the (compressible) fluid medium, through which the object is moving. It is a property of a compressible fluid that a change in absolute pressure causes a change in density. Thus when an object is moving faster through the flow the density increases. The definition of the Mach number is given in Equation (2.7).

The only way to effectively simulate the effect of the Mach number is to subject the scaled model to the desired Mach number. For atmospheric flight testing this will lead to several problems, since the airspeed of model will need to be very high, in the order of $3 \cdot 10^2$ $m/s$.

$$M = \frac{V}{a} \tag{2.7}$$

## 2.2. INFLUENCE OF SCALING ON THE AERODYNAMIC PROPERTIES

Figure 1.2 already showed the effect of the flow at different Reynolds number with respect to lift and drag of a wing. The lift curve slope and maximum lift tends to decrease with decreasing Reynolds number, whereas the drag increases with decreasing Reynolds number. The effect of scaling on the moment is investigated in Figure 2.2a. Here an increase of $C_M$ with an increase of Reynolds number is observed. The effect of Mach number on the maximum lift can be seen in Figure 2.2b, it shows an increase of maximum lift coefficient with a decrease of Mach number.

The Mach effect has an opposing effect as the Reynolds number on the moment and lift coefficient, namely the lift and moment coefficients increase with increasing Mach number. This is indicated by the *Prandtl-Glauert rule* [23] in Equation (2.8), it is a compressibility correction and states that the pressure coefficient coefficient will increase with increasing Mach number. Since the lift and moment coefficients are integrals of the pressure coefficient over a body, this rule is also valid for the lift and moment coefficient. The rule has a reasonable accuracy and can be used up to a Mach number of 0.7.

$$C_p = \frac{C_{p,0}}{\sqrt{1 - M_\infty^2}} \tag{2.8}$$

It can be concluded that when going from full scale to a small scale testing model that the aerodynamic properties will change. Lift and maximum lift will decrease, due to the Reynolds effect. On the other hand, the decrease in Mach number will cause an increase of lift and maximum lift. However, it is expected that the effect of the different Reynolds number will be more pronounced. The moment coefficient will decrease when going to small scale and the drag coefficient will increase. To investigate where these differences may come from, the next section will look into the changes of the boundary layer with scaling.

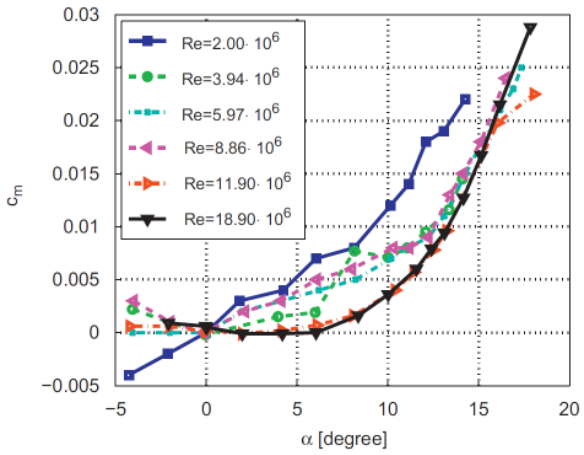


(a) Effect of Reynolds number on moment coefficient [5, 24]

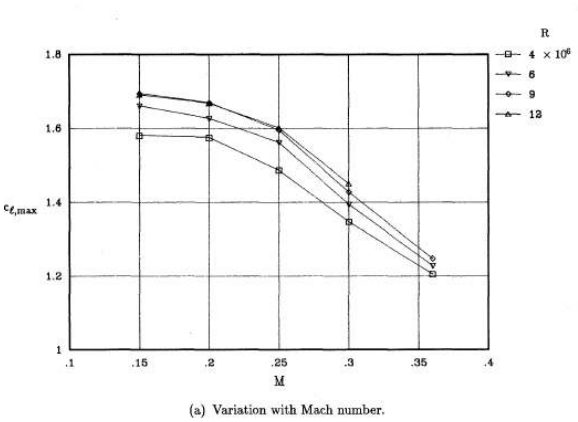


(a) Variation with Mach number.

(b) Effect of Mach number on maximum lift coefficient [24]

Figure 2.2: Effect of Reynolds and Mach number on moment and maximum lift coefficient on a NACA0012 airfoil

## 2.3. INFLUENCE OF SCALING ON THE BOUNDARY LAYER

The following section will have a brief look at how scaling influences the boundary layer. The boundary layer is the concept of the region of the fluid around an object, in which the viscous effects are important. The size and state of the boundary layer have an important influence on the aerodynamic properties of an object. As noted before in Section 1.5 the focus is on low subsonic Mach numbers, so shock wave interactions, where the boundary layer thickness and state play an important role, are not investigated here.

#### BOUNDARY LAYER THICKNESS

Since the boundary layer is not a clear layer, but rather a concept which denotes the region of flow close to the object, several different definitions of the thickness are in use. The most common are the velocity boundary layer thickness ($\delta$), displacement thickness ($\delta^*$) and momentum thickness ($\theta$):

- $\delta$ - The velocity boundary layer thickness is defined as the point above the surface at which the velocity is equal to 99% of the freestream
- $\delta^*$ - The displacement thickness is distance which the external flow is displaced by the presence of the boundary layer
- $\theta$ - The momentum thickness is distance which the surface has to moved parallel to itself, to give the same momentum as for an inviscid flow

The thickness of a boundary layer over a flat plat may be approximated by Equation (2.9) and Equation (2.10) [25]. The first equation is the Blasius solution and is valid for laminar boundary layers, the second is for turbulent boundary layers, for both equations $x$ is the downstream distance from te leading edge point and $Re$ is the Reynolds number, see Equation (2.6). This approximation allows us to look at what factors influence the boundary layer over an airfoil. It is clear that the boundary layer grows when moving further downstream. Also visible here is that the boundary layer will be thicker for an airfoil at low Reynolds number. When the aircraft is not Reynolds scaled the boundary layer will thus be relatively thicker.

$$\delta = 5x/\sqrt{Re} \tag{2.9}$$

$$\delta = 0.37x/Re^{1/5} \tag{2.10}$$

The boundary layer thickness ($\delta^*$) changes the aerodynamic properties of the airfoil, the flow sees a combination of the airfoil and the boundary layer as the effective airfoil, this is a decambering effect of the airfoil. Thus with a relatively thicker boundary layer the change to the effective airfoil shape is greater.

It is also clear from Equation (2.9) and Equation (2.10) that a turbulent boundary layer is much thicker than a laminar boundary layer. Thus it is also worthwhile to look at when the boundary layer changes from laminar to turbulent.

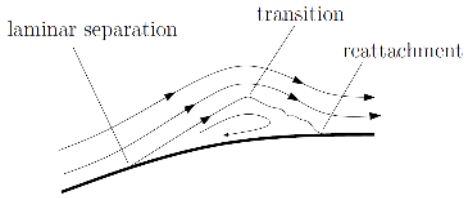


Figure 2.3: An illustration of a laminar separation bubble [27]

**TRANSITION**
Lower values of Reynolds number lead to a rearward movement of the transition point, thus an airfoil at lower Reynolds number has more laminar flow [26]. This is a important difference, since a turbulent boundary layer has different properties than a laminar boundary layer, as noted before.

**SEPARATION**
A laminar boundary layer is also more prone to separation, by an adverse pressure gradient. When the flow separates towards the rear of the airfoil, it can be assumed that stall occurs, since the separation is combined with a large loss in lift. For high Reynolds number flows, this is commonly in the turbulent part of the boundary layer. However, at low Reynolds number, laminar separation bubbles can form. These bubbles are (small) regions of separated flow, after which the flow reattaches itself to the airfoil. In these bubbles the flow is fully turbulent and backflow, i.e. flow in the other direction than the freestream flow direction, can exist. An illustration of such a laminar separation bubble is given in Figure 2.3. This laminar separation has a big influence on the drag, but also on the lift and moment of an airfoil.

## 2.4. REQUIREMENTS FOR SIMILITUDE

In order to have similar aerodynamic behaviour at different Reynolds number, the following properties are important for dynamic flight test [28]:

- Maximum lift coefficient - $C_{L,max}$
- Lift curve slope - $\frac{dC_L}{d\alpha}$
- Moment - $C_M$
- Stall behaviour

### 2.4.1. MAXIMUM LIFT

The maximum lift coefficient, $C_{L,max}$, is an important parameter to match when looking at flight tests including (level) stall, spin and upset recovery, since these phenomena occur at regions near maximum lift coefficient. Figure 1.2a shows the influence of changing Reynolds number on maximum lift coefficient, while Figure 2.2b shows the effect of Mach number. The decrease of $C_{l,max}$ can be explained by less energetic, laminar, boundary layer, which is more prone to separation [5].

### 2.4.2. LIFT CURVE SLOPE

The (linear) lift curve slope is also important when doing flight testing, since this guarantees similar reaction to a change in angle of attack. A difference in zero-lift angle of attack could be negated by having an incidence angle of the wing, however this could alter the geometric angle of attack at which the aircraft reaches its maximum lift. The lift curve slope is changed by scaling due to the (relative) thickening of the boundary layer, with reducing Reynolds number, as this leads to a decambering effect, see Section 2.3. Due to the compressibility effects, a decreasing Mach number leads to a lower lift and lift curve, although the effects are still minimal when looking at Reynolds number below approximately 0.3 [6].

### 2.4.3. MOMENT

A change in moment (coefficient) about the wing leads to a change in stability for the entire aircraft, this is why it is important to match the moment coefficient as best as possible. The moment is the result of how the lift is distributed chordwise and in case of sweep also spanwise. The distribution of forces of course has a direct influence on the static and thus dynamic stability of a wing and aircraft.

### 2.4.4. STALL BEHAVIOUR

As discussed before the change in flow conditions has a direct influence on the transition and separation of the flow on the wing. Thus the change in Reynolds number leads to a change in stall behaviour. Different kinds of stall mechanisms lead to different behaviour during the stall and thus also to different procedures for upset recovery. Generally speaking three different kinds of stall mechanisms can be identified: trailing-edge, leading-edge and thin-airfoil stall. It is assumed that a clean airfoil, in a low turbulence flow, stalls by either one or a combination of two of these mechanisms. A correlation has been found between the type of stall, the flows Reynolds number and the upper surface coordinate of the airfoil at 1.25% chord. The correlation between the type of stall and the Reynolds number seems intuitive, as the type of stall is highly dependent on the state of the boundary layer and changes Reynolds number affect the boundary layer [29]. However, there is no clear physical basis for the correlation between the upper surface coordinate and the type of stall and, thus, this is more of an empirical rule. Figure 2.4 shows the types of stall for different thickness and Reynolds number. Below are further descriptions of how these mechanisms work [29].

#### TRAILING-EDGE STALL

This type of stall is marked by forward movement of the point of boundary layer separation, with increasing angle of attack, starting at the trailing edge. On lift and moment curves this can be seen as gradual variations, with a well-rounded lift curve peak.

#### LEADING-EDGE STALL

An abrupt flow separation of the laminar boundary layer, at the leading edge, is called leading-edge stall. In lift curves leading-edge stall can be seen as an abrupt drop in lift, after the maximum lift is reached.

#### THIN-AIRFOIL STALL

Thin-airfoil stall is when a laminar separation bubble, starting at the leading edge, grows in chordwise length, with increasing angle of attack and finally leads to leading edge separation. The laminar separation bubbles are visible on the lift curve as a discontinuous change in lift curve slope, it is further characterized by a well-rounded maximum lift curve.

#### COMBINED STALL

According to Vos and Farokhi [6] often a combination of leading- and trailing-edge stall occurs; a short laminar separation bubble occurs at the leading-edge, after which the flow reattaches and the turbulent boundary layer separates near the trailing edge. The presence of the laminar separation bubble causes a thicker boundary layer, which is more likely to separate.

### 2.4.5. DRAG

The drag, or drag coefficient, is not taken into account in the list mentioned at the start of this section. This is because, just like the previous aerodynamic properties, the drag is bound to increase with decreasing Reynolds number. The drag is increased via several mechanisms. An obvious one is the increase of viscous drag, with a decrease of Reynolds number, the viscous forces become more important and thus the skin-friction drag will increase. As noted before, at low Reynolds number laminar separation regions can exist, these regions give rise to a large increase in pressure drag.

A way to overcome the consequence of the increase in drag is by simply increasing the thrust, to still be able to fly the flight envelope. This is, of course, not a solution to the problem, but rather a solution to the symptom.

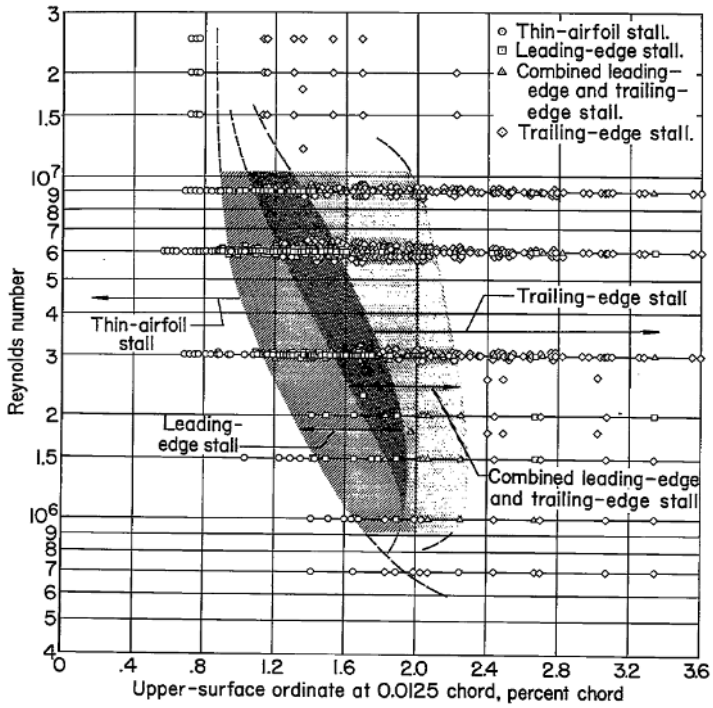


Figure 2.4: Different stall characteristics as function of Reynolds number and leading-edge thickness [29]

## 2.5. LONGITUDINAL STATIC STABILITY

When looking at flight dynamics an important parameter is the longitudinal static stability. It is relevant to look at this since this to a great deal affected by the horizontal tail. Scaling has influence on the horizontal tail in two ways, the aerodynamic properties of the horizontal tail itself change. Besides it is also affected by the flowfield, due to the wake of the main wing. The equation for the location of the neutral point is given by Equation (2.11), when the equation is true the aircraft is statically stable. $x_{ac}$ is the location of the aerodynamic center of the wing and $\frac{V_h}{V}$ is the ratio between the velocity at the tail and the wing.

It is now interesting to look at which of these parameters will change due to scaling. Immediately the importance of geometric scaling is visible, if all the lengths and areas are not scaled equally, the neutral point will be at a different location.

The term $\frac{C_{L\alpha_h}}{C_{L\alpha}}$ will likely change, however, since the Reynolds number scaling effects for the main wing and horizontal tail are not the same. The horizontal tail operates at a lower Reynolds number than the main wing. Another term which will likely differ is $\frac{d\varepsilon}{d\alpha}$, since the downwash is dependent on the lift generated, the downwash gradient is thus similar to the lift curve slope. Also the velocity ratio might differ, depending on the location of the tail. If the tail is a high mounted T-tail, then it will be free of the interfering effects of the wing and the body. However, with low tails effects from the main wing and/or body will be present.

$$\overline{x}_{np} = \overline{x}_{ac} + \frac{C_{L\alpha_h}}{C_{L\alpha}}\left(1 - \frac{d\varepsilon}{d\alpha}\right)\frac{S_h l_h}{S\overline{c}}\left(\frac{V_h}{V}\right)^2 \tag{2.11}$$

## 2.6. USE CASE

In this section the use case is investigated, with all the geometries and flight conditions. Besides this, it is possible to look at some scaled cases and determine a default case, which can be used for further analysis.

### 2.6.1. FULL SCALE CASE

As stated before in Section 1.5, the study focusses on a regional aircraft, in this case the ATR72, see Section 2.6.1. The ATR 72 is a twin-engine turboprop regional aircraft, produced by the European ATR manufacturer. The ATR 72 is developed as a stretched version of the ATR42 and has been in service since 1989. It is difficult to obtain a complete dataset about this aircraft, however, using various sources and estimates, the

data set as given in Table 2.1 is used. It has a very slender wing, with barely any sweep. Also, since no clear data was found on the twist angle, it is set to zero.

Another point of interest is the airfoil. Various unconfirmed sources state that a modified NACA43018 airfoil is used, but what these modifications entail is not clear. Due to unavailability of further data about this airfoil, a choice has to be made for a different airfoil. The NLR7301 airfoil has been chosen, as can be seen in Figure 2.6a, there are quite some differences between these. The NLR7301 is a transonic airfoil, thus one not suited for a low subsonic aircraft, like the ATR72. NLR7301 was chosen as airfoil because of the good availability of data, with and without a slotted flap. The flap is a 32% chord flap, deployable at different angles, shown in Figure 2.6b. Using the NLR7301 airfoil makes sure that the method can be validated and that the clean and flapped case are a fair comparison. Since the focus is on the take-off conditions in this research, it is necessary to look at the wing in take-off conditions. During take-off conditions the 'Flight Crew Operating Manual' [30] prescribes, under standard conditions, the flaps at an angle of 15 degrees.

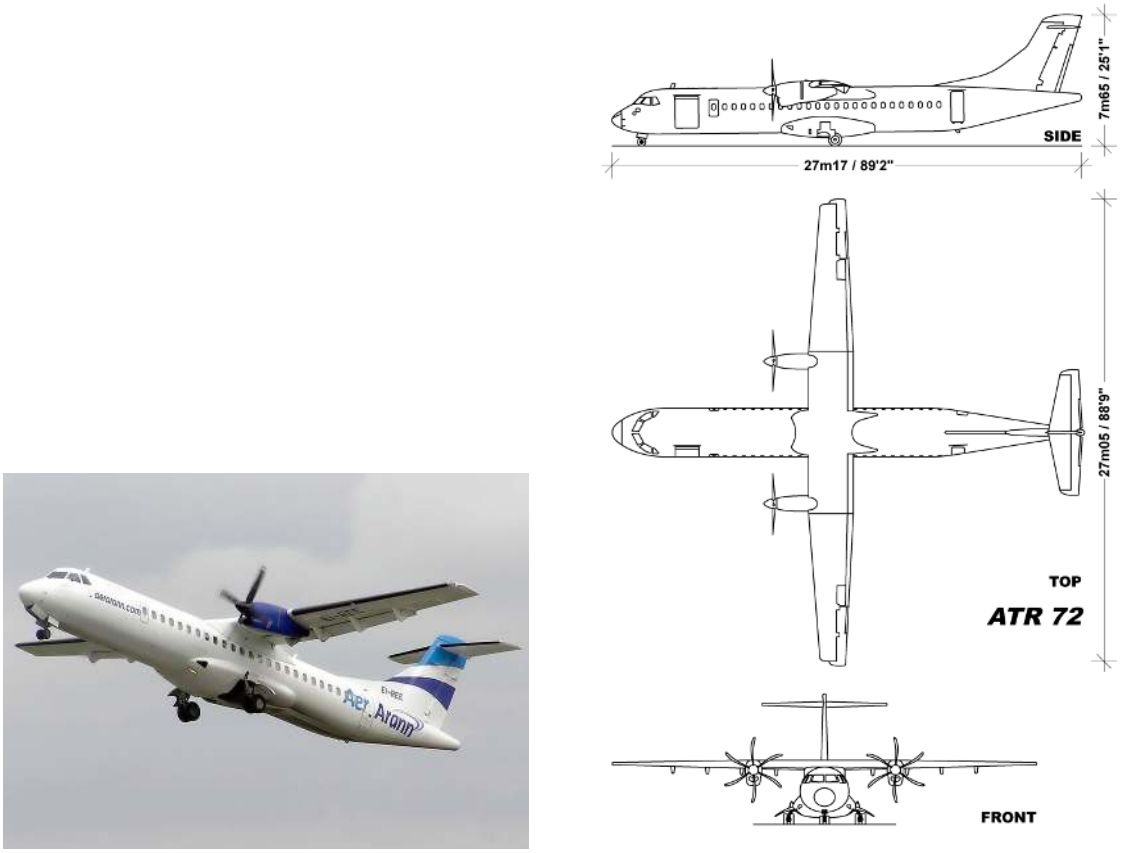


(a) ATR-72 in flight [31]

(b) ATR-72 three-way view [31]

Figure 2.5: The ATR-72

### 2.6.2. SCALING

In Section 2.1 various different scaling methods have been discussed, now it will be discussed how these are used in the current study. This research is concerned with the effects of scaling on the aerodynamic properties, in the context of dynamic flight tests. Since the tests will be performed under take-off conditions, the altitude and thus air density of both the models can be assumed to be the same.

First of all, it is important that geometric similarity is met, since this is the most important similarity, when looking at aerodynamic tests. Geometric scaling thus determines the shape of the aircraft, as it going to be a scaled down version of the use-case, it is going to be scaled with the scale factor $n$. The value of the scale factor must be determined based on maximum dimensions. Next, dynamic scaling is also important as dynamic flight testing is of importance, where the dynamic responses must be similar. This means that the masses and inertias are also known, based on the full scale case. Masses will scale with a factor of $n^3$ and inertias with a factor $n^5$. As was shown in Section 2.1 Froude number matching is also important when

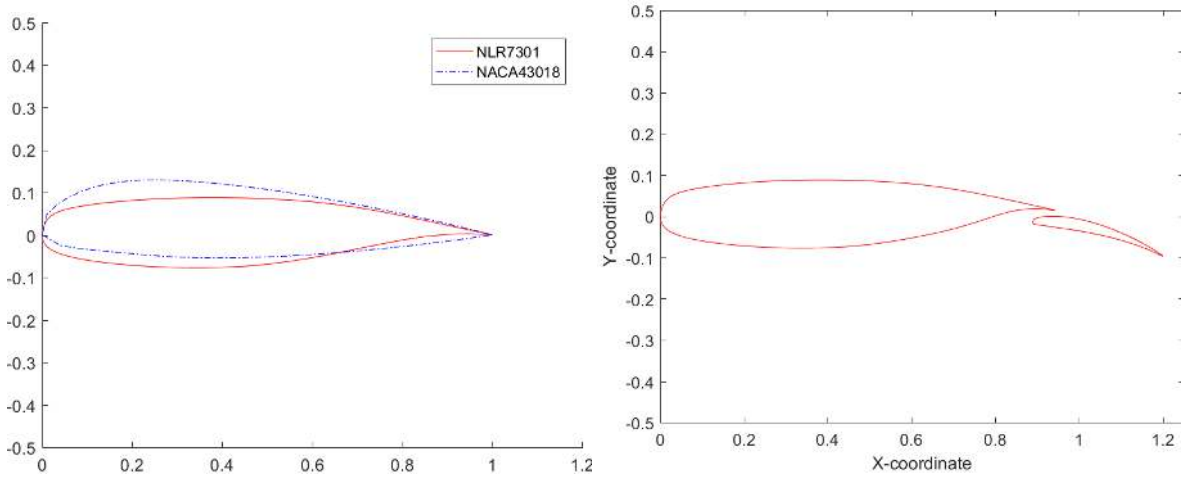


(a) The two different airfoils

(b) NLR7301 airfoil with flap 15 degrees

Figure 2.6: The airfoils used in this study

Table 2.1: ATR72 Data [32]

| *Dimensions* | | *Take-off Conditions* | |
|---|---|---|---|
| Span $[m]$ | 27.05 | MTOW $[kg]$ | 22000 |
| Length $[m]$ | 27.2 | Velocity $[m/s]$ | 59.2 |
| Fuselage width $[m]$ | 2.5 | Mach $[-]$ | 0.17 |
| Wing Area $[m^2]$ | 61 | $C_L$ $[-]$ | 1.65 |
| Root chord $[m]$ | 2.57 | Wing Loading $[N/m]$ | 3538 |
| Tip chord $[m]$ | 1.59 | | |
| Taper ratio $[-]$ | 0.62 | | |
| Kink location $[m]$ | 4.85 | | |
| Aspect Ratio $[-]$ | 12 | | |
| Flap span $[m]$ | 16.2 | | |

looking at dynamic testing. This determines the velocity, it is scaled with a factor $\sqrt{n}$.

When looking at aerodynamic testing, ideally Reynolds and Mach number are also to be matched, as these have a clear influence on the aerodynamic properties. However, under atmospheric flight conditions, Reynolds number matching is not compatible with a scale factor below 1, if Froude, dynamic and geometric scaling is also to be matched. In addition, Mach number matching is not compatible with matching the Froude number and should Mach number matching be chosen, this means excessively high velocity, for aircraft at smaller scales.

### 2.6.3. SCALING RESULTS

The closer the scaling factor is to unity, the better the results are [33]. However, with the increase in size come an increase in cost and problems with operability. If, for example, the scale factor is set at 0.5 the aircraft will have a span of $13.5m$. A balance must be found. An initial limit on the wing design was that the span could not exceed $4m$, in order to still be operable. This is similar to that found for other comparable programs [4, 10, 12]. With a full size span of $27.05m$ this gives a rounded down geometric scaling factor of 14.7%. Combining this geometric scaling factor with dynamic and Froude scaling, gives the data as in Table 2.2. This will be the basis on which the calculations will be done, unless specified otherwise. A representation of the ATR7-72, along with the scaled version is given in Figure 2.7.

It is also interesting to look at how the properties change with scale factor, Figure 2.8 has an overview of how the scale influence some important parameters. Figure 2.8a shows the difference between only dynamic scaling and dynamic and Froude scaling, for the mean aerodynamic chord at take-off velocity. Froude scaling influences the velocity, as can be seen in Figure 2.8b. Figure 2.8c shows the increase of mass with increasing scale factor.

Table 2.2: Full size and scaled data of the ATR-72

| *Dimensions* | Full Size | 14.7 % Scaled |
|---|---|---|
| Span $[m]$ | 27.05 | 3.98 |
| Length $[m]$ | 27.2 | 4.00 |
| Fuselage width $[m]$ | 2.5 | 0.3675 |
| Wing Area $[m^2]$ | 61 | 1.32 |
| Root chord $[m]$ | 2.57 | 0.378 |
| Tip chord $[m]$ | 1.59 | 0.234 |
| MAC $[m]$ | 2.30 | 0.339 |
| Taper ratio $[-]$ | 0.62 | 0.62 |
| Kink location $[m]$ | 4.85 | 0.713 |
| Aspect Ratio $[-]$ | 12 | 12 |
| Flap span $[m]$ | 16.2 | 2.38 |
| *Take-off Conditions* | | |
| MTOW $[kg]$ | 22000 | 69.9 |
| Velocity $[m/s]$ | 59.2 | 22.7 |
| Mach $[-]$ | 0.17 | 0.67 |
| $C_L$ $[-]$ | 1.65 | 1.65 |
| Wing Loading $[N/m]$ | 3538 | 520.1 |
| Reynolds number MAC $[-]$ | $9.3{\cdot}10^6$ | $5.3{\cdot}10^5$ |

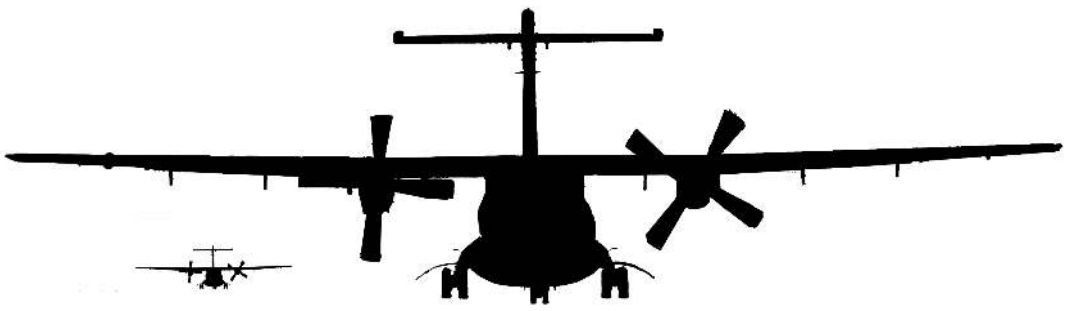

Figure 2.7: Full size and scaled ATR-72

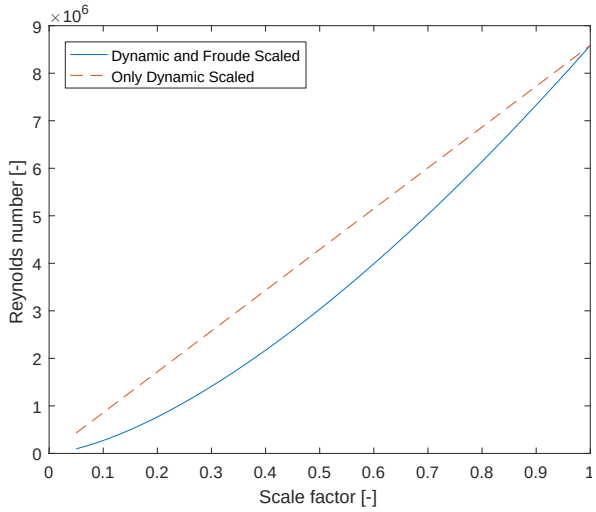


(a) Effect of scale on Reynolds number

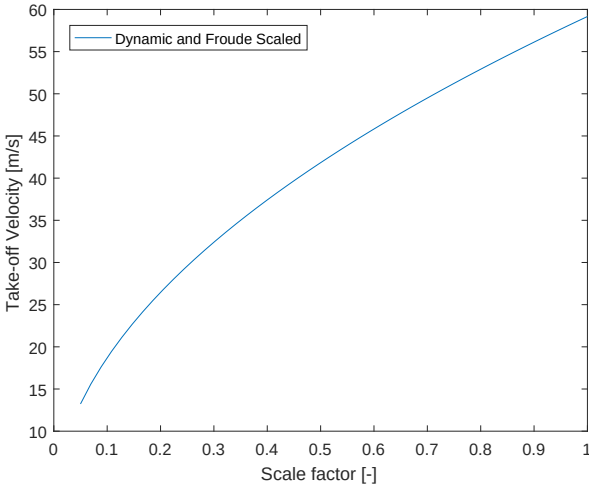


(b) Effect of scale on take-off velocity

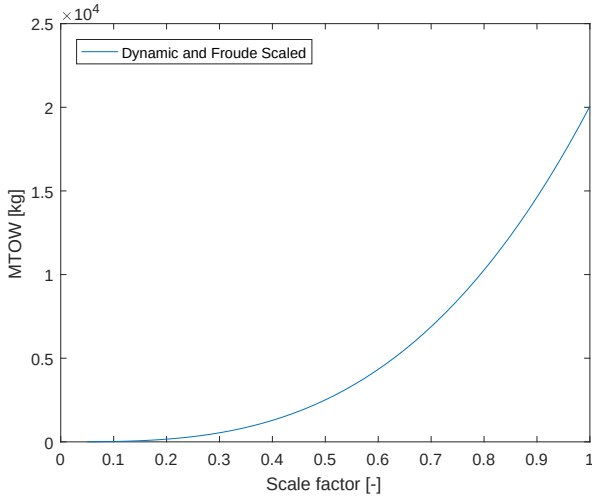


(c) Effect of scale on take-off mass

Figure 2.8: Effect of scale factor

## 2.7. CONCLUSION

The analysis of the aerodynamic properties will be conducted on a 14.7% geometrically scaled version of the regional aircraft ATR72. The mass and flight speed is determined based on dynamic and Froude scaling. When flight testing is done at different flight conditions as the full scale case, the aerodynamic properties will also change. This is due to the greater effect of viscous forces on the boundary layer.

For similarity the (maximum) lift and moment coefficient, along with stall behaviour are deemed as important.

# 3

# METHODOLOGY OF THE WING ANALYSIS

With the background and expected results discussed, it is now time to look at the different method and implementation thereof, which are used to do the analysis of the wing. The following chapter only gives a brief introduction into the various methods, the reader is encouraged to read further in the background in well-known aerodynamics books such as Anderson [23] or Katz and Plotkin [34]. First the background of the used methods are described in Section 3.1 for the clean wing and in Section 3.2 for the flapped case. After that, in Section 3.3 the different tools used in order to do the analysis of the wing are explained. Finally, the chapter is ended with a conclusion.

## 3.1. CLEAN WING AERODYNAMIC ANALYSIS

The analysis of the wing is split up in two parts, namely the clean wing and wing with flap. This is done because both these methods require different methods for analysis, most methods are not able to accurately represent multi surface wings and their mutual interactions. The interest of this study is in the change of the aerodynamic properties, such as $C_L$,$C_D$, and $C_M$, when scaling down the wing. Again, a further distinction can be made: analysis of the wing during the linear regime of the properties, and the maximum lift.

In the coming sections the different methods that enable a quick and flexible analysis of the full and scaled wing will be discussed.

### 3.1.1. VORTEX LATTICE METHOD

The vortex lattice method (VLM) is an expansion of the lifting line theory, which was first developed by Ludwig Prandtl. The starting point of this theory is to replace the wing by a bounded vortex with a strength $\Gamma$. This bounded vortex will give a lift according to the Kutta-Joukowski theorem, in Equation (3.1). Contrary to a free vortex, this bounded vortex is at a fixed location, which means this vortex cannot end at the wing tip, according to the Helmhol'z vortex theorem [23]. This leads to the continuation of the vortex at the wing tips, as a free vortex downstream, to infinity, these two vortices cause an induced downward velocity along the wing. This is represented in Figure 3.1 and it is called a horseshoe vortex, because of the shape. This single horseshoe vortex is not sufficient to represent the realistically represent a full wing, so a collection horseshoe vortices is placed along a line between the wingtips. This is called the lifting line. [23]

$$L = \rho V_\infty \Gamma \tag{3.1}$$

The lifting line theory represents a straight wing with high aspect ratio reasonably well, however when sweep is introduced or the aspect ratio becomes lower the accuracy is poor [23]. To overcome this several of these lifting lines can be placed in parallel, over the chord of the wing. This creates a lattice of horseshoe vortices on the wing, where each vortex represents a small lifting surface. A schematic of such a vortex-lattice system is shown in Figure 3.2. Here the trailing vortices are shown as separate, however, in the implementation they will like on top of each other.

At each point P the induced velocity, due to all the vortices, can be calculated using the Biot-Savart law, Equation (3.2). Here $\Gamma$ is the vortex strength, $\overrightarrow{dl}$ is the segment of a vortex filament, which causes the induced velocity and $\overrightarrow{r}$ is the vector to the filament. Since there is no flow through the wing itself, the flow tangency

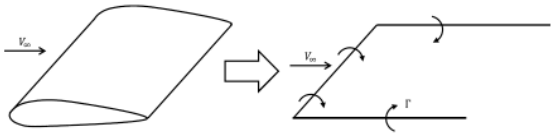

Figure 3.1: Representation of a wing as a horseshoe vortex [23]

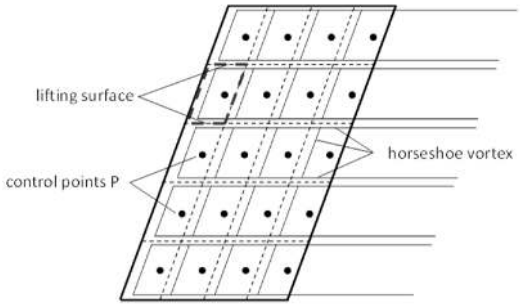


Figure 3.2: Representation of a wing as vortex lattice [23]

condition states that the normal velocity at the surface of the wing must be zero. Now the vortex strengths, Γ, can be determined such that the normal velocity at the wing surface is zero. In the vortex-lattice method implementation the control point P is set at 75% of the chord of the lifting surface, while the vortex is placed at 25%. This gives a set of equations, which can be solved numerically. Each lifting surface can be rotated with the local camber line to provide more accurate results.

$$\vec{v} = \frac{\Gamma}{4\pi}\frac{\vec{dl}\times\vec{r}}{\vec{r}^{\,3}} \tag{3.2}$$

### 3.1.2. VORTEX PANEL METHOD

A way how 2D shapes can be modelled is the vortex panel representation. The vortex panel is a method to numerically solve the flow over a lifting body. For this method, a number ($m$) of panels are placed along the outer surface of the airfoil, with a given vortex strength per unit length ($\gamma$). An illustration of this is in Figure 3.3. The velocity potential at each panel is given by Equation (3.3). The velocity potential due to all the panels at the control point in panel $i$ is given by Equation (3.4). Here $\gamma(s_j) = \gamma_j + (\gamma_{j+1} - \gamma_j)\frac{s_j}{S_j}$.

$$\Delta\phi_j = -\frac{1}{2\pi}\int \theta_{pj}\gamma_j ds_j \tag{3.3}$$

$$\phi(x_i, y_i) = V_\infty(x_i cos\alpha + y_i sin\alpha) - \sum_{j=1}^{m}\int_j \frac{\gamma(s_j)}{2\pi} tan\left(\frac{y_i - y_j}{x_i - x_j}\right) ds_j \tag{3.4}$$

Since there is no flow through the surface of the airfoil, the normal velocity must be zero at control points in the panel. This means that the relation in Equation (3.5) must be true. Finally, this leads to Equation (3.6), which can be solved after further manipulation, which is outside of the scope of this text. The only unknown in this equation, if the shape is known, is the vortex strength. However, as there are $m$ control panels, there are $m$ equations and $m$ unknowns. Further more, the Kutta condition must be satisfied. The Kutta condition states that for an airfoil, at a given angle of attack, the vortex strength around an airfoil is such that the flow leaves the trailing edge smoothly. This means that if the trailing edge is of a finite angle, the trailing edge becomes a stagnation point. If the trailing edge is cusped, the velocity leaving the airfoil at the top and bottom have the same magnitude and direction. Which leads to the fact that the strength of the vortex sheet at the trailing edge is zero [23].

With the strength of each vortex known, the final lift per span can be calculated using the Kutta-Joukowski theorem, in the form of: $L' = \rho_\infty V_\infty \sum_{j=1}^{n} \gamma_j s_j$.

$$\frac{\delta}{\delta n_i}\phi(x_i, y_i) = 0 \tag{3.5}$$

$$V_\infty cos(\theta_i - \alpha) - \sum_{j=1}^{m}\int_j \frac{\gamma(s_j)}{2\pi}\int_j \frac{\delta\theta_{i,j}}{\delta n_j} ds_j = 0 \tag{3.6}$$

There are of course limits to this method. One of the limits is that it assumes constant values of vortex strength over a panel. Thus the panels need to be small enough to ensure accurate results, especially at the curved regions of an airfoil. There are also numerical limitations since the vortex strength of each panel is discrete and can lead to jumps in vortex strength from one panel to the next [23].

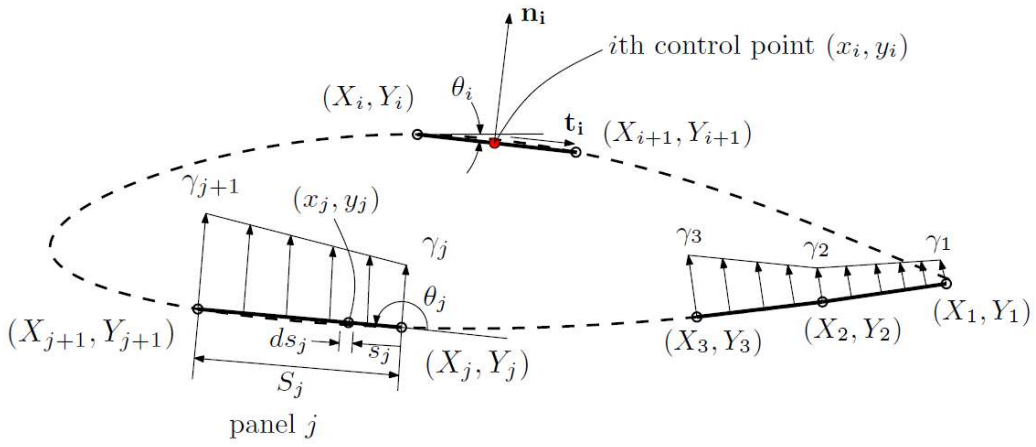


Figure 3.3: Vortex panel representation [27]

### 3.1.3. MAXIMUM LIFT

As noted before, the maximum lift is relevant when looking at flight at the border and beyond of the normal flight envelope. The maximum lift coefficient is different for a 2D wing section than for the 3D wing. The maximum lift is dependent on the maximum lift coefficient of the airfoil section, at the critical spanwise position and the change in airfoil lift to wing lift. However, the translation from 2D to 3D is mainly dependent on aspect ratio, sweep, twist and spanwise variation of airfoil section[35]. This means in order to compare the maximum lift of a scaled wing and full scale wing, which has been geometrically scaled, one needs to look at the maximum lift at the critical section, which is easier than to do an analysis of the full wing.

The analysis of the 2D section can be done using a panel code implementation, albeit with some modifications in order to accurately predict stall. More on this in Section 3.3.1.

## 3.2. FLAPPED WING AERODYNAMIC ANALYSIS

During the landing and take-off phase of flight high-lift devices are commonly deployed. High-lift devices are deployed in order to improve the airfield performance. Maximum lift coefficients for airplanes without high-lift devices usually does not exceed 1.2 [36]. It can be shown that an increase of maximum lift coefficient from 1.2 to 1.55, can lead to an improvement of drag, during cruise, of 18.3% [36].

### 3.2.1. HIGH-LIFT DEVICES

There are several different configurations for the high-lift devices possible. The first distinction comes from the location on the wing, in front or behind the main element of the wing, called leading-edge and trailing-edge devices, respectively. Within these two categories several further different types exist, see Figure 3.4 for different kinds of trailing edge flaps. here the focus is only on trailing edge devices, as only these are commonly found on regional aircraft within the scope of this study. The common trailing edge flap types found on these aircraft are so-called slotted Fowler flaps. Fowler motion denotes the rearward movement of the flap, which increases the chordline and thus the effective wing area. These flaps increase lift via three main principles. First of all they move rearwards, thereby increasing the chord. Furthermore, the flap hinges down, thereby increasing the camber of the wing section. Finally, it creates a gap between the main element and the flap, called a slot, which has several beneficial properties. A slotted flap induces a circulation effect on the main element of wing, thereby increasing the loading. The higher flow velocity on the trailing element allows the flow to leave the leading element at a higher velocity, reducing the pressure recovery on the forward element, called the dumping effect. This also favours off-surface pressure recovery, which is more efficient than pressure recovery on a wall. Each element also has a fresh boundary layer, this boundary layer is less likely to separate than a boundary layer originating from a previous element [37].

### 3.2.2. ANALYSIS OF A WING WITH FLAP USING A VORTEX LATTICE METHOD

The analysis of the wing can be done using a vortex lattice method, if some workarounds are applied to account for slotted high-lift devices. The maximum lift coefficient can be analysed using the pressure difference

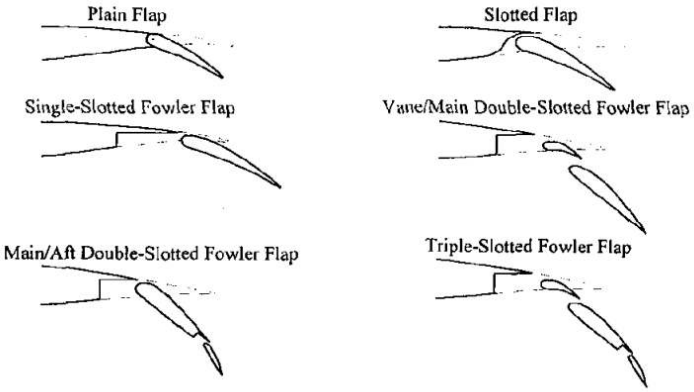


Figure 3.4: Commonly used trailing edge flaps [38]

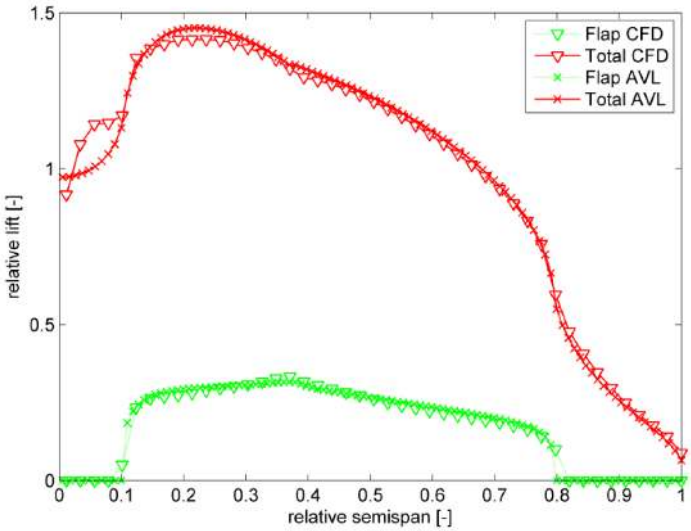


Figure 3.5: Comparison between AVL and a higher order CFD method to model a wing with slotted flaps [40]

rule.

Analysis with VLM is limited to single element wings, thus no slotted leading edge or trailing edge devices can be normally modelled using a VLM. However, using some workarounds the wing can still be fairly accurately modelled using a VLM [39–42]. The high-lift device can simply be modelled as an additional surface, which has the projection area of the high-lift device, at the position where the high lift device normally be. It is the projected surface, since a VLM only models the wing as a 2D surface. The vortex element at the location of the high-lift device must be rotated by the deflection angle, in order to give the best results [39]. The slot between the wing and the high-lift device must be simply modelled by an extension of the main wing surface [41]. More information about the implementation can be found in Section 3.3.2. Figure 3.5 shows an example of using a vortex lattice method -AVL in this case- to model wing with flaps, compared to a more complex computational flow dynamics (CFD) model.

## 3.3. TOOLS USED

The following section will explain the workings of the specific tools used for the analysis.

### 3.3.1. CLEAN WING ANALYSIS

For the analysis of the clean wing the tools used must be able to find the relevant aerodynamic properties of the wing and airfoil. The most important are, as given in Section 2.4, the lift, moment and drag coefficient, as well as the maximum lift. For the analysis of the wing the tool *Q3D* is chosen and for the analysis of the maximum lift *RFOIL* is selected, RFOIL was selected because of the better prediction of behaviour near stall.

**Q3D**

In order to analyse the full wing and not just the airfoil, but still have reasonable calculation time, the quasi-three-dimensional aerodynamic(Q3D) solver is chosen. This routine is much faster and easier to implement than higher fidelity CFD methods, however this is of course at the cost of accuracy [43]. The decision for this method was made in order to be able to evaluate a large number of different flow conditions, airfoils and wing shapes within a reasonable amount of time.

The routine was developed at the faculty of Aerospace Engineering of the Technical University in Delft, a simplified overview is given in Figure 3.6. The calculation is done in several stages. First the lift coefficient and induced drag coefficient of the entire wing are calculated using a VLM. Then using the calculated spanwise lift distribution, the local lift coefficients at several spanwise locations are determined. With simple sweep theory and the planform of te wing, the exact airfoil section perpendicular to the sweep line can be found. Next a panel method is used to, iteratively, calculate the local induced angle of attack and the profile drag properties (friction and pressure). Once the induced angle of attack is converged, the local drag coefficients are transformed back to the freestream values, by use of simple sweep theory [43].

Finally the total profile drag is calculated based on the local drag coefficient and the local section area. Combined with the induced drag found by the VLM, the total drag is now known. With the lift and moment coefficient already known from the VLM, all the required aerodynamic coefficient are now calculated.

The tools used for this analysis are AVL as the VLM and XFOIL for the airfoil analysis.

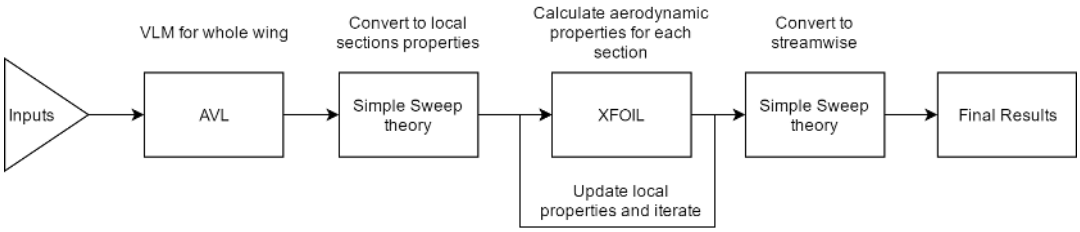


Figure 3.6: Q3D work flow

Q3D has been validated at high Reynolds numbers by Mariens et al. [43], in order to validate the results of Q3D it is compared to windtunnel data obtained by Purser and Spearman [44]. For this test a small wing has been tested in a windtunnel at low speed and Reynolds number of $6.8 \cdot 10^5$. The data for the test can be found in Table 3.1. The results are found in Figure 3.7, it shows a slight difference between Q3D and the test data, the maximum difference is $C_L = 0.05$. A reason for this could be that the lift prediction by AVL is off for low Reynolds numbers, where the viscous effects are more dominant and AVL does not fully take into account the viscous effects on the lift. The quality of Q3D is deemed to be acceptable.

Table 3.1: Data for validation case for Q3D at low Reynolds number

| **Property** | **Value** |
|---|---|
| *Profile* | NACA23012 |
| *Sweep [deg]* | 14 |
| *Span [m]* | 1.52 |
| *Root chord [m]* | 0.38 |
| *Taper ratio [-]* | 1/3 |
| *Reynolds number [-]* | $6.8 \cdot 10^5$ |
| *Mach number [-]* | 0.079 |

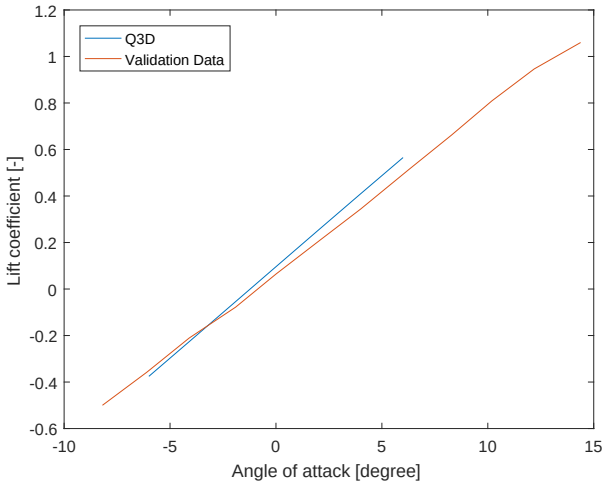


Figure 3.7: Q3D compared to test data at low Reynolds

**SIMPLE SWEEP THEORY**

With the use of simple sweep theory, properties of a swept wing can be related to the properties of the freestream air flow. Say, a wing is subjected to a freestream flow of $V_\infty$ and consider two cases, one straight wing and a sweep, oblique wing, as in Figure 3.8. The flow for the oblique wing can be split into three components, $u$,$v$,and $w$. The flow of the straight wing can be split into two parts: $u'$ and $w'$. $V_\infty$ can be related to $u_\infty$ by $V_\infty = \frac{u_\infty}{cos\Lambda}$, where $\Lambda$ is the sweep angle. Using this relation and Equations (3.7) and (3.8) the straight velocity can be rewritten as in Equation (3.9).

$$V^2_{oblique} = u^2 + w^2 + v^2_\infty \tag{3.7}$$

$$V^2_{straight} = u'^2 + w'^2 \tag{3.8}$$

$$V^2_{straight} = \frac{u^2 + w^2}{cos^2\Lambda} \tag{3.9}$$

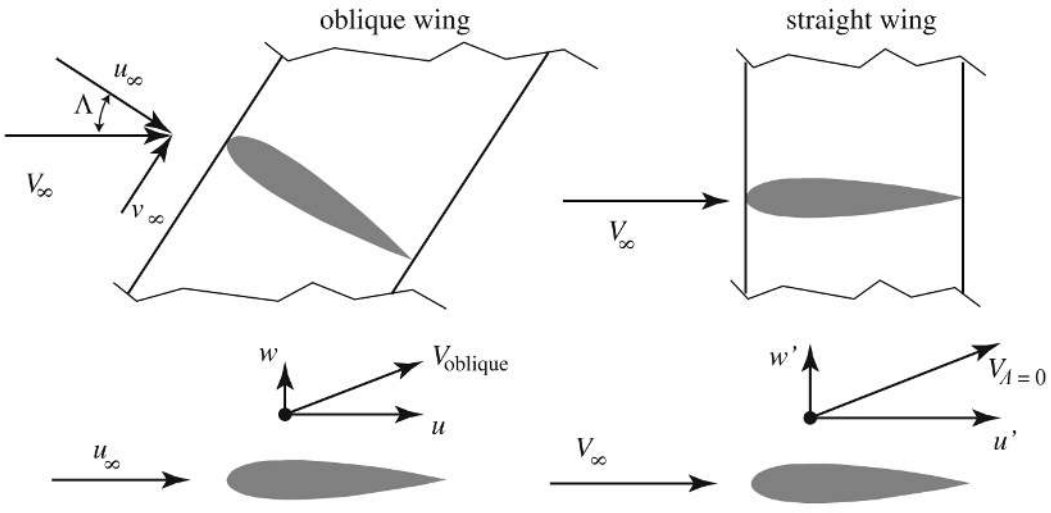


Figure 3.8: Visualisation for simple sweep theory [6]

Now the two equations can be related to each other to give Equation (3.10). In order to relate this to the lift and moment coefficient, the pressure coefficient is used. Equation (3.11) has the pressure coefficient for

incompressible flows. Combining Equation (3.11) and Equation (3.10) gives Equation (3.12), this means it is possible to relate the freestream pressure coefficient to the swept pressure coefficient for incompressible flows, using only the sweep angle. This result can be used to determine the relations of the lift and moment coefficients, as in Equations (3.13) and (3.14). [6]

$$\left(\frac{V_{oblique}}{V_\infty}\right)^2 = sin^2\Lambda + \left(\frac{V_{straight}}{V_\infty}\right)^2 sin^2\Lambda \tag{3.10}$$

$$C_P = 1 - \left(\frac{V}{V_\infty}\right)^2 \tag{3.11}$$

$$C_{p,swept} = C_p cos^2\Lambda \tag{3.12}$$

$$c_{l,swept} = c_l cos^2\Lambda \tag{3.13}$$

$$c_{m,swept} = c_m cos^2\Lambda \tag{3.14}$$

**AVL**

AVL (Athena Vortex Lattice) is VLM, Section 3.1.1, which can calculate on simple, thin lifting surfaces. AVL is developed by Mark Drela, is a Fotran-based code, has short runtimes and is able to run in batch mode [45].

AVL, just like any VLM, has some limitations:

- The results are only valid for small angles
- The method is only applicable for thin lifting surfaces
- Quasi-steady flow is assumed, so no unsteady vortex shedding is taken into account
- The vortex lattice method is based on potential flow and does not include viscous effect, directly

A VLM is an inviscid method, thus this will seem not suited for investigation of scaling, where viscous effects are important. However, one way the viscous effects do come into effect for this implementation of the VLM is by the lift curve slope. The lift curve slope of the airfoil is used for the calculation of the lift. As already noted in Section 2.3 scaling will cause a more pronounced decambering effect, which results in a lower lift curve slope. As a default a slope of $2\pi$ is assumed, but since this is only valid for very thin airfoils, the method is updated to calculate the lift curve slope for the airfoil. The lift curve slope is calculated using RFOIL or MSES, where applicable.

**XFOIL**

XFOIL is a interactive program for the analysis and design of subsonic airfoils. It is an implementation of a linear-vorticity stream function panel method, which is a further development of the vortex panel method mentioned in Section 3.1.2. XFOIL solves the viscid boundary layer and wake, and inviscid flow field equations simultaneously using a global Newton method. The viscous calculations are done based on the wake from the inviscid wake calculations. This means that the viscous effects are not fully incorporated for the lift calculation. The transition is modelled by the $e^n$-method [46]. It allows for fast analysis of airfoils at low Reynolds numbers with good accuracy, also when separation bubbles occur. The compressibility correction is done using the Karman-Tsien correction [47].

The advantage of XFOIL is that it a fast program, delivering results within seconds, and provides good results. However, the solutions are not reliable for when the flow around the airfoil starts to separate, which is around stall. There is also the limitation that the viscous effects are not taken into account for the lift calculation.

#### RFOIL

The maximum lift is calculated using RFOIL. For this RFOIL was chosen, instead of XFOIL, as it is better in predicting the behaviour near stall. For the use of Q3D XFOIL is still used. RFOIL is a modified version of XFOIL, developed at the Delft University of Technology [48]. The modifications are mainly to improve the behaviour of the flow around and post-stall. The original XFOIL was not able to calculate airfoil parameters after stall. The modifications made to XFOIL are improvements to the numerical stability in XFOIL and adjustments of the boundary layer equations. Originally developed for wind turbine airfoil calculations, it also includes rotational flow effects.

In general the performance of RFOIL is not perfect and can, especially near stall, show some deviations [48]. As it is fully able to capture all the non linear behaviour there. However, it is better at predicting airfoil behaviour near stall than XFOIL and still is able to run in a fairly fast amount of time. Broadly said, RFOIL under predicts the drag coefficient, the lift curve near stall is reasonable and the post stall behaviour is too optimistic [48]. RFOIL has also been verified to provide good results at low Reynolds numbers, which is what is also of interest to this study.

### 3.3.2. FLAPPED WING AERODYNAMIC ANALYSIS

For the analysis of the wing with flap, ideally an analysis method for the complete wing with flap is desired, in order to calculate the lift, moment, drag coefficients, and maximum lift. As explained in Section 3.2.2 a vortex lattice method can be used to a quasi-3D analysis of the wing with flap, as the vortex lattice method AVL is selected. An analysis of the 2D airfoil is also possible, *MSES* is used for this. The maximum lift will be determined for the entire wing, using a semi-empirical method called the *Pressure Difference Rule*. The pressure difference rule only requires 2D inviscid analysis, which is doable with basic tools, paired with empirical factor to determine the maximum lift of a wing.

#### INTEGRATION OF FLAP WITH AVL

Section 3.2.2 has the theoretical background to the implementation of a (slotted) flap in AVL. Here the actual implementation as used in this study is described.

An overview of the implementation is given in Figure 3.10. As the first step, the lift curve slope is calculated at each of the sections, using MSES. The two surfaces which are the main wing and the flap, are given the lift curve slope of the combined analysis of the two elements in MSES. This is done in order to accurately represent the beneficial mutual interaction between the two elements. Next the input is made for AVL, where the main wing is taken as the clean planform, that it is, and given the correct local camber line. The flap is modelled as the surface projection on the x,y-plane, with the gaps between the main element and the gap closed with the extension of the flap surface. The camberline is rotated as necessary for the flap angle, but reduced with the flap relaxation fraction, as found in Figure 3.14b. This is done because AVL is an inviscid method and the viscous decambering effect needs to be taken into account. The decambering occurs because the flow at the trailing element has an angle, as shed by the boundary layer of the preceding element. Finally, Figure 3.9 shows the implementation of the scaled wing, with trailing edge flap in AVL.

A short study is done into sensitivity of the integration of AVL with flaps, to the number of vortices per element. Figure 3.11 has the results for both different number of chordwise and spanwise vortices. All these runs have been done on the full scale wing, with flaps at 15 deg, the vortices are spaced with a cosine spacing, with a default of 10 spanwise and 5 chordwise vortices. A clear effect is visible on the lift coefficient for less than 6 chordwise, after that the values are within 0.5%. For the spanwise vortices most differences occur before approximately 10 spanwise vortices per element. For all these cases the calculation time of AVL only is approximately 10-12 seconds, so that is not a big issue. Here the calculation times are very erratic and suggest an optimal calculation time, with good accuracy, could be achieved with 11 spanwise and 7 chordwise vortices. Figure 3.12 has the spanwise loading diagram for two different number of spanwise vortices (solid and dashed lines), as can be seen the difference between the two solutions is minimal.

In further analyses 11 spanwise and 7 chordwise vortices will be chosen for the AVL analysis with flap.

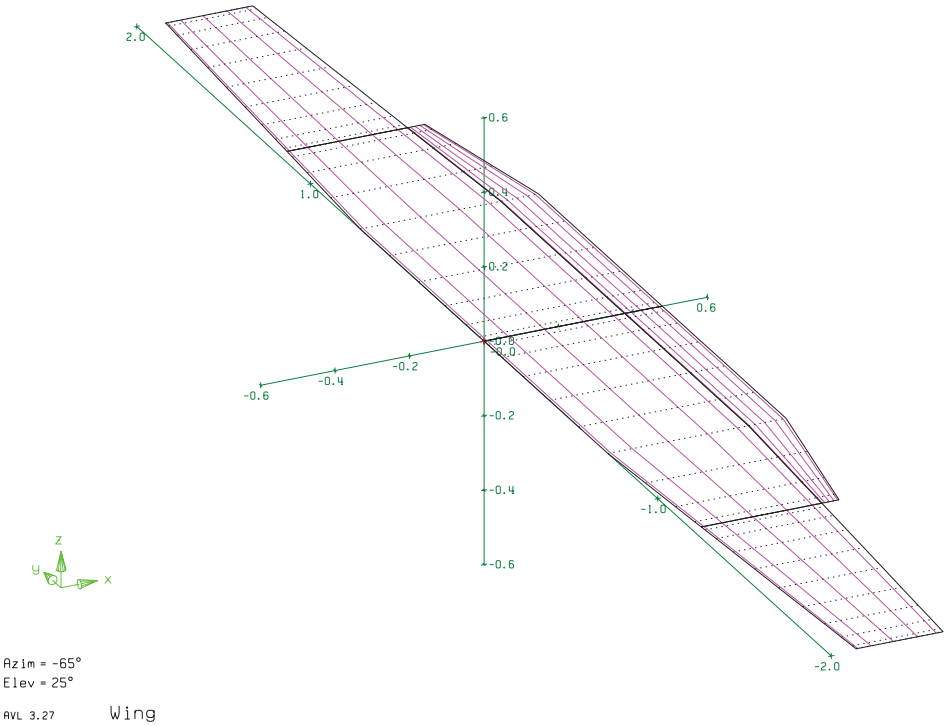


Figure 3.9: Visualisation of the scaled wing in AVL

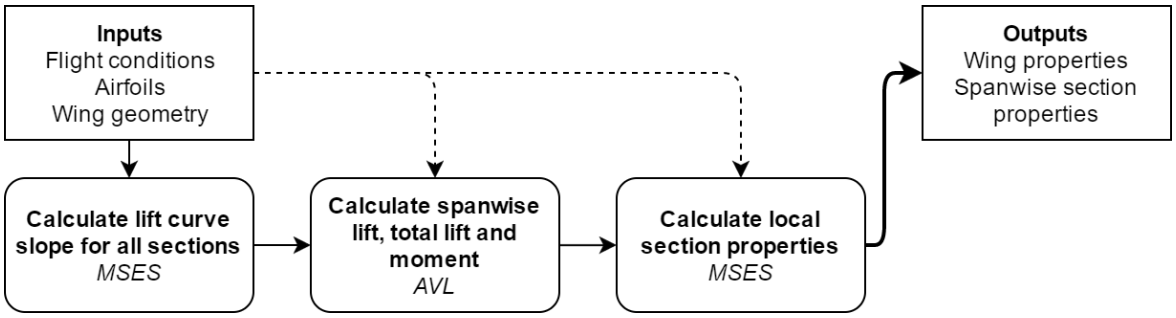


Figure 3.10: Diagram of calculation of AVL with flap

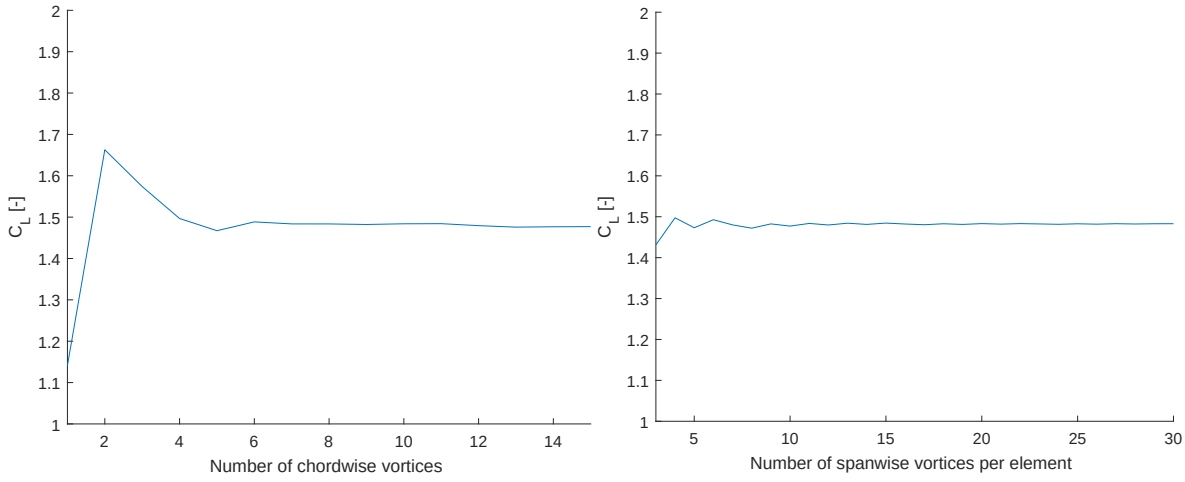


(a) Influence of number of chordwise vortices

(b) Influence of number of spanwise vortices

Figure 3.11: Influence of different number of vortices

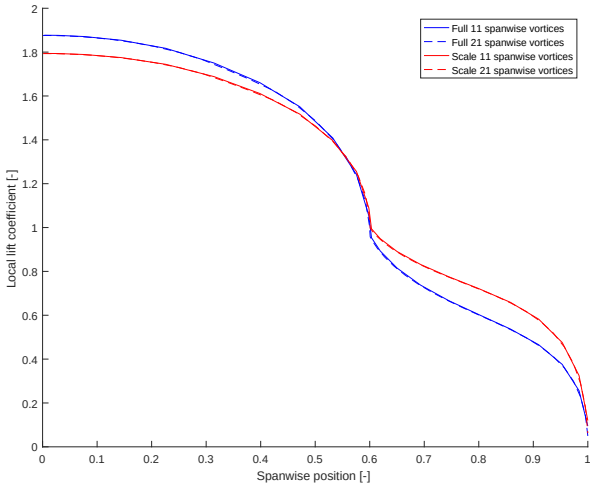


Figure 3.12: Spanwise loading with different number of vortices

**MSES**

MSES is a multi-element airfoil analysis and design tool. It is an Euler solver, which permits both inviscid or viscid analysis. MSES automatically generates a mesh, by intersecting the inviscid streamlines and lines normal from the surface of the airfoil. MSES couples the viscous and inviscid calculations, in order to achieve fast convergence and solutions. The Euler-equations are coupled to a two-equation integral boundary-layer formulation. The prediction of the transition is done using the $e^n$-method [46]. The entire equation set is solved as a fully coupled nonlinear system, by a Newton method. This couples the discrete inviscid Euler equations with the discrete boundary layer equations, which require simultaneous solving. Results show that it is accurate in predicting airfoil performance, including separation bubbles [47].

**PRESSURE DIFFERENCE RULE**

First developed in 1994 the Pressure Difference Rule (PDR) is a method used to predict the maximum lift of a (complex, multi-element) wing [49]. The PDR is a good way to approximate the maximum lift on a wing, with only the use of inexpensive CFD techniques.

The PDR states that an element will stall when the difference between the peak pressure coefficient and the pressure coefficient at the tailing edge reach a certain value. The pressure difference at maximum lift depends on the free stream Mach number and the local chord Reynolds number of the element, see Figure 3.14. A clear benefit of this method lies in the fact that these pressures may be calculated at inviscid conditions, which makes for low computational times and straight forward, existing, straightforward panel codes to be used.

The way the PDR is implemented here is as follows, see Figure 3.13. First, the wing is split in to a number of sections, based on user input. First the local wing cross-sections is determined, based on thickness distribution and the presence of trailing edge flaps. At all the sections the local airfoil and Reynolds number is calculated. For each of these sections, based on local Mach and Reynolds number the critical pressure difference is determined, by interpolating the graphs from Figure 3.14a. Next the pressure coefficient difference, between the peak and the trailing edge is calculated for each section, for an initial angle of attack. This angle of attack is later updated. The calculation of the pressure coefficients is performed using MSES and at inviscid conditions. If the difference is greater than the critical difference, the angle of attack is lowered, if it is smaller then the angle of attack is increased. In such a way the critical angle of attack is found through an iterative process. The exit-criterion for this loop is when the actual pressure difference is within a limit, so $\Delta C_{P,actual} - \Delta C_{P,critical} < \epsilon$. At this point one, or more, sections have reached the limit pressure difference and thus will stall. In this implementation only the main wing section is investigated, since it is assumed that the peak pressures on the main wing are higher and thus the main wing will stall before the flap. Should there be a leading edge device, then this could also become the critical element, however in the current use case, no leading devices are present. For the geometries used in the current study, the pressure difference of the main element is much larger than that of the flap. See Figure 6.8a as a reference.

The value of $\epsilon$ is chosen to be 0.05, which is a margin of 0.7% for Reynolds numbers at 2 million, which corresponds to a pressure difference of 7. At a Reynolds number of 9 million the critical pressure ratio is 14, so a margin of 0.05 is 0.35% of 14. For higher Reynolds numbers, and higher critical pressure differences, the margin is thus even smaller, ensuring accurate results.

Another assumption lies in the fact that the maximum lift is reached as soon as one section reaches its maximum lift. It is likely that the section will stall after it has reached its maximum lift and that the stall will spread to the rest of the wing. It might be possible that the wing can generate a little more lift after a single section has reached its maximum, but it is not known if this is always the case and the magnitude of this increase in maximum lift is assumed to be also small.

The maximum lift coefficient of the wing is then calculated by calculating the inviscid lift at each of the sections, at the angle of attack which was found in the previous steps. This section lift is then multiplied by the relative chord, to get the weighted maximum lift of the different sections, this will not be equal to the maximum lift actually achieved by the wing, but is a good approximation. Should there be twist in the wing, then this is also accounted for. Figure 3.15 shows how the maximum lift is determined, on the x-axis there is the spanwise position and on they y-axis it shows the pressure coefficient difference between the peak and trailing edge. The two lines of $C_L$ indicate the spanwise pressure coefficient distribution and the Pressure Difference Rule line indicates the local critical pressure coefficient ratio. As can be seen here the maximum lift coefficient of the wing is 1.04, as this is when the pressure coefficient ratio becomes critical at 0.87 wingspan. A large limit to the method is that the pressure difference is no longer known for flows with a Reynolds below

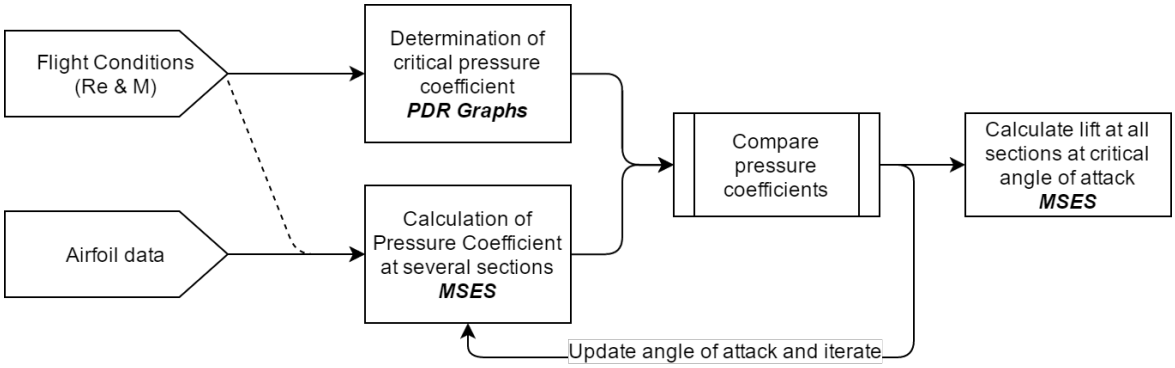


Figure 3.13: Pressure difference rule work flow

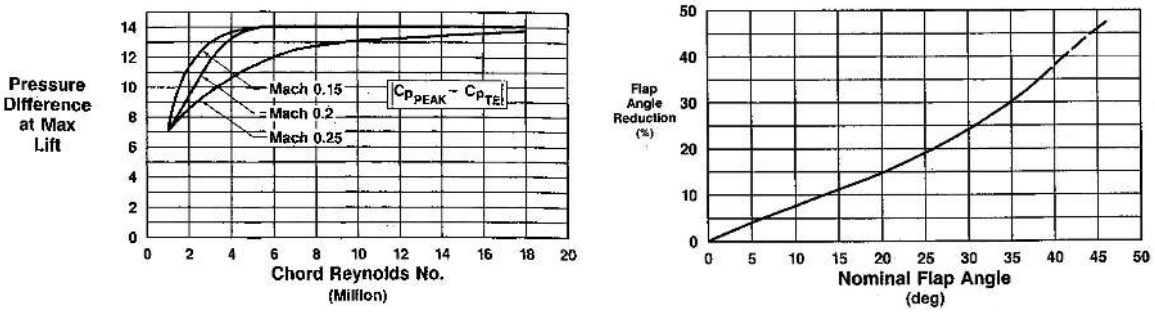


(a) Critical pressure coefficient

(b) Flap relaxation from viscid to inviscid

Figure 3.14: Graphs used for the Pressure Difference Rule [49]

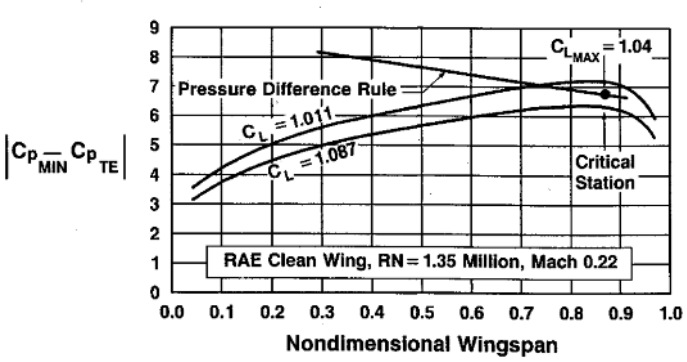


Figure 3.15: Maximum lift prediction using the PDR [49]

1 million, as can be seen in Figure 3.14a. It is possible to extrapolate the data to below a Reynolds of 1 million, but this is not validated and becomes very uncertain when looking at the scaled case, which as a Reynolds number of approximately $5.3 \cdot 10^5$. Also there is only data for a few Mach numbers available, again this can be extrapolated, but the uncertainty increases.

Another limit is the validity for the type of wings for which the PDR can accurately predict the stall. Good results have been found for swept wings with high-lift devices [49], however, for the unswept wings without high-lift devices the PDR is not so accurate in predicting stall [42]. Thus the PDR will only be used for the case for wing with flaps.

**Sensitivity to Settings** A brief investigation into the sensitivity of the settings of the PDR is shown in Figure 3.16. Here the influence of the number of sections on the maximum lift found is investigated. The test conditions were a flap setting of 15 deg and the full scale model as described in Section 2.6. All the sections are spaced with an equidistant to the next.

As can be seen already with 2 sections the value found for the maximum lift is within a close margin of the value found for a greater number of sections. This means that large sections of the wing reach the same conditions for maximum lift. In subsequent studies 6 number of sections will be used, in order to capture possible, unknown, local effects properly, while still having good computational times.

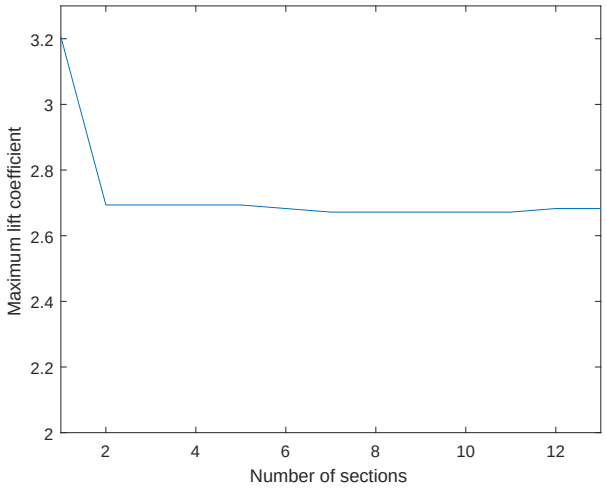


Figure 3.16: Sensitivity to the number of spanwise sections

## 3.4. CONCLUSION

In the preceding chapter the methods that will be used in order to scale te aircraft and analyse the clean and wing with flap have been discussed. Also the use case which this research will use has been outlined. For the clean wing analysis, a quasi-3D analysis called *Q3D* will be used, which is an combination of a VLM and a vortex panel method. This allows for fast evaluation, while still having reasonably accurate results. AVL is the implementation of the VLM employed here, along with *XFOIL* as the vortex panel method, further, simple sweep theory is used to relate these two with each other. The maximum lift is compared based on the maximum airfoil lift coefficient found by *RFOIL*. RFOIL is a modification of XFOIL, in order to allow for better prediction of the flow near the stall region.

For the analysis of the wing with flap again AVL is used, with the flap modelled as an additional lifting surface. For the sectional properties the vortex panel method *MSES* is used. The maximum lift is determined with the use of the semi-empirical *Pressure Difference Rule*, which states that there is a relation between the pressure difference on the airfoil section and stall occurring. The PDR is not used for the clean wing, as the method was found to be provide inaccurate results for clean, unswept wings.

Using these tools both the full scale and scaled wing can be evaluated using the same tools, in a relatively short time, to allow for different configurations.

The tools selected for the analysis are limited in the way they incorporate the viscous effects. AVL is mainly a inviscid method, which incorporates some viscous corrections by the alteration of the lift-curve slope. This means that this method is limited in predicting the effects of scaling, which is mainly a viscous effect.

The methods for the two 2D airfoil analysis (XFOIL, RFOIL and MSES) have shown results, also at lower Reynolds numbers and are able to predict laminar separation bubbles accurately. Even though the vortex panel methods are at their core potential methods, inclusion of a viscous boundary layer improves the accuracy of them.

# 4

# METHODOLOGY OF THE WAKE ANALYSIS

With a base now laid out to do the aerodynamic analysis of the wing, it is time to extend this into the analysis of the wake behind the wing. In order to calculate the aerodynamic properties, required for the wake analysis, the methods as described in Chapter 3 are used. This chapter will introduce the methods selected for this purpose, first for the clean wing in Section 4.2, then for the wing with flap with Section 4.3. Then the implementation of the calculation of wake is described in Section 4.4. Finally the calculation on the wake itself is given in Section 4.5. Further background information on the ESDU methods used for downwash and wake location calculation can be found in Appendix A.

## 4.1. WAKE SURVEY PLANE ANALYSIS

The wake survey plane is an arbitrary-sized plane placed at a certain distance behind the wing. This fictional plane is used in order to investigate the effects of scaling on objects placed in the wake of the wing. These objects could be a traditional horizontal and vertical tail, but also a combination of propulsion and control surfaces. Thus in further analyses this wake survey plane is placed at the approximate location of the horizontal tail, for the ATR72, unless specified otherwise.

To determine how the flow field looks at this location several steps have to be taken: the size and magnitude of the wake are to be determined, the location of the wake needs to be calculated and the downwash computed.

To perform the analysis at the wake survey plane, methods are needed to calculate the position of the wake, the magnitude of the wake and the downwash. In order to calculate the downwash and wake location two methods developed by the ESDU (*80020 & 97021*) are used. For the magnitude and width of the wake the method developed by Schlichting is used. These methods are further discussed below.

## 4.2. DOWNWASH OF THE CLEAN WING - ESDU 80020

The method selected for the calculation of the wake properties of the clean wing is the ESDU80020, *Average Downwash At The Tailplane At Low Angles Of Attack And Subsonic Speeds*[50]. It is a method provided by the ESDU, which is British engineering advisory organisation. The method is selected for their fast computation time, fair accuracy, while only needing a limited amount of inputs.

The equation for the calculation of the downwash is given by Equation (4.1). It states that the downwash is comprised of a zero-lift downwash, a contribution dependent on the change of downwash with angle of attack with the difference between the angle of attack and zero-lift angle of attack ($\alpha_0$). In this method it is assumed that the downwash gradient is constant for the angles of attack used in this study, and scales linearly with vertical distance from the wake, as shown in Figure 4.1. Here $\zeta_t$ is the dimensionless height above the wake -made dimensionless by dividing by the the half wing span.

$$\varepsilon = \varepsilon_0 + ((\frac{d\varepsilon}{d\alpha})(\alpha - \alpha_0) \tag{4.1}$$

The method works as follows, first the downwash gradient at the wake location is calculated, based on lifting surfaces method and empirical corrections. Further corrections are done for the presence of te body and the

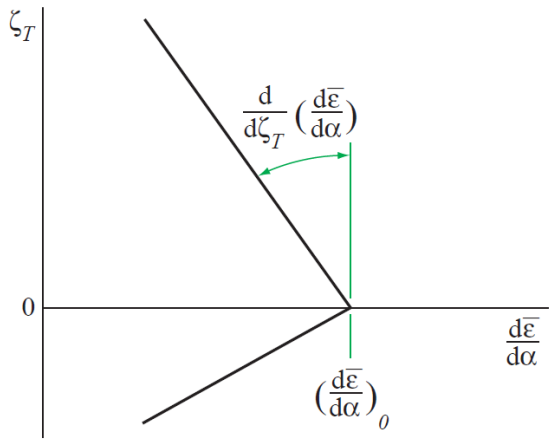


Figure 4.1: Effect of height on downwash gradient[50]

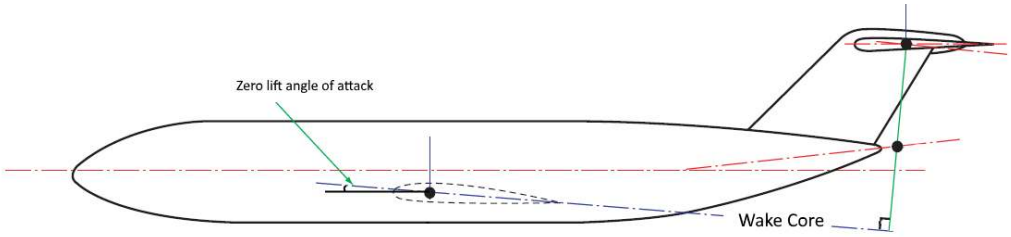


Figure 4.2: Location of the wake core for a clean wing, adapted from [50]

tailplane height, these are based on experimental data. Finally, the downwash at zero-lift is calculated using, again, experimental data. This is all done in the application provided by ESDU. The method allows for the inclusion of the effects of body, thus this is also included, in contrast to the analysis of the wing, where this is not done.

The method has the following limitations and assumptions. It assumes a flat vortex sheet, so the downwash is constant over the entire tailplane/wake survey plane. It assumes attached, linear flow, so only low angles of attack are possible. Furthermore, the vortex sheet is assumed to be in the zero-lift plane. There are also limits to the method, based on the type of configurations used to build the model, these are listed in Table 4.1, these are also the factors which are the input for the model. $\xi$, $\eta$, and $\zeta$ are distances in the x,y, and z direction respectively, all made dimensionless by dividing by the semi-span. Even though the minimum Reynolds number listed in Table 4.1 is above the Reynolds number for the scaled wing, this method will still be employed, since it is found that the influence of Reynolds number on the results of the ESDU80020 method are minimal.

In order to check the validity of the assumption that the vortex is flat over the span literature is consulted. An investigation looking at roll-up of the wake due to the tip vortex has been conducted by Vaessen [51]. In this investigation the vortex was analyzed at different distances behind a high aspect ratio (8) and swept (26 degrees) wing. It was found that the tip vortex never exceeded approximately further than 15% inboard from the tip. This means that for the current case with a wake survey plane extending 11% outboard from the centre the vortex will still remain flat.

Table 4.1: Limits to the ESDU80020 model [50]

| | $AR$ | $\lambda$ | $\Lambda_{0.25}$ | $w/2s$ | $\xi$ | $\eta$ | $\zeta$ | $Re \cdot 10^6$ |
|---|---|---|---|---|---|---|---|---|
| Minimum | 2 | 0 | 0 | 0.1 | 0.5 | 0.2 | -0.2 | 0.5 |
| Maximum | 12 | 1 | 52 | 0.2 | 3 | 0.8 | 0.6 | 15 |

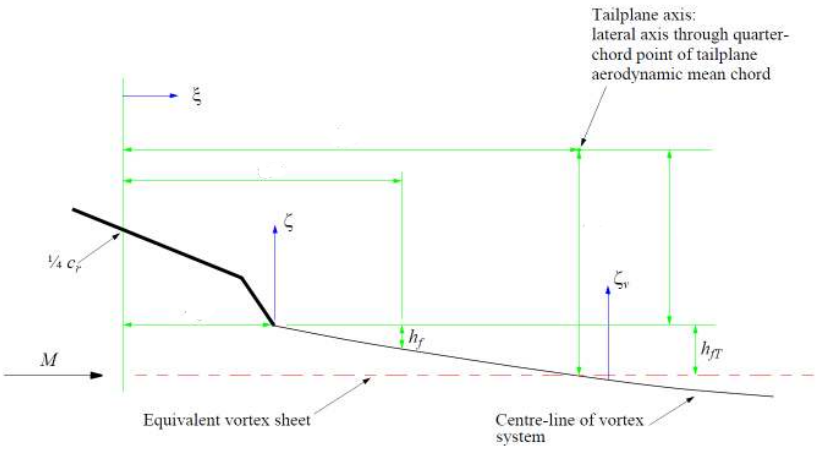


Figure 4.3: Location of the wake for wing with flap [52]

## 4.3. DOWNWASH DUE TO FLAP DEPLOYMENT - ESDU 97021

ESDU 97021 *Effect of trailing-edge flap deployment on average downwash at the tailplane at low speeds* [52], is a semi-empirical method to calculate the downwash at the horizontal tailplane. It is similar to the ESDU 80020 in that it gives only a mean value for the downwash across the tailplane, or the case of this research the wake survey plane. The method is based on calculations for straight untapered wing with a simple flap, with further correction factors for the different geometries. These correction factors are mainly based on empirical data. The effects of flap deployment are based on a system of horeshoe vortices, which represent the flap loading, from this the downwash can be calculated using the Biot-Savart Law (Equation (3.2)). This vortex sheet starts out straight, but curves as it moves downstream. To simulate this, a equivalent vortex sheet can be determined, such that is straight, but at the same height where the vortex would be in case of a curved vortex shed from the wing. Figure 4.3 shows this equivalent vortex sheet. Normally a vortex sheet will be shed from the flap trailing edge and not be straight, but curve in order to align itself with the flow direction. In order to simulate this, the equivalent straight vortex sheet stemming from the wing quarter-chord point is vertically displaced twice, once to the trailing edge of the flap and then to the location of the vortex sheet. The location of the vortex sheet is matched according to empirical data for the downwash behind the wing.

It was found that difference in flap type did not have a large impact on the wake location and downwash [52].

Table 4.2: Limits to the ESDU97021 model [52]

| | $AR$ | $\lambda$ | $\Lambda_{0.25}$ | $b_f/b$ | $c_f/c$ | $\xi$ | $\eta$ | $\zeta$ | $M$ |
|---|---|---|---|---|---|---|---|---|---|
| Minimum | 1 | 0 | 0 | 0.4 | 0.1 | 0.5 | 0.2 | 0.05 | 0 |
| Maximum | 12 | 1 | 60 | 1 | 0.4 | 2 | 0.6 | 1 | 0.4 |

## 4.4. IMPLEMENTATION OF THE WAKE CALCULATION

First the downwash of the clean wing is calculated as follows: the zero-lift angle of attack is calculated, using Q3D, to give the proper geometric angle of the entire wing. Next the zero-lift downwash and the downwash gradient are calculated using the ESDU80020 method. Using the ESDU80020 method the location of the equivalent vortex sheet can also be found, this gives the location of the wake core.

Using the drag of the local airfoil section, the local wake thickness and velocity deficit are calculated, over the complete wake survey plane.

For the wing with flap case, first the clean wing is calculated as described above, then the additional lift contribution of the flap is calculated using AVL integrated with the flap, this value is required for the ESDU97021 method. Again, the downwash is calculated using the ESDU method and added to the value found for the clean wing. Also the wake location can be determined from the location of the equivalent vortex sheet. The flowcharts for this procedure are found in Figure 4.4.

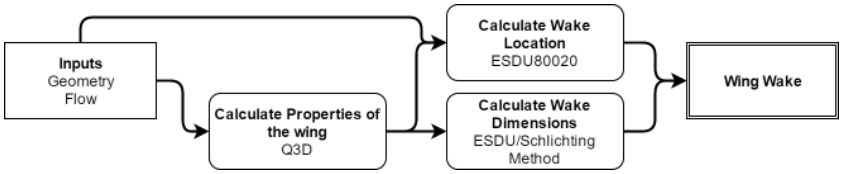


(a) Flowchart for the clean wing wake

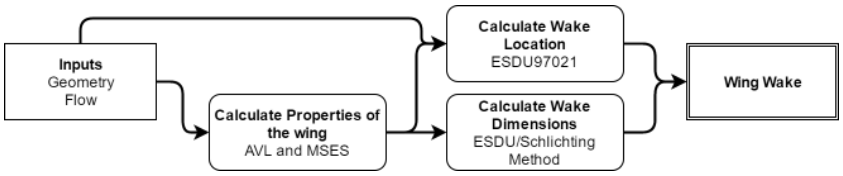


(b) Flowchart for the flapped wing wake

Figure 4.4: Flowcharts for wake analysis

### 4.4.1. WING AND FLAP WAKE

In order to correctly calculate the lift generated by the flap, the wing is analysed using AVL for both the clean wing and the wing with flap. Using MSES and the local lift coefficient at each station the local drag of the sections can be calculated, similar as the Q3D method.

For the clean wing, the wake shed by the wing is assumed to be in the zero-lift plane, which means it is at the same z-location as the wing for the zero-lift angle of attack. This means to find the location of the wake Equation (4.2) can be used.

$$z_{wake} = tan(\alpha_0) x_{tail} \tag{4.2}$$

Conveniently the ESDU 97021 method gives the location of the equivalent vortex sheet, thus this also gives the wake location. Combining this with the local drag coefficient gives the wake thickness and magnitude. As illustrated in Figure 4.3, $h_{fT}$ is the location of the wake at the tail.

## 4.5. WAKE WIDTH AND VELOCITY DEFICIT

The properties of the wake can be calculated two ways, one method developed by Schlichting [25] and an ESDU method [53]. The velocity deficit denotes the reduction in velocity in the wake, relative to the freestream velocity, see Equation (4.3). Both are used and will be evaluated in the results in Chapter 7. The equation for the velocity ratio as defined by Schlichting can be found in Equation (4.4), here $b$ is the wake width, given by $b = 0.569\sqrt{x c_d c}$.

$$V_{deficit} = \frac{V_\infty - V_{local}}{V_\infty} \tag{4.3}$$

$$\frac{V}{V_\infty} = \frac{\sqrt{10}}{3.24}\left(\frac{x}{c_d c}\right)^{-0.5}\left(1-\left(\frac{y}{b}\right)^{3/2}\right)^2 \tag{4.4}$$

Equations (4.5) to (4.7) describe the equations for the wake width and strength determination, from ESDU. Equation (4.5) states that the wake width is a function of chord length Equation (4.6) shows the wake strength at the core of the wake, expressed in dynamic pressure, $q = \frac{1}{2}\rho V^2$. It is dependent on the drag coefficient and the distance behind the wing. Finally Equation (4.7) relates the strength at the center of the wake with the strength at any point $y/b$ in the wake.

$$b = \frac{1.1c}{2}\sqrt{C_d x} \tag{4.5}$$

$$\frac{q_c}{q_\infty} = 1 - 2\sqrt{\frac{c_d}{x}} + \frac{c_d}{x} \tag{4.6}$$

$$\frac{q_{loc}}{q_\infty} = (1 - \frac{q_c}{q_\infty})\frac{y}{b}^{1.75} + \frac{q_c}{q_\infty} \tag{4.7}$$

Both methods include the same terms, namely the chord, drag coefficient and the distance behind the wing and are similar of form.

## 4.6. CONCLUSION

The properties of both the scaled as well as the full scaled wake will be calculated using *ESDU80020* and *ESDU97021*, for clean and flapped wing respectively. Both methods are semi-empirical methods and use a simplification where to place the vortex sheet. The properties of the wake itself can be calculated using either a method by ESDU or a method by Schlichting. The aerodynamic properties are calculated using the methods discussed in Chapter 3.

The wake models used in this study this cannot guarantee the validity of the exact found numbers. They are indicative of the difference found between the full and scaled case, as both the scaled and full scale wing are subjected to the same methods.

# 5

# OPTIMIZATION METHODOLOGY

This current chapter limits itself to the optimization of the clean wing. This is done because of the difficulties with obtaining convergence for multi-element airfoils and the associated difficulties of using such a method in an optimization scheme. The workflow can be found in Figure 5.1. On the left side we see the generation of the reference data, this is done using the use-case described in Section 2.6 and the tools as described in the previous sections. On the right side is the optimization loop, the same tools are used here as for the reference data. The data is compared in the objective function, which is then used by the optimizer. The optimizer in turn changes the airfoil shape, in order to reach a minimum value of the objective function.

The objective function is explained in Section 5.1, after that the parametrization of the input is discussed in Section 5.2. After that the different optimization algorithms are explained in Section 5.3. Finally the chapter is concluded with a conclusion.

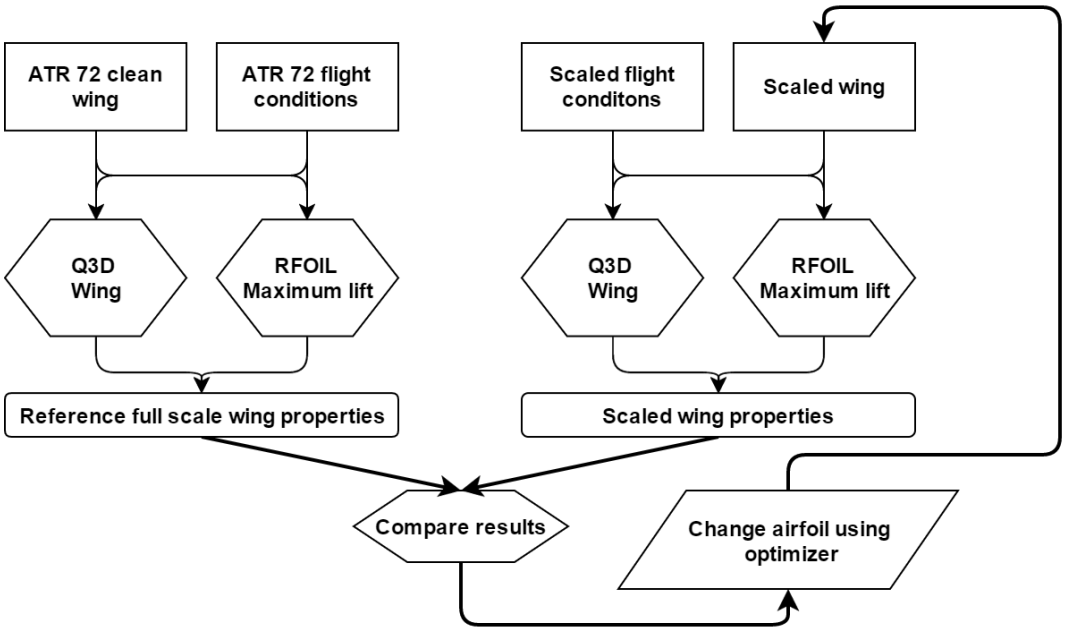


Figure 5.1: Optimization work flow

## 5.1. OBJECTIVE FUNCTION

The optimization is performed with the goal of minimizing the objective function. This means the objective function must represent the difference between full and scaled wing. What it is to be represented has been discussed in Chapter 2, below is discussed how this is determined for the objective calculation in the optimization. The following properties have been deemed important to match for aerodynamic scaling :

- $C_{L_\alpha}$
- $C_M$
- $c_{l,max}$
- Stall behaviour
- $C_D$

These properties are based on the requirements required for similitude in Section 2.4, noteworthy is the inclusion of the drag coefficient. The drag coefficient was added as this term has a high correlation with the wake thickness. It may be the case that this term is later omitted, as it might prove difficult to achieve significant improvements in drag, while also getting better results for the other parameters. The methods of the wing analysis are limited to moderate angles of attack, where the flow is still fully attached and behaves linearly. However, for the stall behaviour and maximum lift different methods are used. The objective is calculated by calculating the properties of the wing using Q3D at two angles of attack default is chosen as -2 and 5 degrees. Thus the derivatives of the lift and moment coefficients are also linear and are included in the optimization when the properties are calculated at two angles of attack.

### 5.1.1. STALL BEHAVIOUR

The stall behaviour is simplified by just checking for which kind of stall is to occur, based on the thickness of the nose of airfoil. The following different kinds of stall are distinguished: leading edge, trailing edge, thin airfoil, and mixed stall. Gault [29] determined that the kind of stall behaviour an airfoil exhibits is determined to a large extent by the thickness of the nose of the airfoil. The thickness is determined by looking at the thickness at 0.0125c. Then, depending on the Reynolds number, the stall behaviour can be categorised. Based on Figure 2.4 it can broadly be said that the thickness at this point must be above 2.3% chord to have trailing edge stall. If the thickness is below this value, the airfoil is discarded and given a very high error value.

### 5.1.2. MAXIMUM LIFT

An aircraft never flies at its maximum lift, there are safety regulations in place that mandate that preventive measures must be activated before the stall (speed) is reached [54]. Of interest is, in this case, the rotate or minimum unstick speed. For a take-off weight of $20000kg$ the *Flight Crew Operating Manual* [30] states a stall speed of $100kts$ and a rotate speed of $110kts$. The lift coefficient at the rotate speed is thus $C_{L,rotate} = \frac{1}{\sqrt{1.1}} C_{L,stall} = 0.95 C_{L,stall}$. The reference value of the full scale case is thus 95% of maximum lift coefficient, which is found using the maximum lift method.

### 5.1.3. ERROR CALCULATION

The final error required to do the optimization is a single value, so all the individual errors are squared and summed. Each error can be given an individual weight factor, before the summation. The errors are calculated as follows: the overall error is calculated as in Equation (5.1), the lift, moment and drag error are calculated as in Equations (5.2) to (5.4) respectively.

$$error = (error_{C_L}^2 + error_{C_M}^2 + error_{C_D}^2) \tag{5.1}$$

$$error_{C_L} = \frac{C_{L_{scale}} - C_{L_{Full}}}{C_{L_{Full}}} \tag{5.2}$$

$$error_{C_M} = \frac{C_{M_{scale}} - C_{M_{Full}}}{C_{M_{Full}}} \tag{5.3}$$

$$error_{C_D} = \frac{C_{D_{scale}} - C_{D_{Full}}}{C_{D_{Full}}} \tag{5.4}$$

## 5.2. PARAMETRIZATION OF THE INPUT

The cross-sectional shape of the airfoil is taken as input for the optimization. Bounds are set on the shape in order to prevent very thin or very thick airfoils, which are not deemed to be realistic. In order to do this optimization it is not convenient to use coordinates as input, as this requires many design variables. In order to achieve a correct parametrisation of the airfoil, in a minimum amount of variables the Class/Shape Transformation is chosen.

The input for the optimization is a parametric representation of the airfoil. The airfoil is represented by the use of Class/Shape Transformation (CST)-coefficients[55]. CST-coefficients are Brezier curves with an added flass function term and are able to model a wide range of smooth curves. The advantage of using CST-coefficients to describe a geometry, is that relatively few variables are required to produce the shape, which makes them convenient for optimization. The definition is given in Equation (5.5), two curves are needed for an airfoil, one for the upper and one for the lower part. Here $\zeta = \frac{z}{c}$ and $\Psi = \frac{x}{c}$, they are both the normalized coordinates and $\zeta_{TE}$ is the trailing edge thickness. The class function is given by $C(\psi) = \psi^{N1}(1-\psi)^{N2}$ and the shape function is $S(\psi)$. Using $N1 = 0.5$ and $N2 = 1.0$ gives good results for NACA-type, round nose and pointed tail airfoils. [56].

$$\zeta(\psi) = C_{N2}^{N1}(\psi)S(\psi) + \psi \cdot \zeta_{TE} \tag{5.5}$$

No constraints are used in this optimization, only bounds on the CST-coefficients. Infeasible design, which are unable to give a solution to the aerodynamic analysis, are given a large objective value. This also means no manufacturing limitations are taken into account.

## 5.3. THE OPTIMIZER

The optimization is done in two steps. First the solution space between the upper and lower bound is searched by the use of a genetic algorithm. The minimum point found by this first optimization is then fed into s sequential quadratic programming (SQP) algorithm. This second steps makes sure the local minimum is found. For both steps the build-in algorithm in MATLAB is used [57, 58].

### 5.3.1. GENETIC ALGORITHM

A genetic algorithm is a an optimization method to search a design space in a way which resembles biological evolution. A genetic algorithm works as follows, it starts with a random population of points, within the design space. The size of the population depends on the number of design variables or user input. At all these points the objective function is evaluated. Then a new population is made based on these values. Some points get passed straight on in the new population, these are called *elites*, other points which have a good fit are used as *parents*. These parents are used to generate new points, called *children*. The children can be generated in two ways from the parents. By combining the vector entries of a pair of parents, called *crossover*, or by making random changes to a single parent called *mutation*. This process is called a *generation*. The genetic algorithm is used when one of the stopping criteria is met, these limits could be a number of generations, a set time limit or a tolerance on the decrease of the function value.[57]

For this optimization the benefit lies in the fact that the genetic algorithm does not start from a starting point, but looks at the design space as a whole. This means the optimizer does not get 'stuck' in a local minimum around the starting point, but is better able to look for a more global minimum. Of course, it is not guaranteed that a global minimum is found.

The downsides are that it is computationally intensive and it does not guarantee a (local) minimum is found. Because of the random nature of the a genetic algorithm and the fact that no gradient data is used, it will require many generations before a minimum is (fully) reached. This is why it is beneficial to couple it to another optimizer. One which does use gradient data and thus can verify that a local minimum is reached.

### 5.3.2. SQP ALGORITHM

A sequential quadratic programming algorihm (SQP) is a efficient method to solve general, continuous, optimization problems. A SQP algorithm splits the problem up into a quadratic programming subproblem at each iteration. This quadratic programming subproblem can

It is especially beneficial for problems which have (many) constraints, however, due to its robustness it is also very well suited for the nonlinear problem in this research. Since the algorithm cannot distinguish between local and global minima, the starting point is very important for the overall result of the optimization.

This is why it is used in combination with the genetic algorithm, to provide a solution, with limited amount of calculations needed.

### 5.3.3. FINITE DIFFERENCE SETTINGS

MATLAB uses finite difference to find the gradient of the aerodynamic coefficients with respect to the CST-coefficients, as there is no analytical solution known. To determine the finite difference settings, used in the calculation of the gradient, a short investigation into the sensitivity of the used programs with respect to the stepsize is done. This is done by altering the input with steps ranging from $10^{-8}$ to $10^{-2}$ and checking if the output, in this case the derivative, is constant. If the resultant change in lift or drag coefficient is not the same for the different stepsizes it can be said that the stepsize produces numerical errors or is too small to accurately give a good gradient result. In this case, Q3D is tested using a small change to the input CST-coefficients and inspecting the results on the derivative with respect to the angle of attack. A forward finite difference scheme is used, the general notation of a forward finite difference scheme can be found in Equation (5.6) [59]. The results of this test are in Figure 5.2. Note, that the left y-axis is for the lift coefficient derivative and the right axis is for the drag coefficient derivative.

Here it can be seen that the solution converges to a constant value at stepsizes of around $10^{-3}$. Using values below this stepsize could yield unreliable results, thus the minimum stepsize is set to $10^{-3}$.

$$\frac{df}{dx} = \frac{f(x+step) - f(x)}{step} \tag{5.6}$$

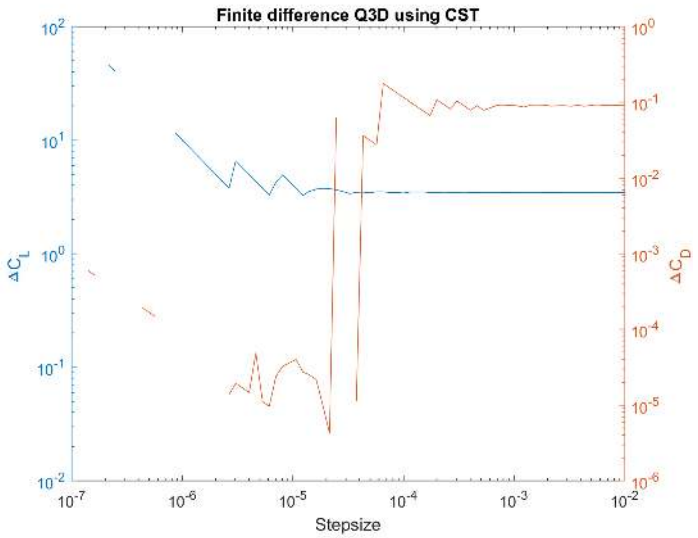


Figure 5.2: The effect of stepsize on Q3D

## 5.4. CONCLUSION

A framework is now in place to optimize the scaled wing, to better represent the full scale wing. The input of the optimization is the shape of the airfoil, which is parametrized using the Class/Shape Transformation (CST). The objective is the sum of the difference between the full scale and small scale values for the lift, moment and drag coefficient at two different angles of attack. The optimization will be performed using a combination of a genetic algorithm, in order to fully capture the the whole design space, and a SQP-algorithm in order to ensure a (local) minimum.

There will always be the question of the results of the optimization will lead to an actual better performance, or that the optimizer finds minima which exist due to the limits of the analytical models. The results of the optimization must be analysed in this light and have to be validated by higher fidelity analyses or wind-tunnel tests.

# 6

# WING ANALYSIS RESULTS

The following chapter will present the results of the analysis, using the methods described in Chapter 3. First the results the analysis if the wing without flaps are given, in Section 6.1. After that the results of the analysis of the wing with flap are presented and explained in Section 6.2.

## 6.1. ANALYSIS OF CLEAN WING

In this section the results of the analysis of the clean wing are presented. The main topics that are going to be investigated are the $C_L$, $C_M$ and $C_D$ for the entire wing and the $C_l$ for the mean aerodynamic chord as a measure of the maximum lift.

### 6.1.1. ANALYSIS OF THE WING

Figure 6.1a shows the $C_L - \alpha$ curve, the full scale wing shows a higher lift coefficient for all angles of attack and here it is visible that the curves have an offset as well as a different slope. The differences in lift coefficient are between 60% and 22% at the same angle of attack. Figure 6.1b has the moment coefficient curve, here it seems to be mainly an offset of the curve, with the maximum difference between 30% and 12%, the full scale has a more negative moment coefficient.

The large differences are visible for the drag, as expected. The differences here, for a fixed lift coefficient, are between 73% and 32%. The full wing has a lower drag coefficient than the scaled wing. Another large difference is visible for the lift curve of the airfoil, the maximum lift are far off, it is 1.86 for the full scale wing and 1.26 for the scaled wing, that is a difference of 33%. Both the airfoils seem to exhibit trailing-edge stall, as indicated by the gradual curve near the maximum lift coefficient [6].

In order to investigate the effect of the change in Mach number, the calculation on the scaled wing is performed at two different Mach numbers, with the other variables kept the same. The angle of attack is set at 3 degrees, for the scaled case at the standard Mach number of 0.067 this gives $C_L = 0.502$. At a Mach number of 0.17 the lift coefficient becomes 0.518, this is an increase of 3%. The full scale case gives a lift coefficient of 0.781, this is an increase of 56%. Of this 3% can be attributed to the Mach number effect, which means that the Reynolds number effect causes a decrease 53% in lift coefficient.

Important for the downwash is how the lift is distributed across the span. Figures 6.2a and 6.2b show the spanwise lift for fixed angle of attack and lift coefficient, respectively. Again, it is clear that the differences are small, when looking at a fixed lift coefficient. Figure 6.2d shows that the differences are small, but increase towards the tip, but still remain within a limit of around 3.5%. The differences in Figures 6.2c and 6.2d are defined as in Equation (6.1). Figure 6.2c shows that the errors for different angles of attack are much larger, as was seen in Figure 6.1a and the differences decrease with angle of attack and also decrease towards the tip. The large error shown in Figure 6.2d for $C_L = 0.05$ starting at 0.6 spanwise position is likely due to the difference in spanwise loading. A small shift in the absolute value of spanwise loading lift coefficient will yield a large difference. Because the local lift coefficients at such a low overall wing lift coefficient are low, thus already a small (absolute) difference will yield large relative differences.

$$Difference = \frac{c_{l,full} - c_{l,scaled}}{c_{l,full}} \tag{6.1}$$

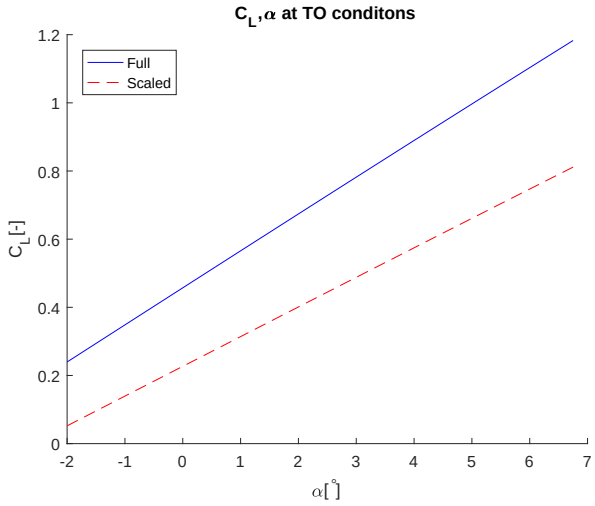


(a) Lift for the wing

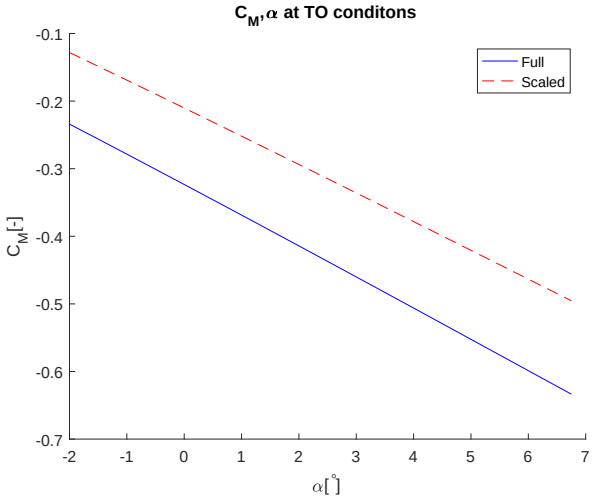


(b) Moment for the wing

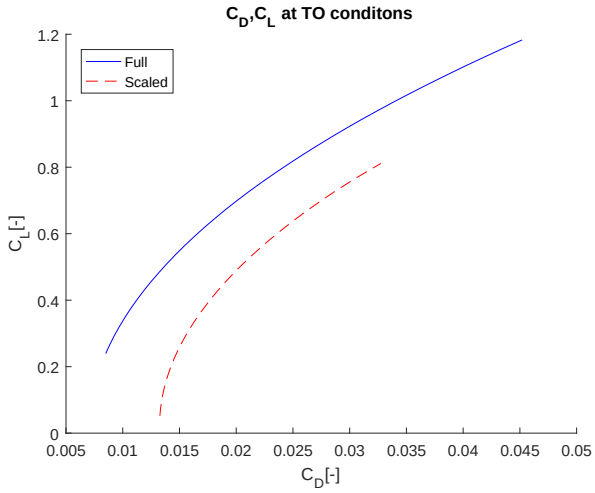


(c) Drag for the wing

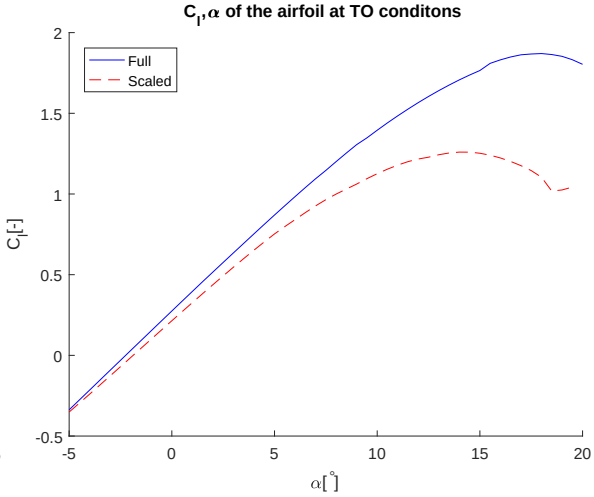


(d) The curve of the MAC airfoil

Figure 6.1: The results of the clean wing analysis, the main aerodynamic properties

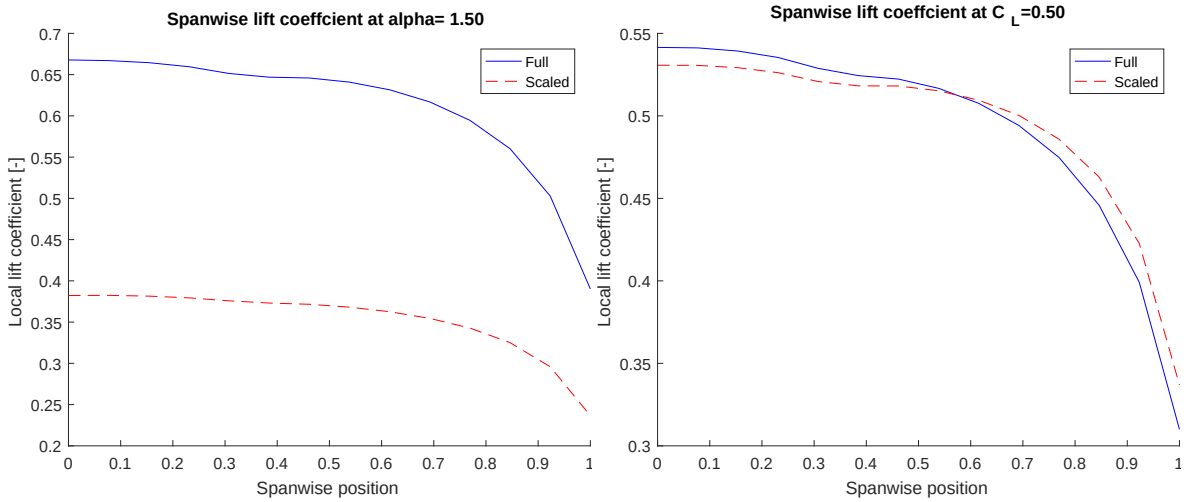


(a) Local spanwise lift coefficient, for fixed angle of attack




(b) Local spanwise lift coefficient, for fixed lift

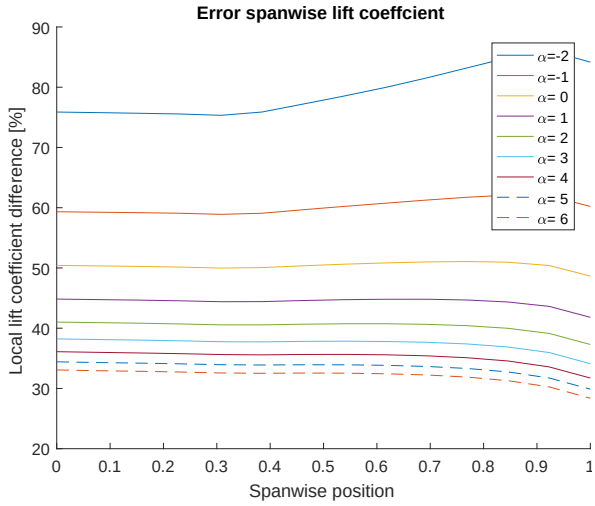


(c) Difference between the full and scaled wing at spanwise positions

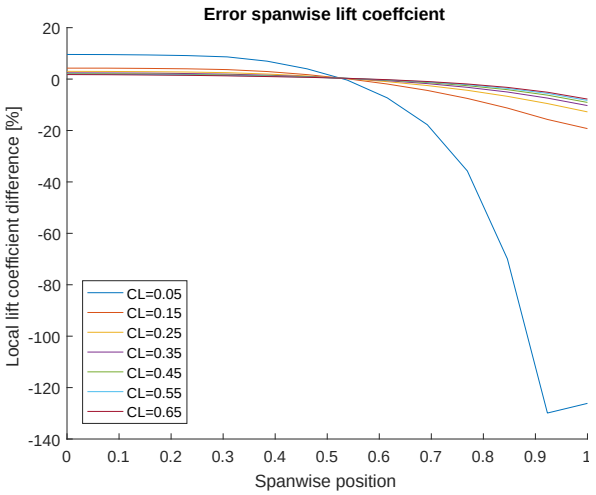


(d) Difference between the full and scaled wing at spanwise positions

Figure 6.2: The results of the clean wing analysis, further results

### 6.1.2. PRESSURE AND BOUNDARY LAYER ANALYSIS

Next it is interesting to look at some properties of the boundary layer, to see where the differences stem from. Figure 6.3a show the pressure distribution over the MAC airfoil, both the scaled and full scale are for the same lift coefficient. Only minor differences are visible here, with a possible laminar separation bubble around 0.1 chord, and the peak pressure is almost the same. A laminar separation bubble is earmarked by a slow reduction in pressure, or even a constant pressure.

More pronounced differences are visible in Figure 6.3b, shown here is the displacement thickness of the boundary layer for the top and lower side of the airfoil, for the scaled and full scale case. The displacement thickness is displayed as fraction of chord. On the top side first of all it is visible that the scaled displacement is (relatively) thicker, as was expected. At around 0.1 chord there is a small 'bump' shown on the graph, which is likely a laminar separation bubble, as supported by the evidence found in Figure 6.3a. On the lower side a larger discrepancy is visible. Again, the displacement thickness is larger for the scaled version, but more interestingly a large increase is seen from $0.5x/c$, this corresponds with the change in geometry of the airfoil as visible in Figure 2.6a. Likely another laminar bubble occurs here. In order to investigate if a separation bubble occurs, the friction coefficient is investigated ($c_f$). When a (laminar) separation bubble occurs there is back flow in this region and the skin friction is thus zero or negative. In Figure 6.3d the result is shown of the skin friction analysis. For the scaled top side it is visible that the $c_f$ becomes negative at an x-coordinate of about 0.1. This location was found earlier to be of interest, as well. Thus it is safe to say an laminar separation bubble occurs here. Then looking at the lower side another bubble occurs around 0.55 to 0.7 x-coordinate, for the scaled case and the full scale case also shows a small dip here. Again, this location corresponds to earlier evidence found for a laminar separation bubble.

Finally, the momentum thickness ($\theta$) is shown in Figure 6.3c, this gives a better indication for the wake properties. On the topside the trend is similar as for the displacement thickness. On the lower side, however, the situation is different. The full and scaled case are similar up to around 0.65 chord, after which the shape of the scaled case starts to diverge and becomes significantly thicker.

#### EFFECT OF FORCED TRANSITION

Since all the laminar separation bubbles that were determined are a result of the laminar boundary layer, it is interesting to look at the effect of forcing the transition. In this case it is chosen to fix the transition from laminar to turbulent flow at 5% of the chord, for both the scaled and full scale airfoil. Figure 6.4 shows that the results for the scaled and full airfoil much more similar and the (laminar) separation bubbles no longer occur. The main difference for the pressure distribution is a slightly wider peak and less lift at the rear of the airfoil. The shape of the displacement thickness is also very similar, however, the boundary layer is thicker for the scaled case.

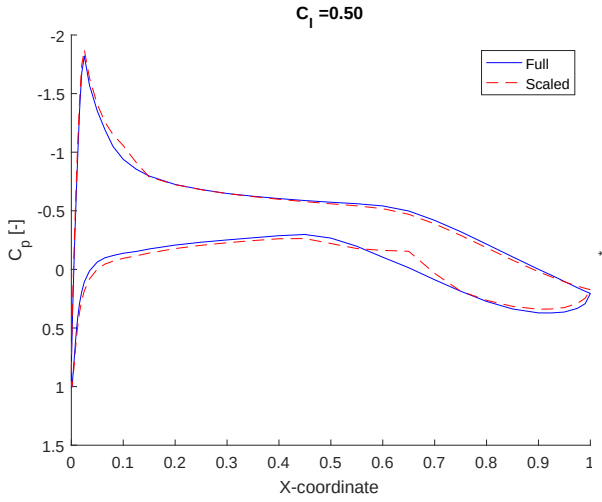


(a) Pressure distribution at the MAC

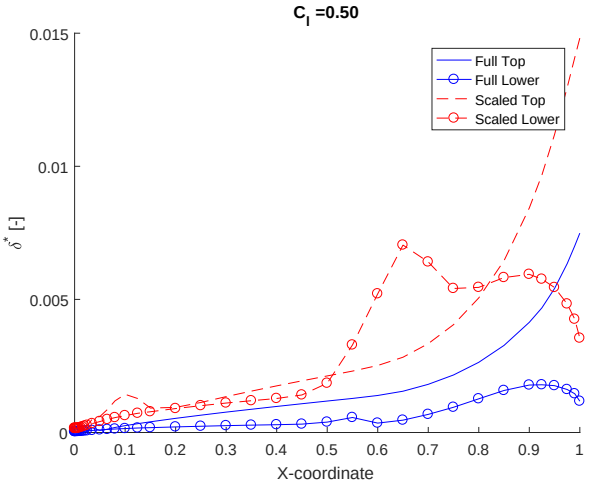


(b) Displacement thickness at the MAC

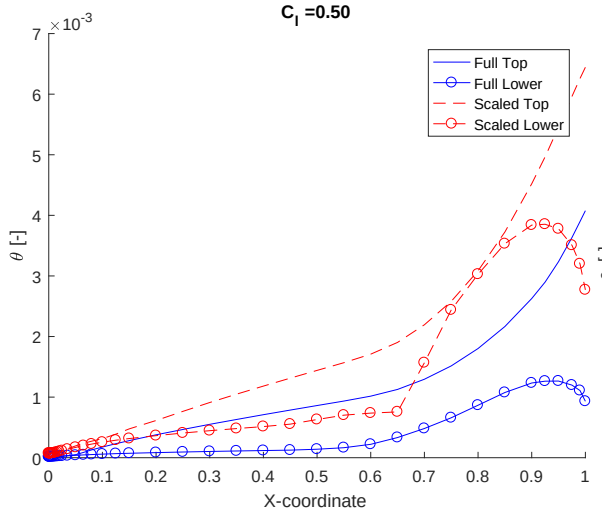


(c) Momentum thickness at the MAC

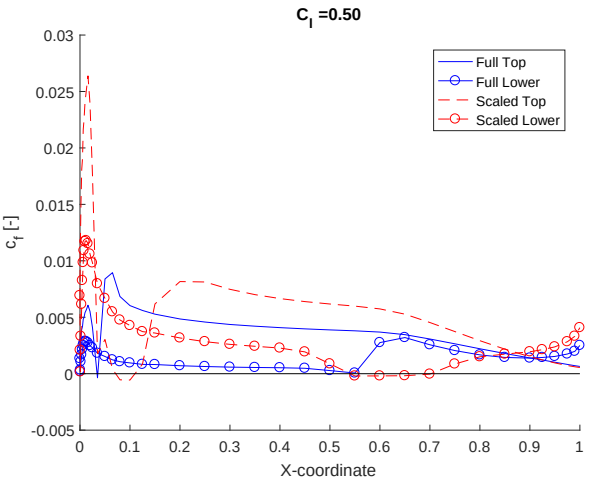


(d) Friction coefficient at the MAC

Figure 6.3: The results of the clean airfoil boundary layer analysis

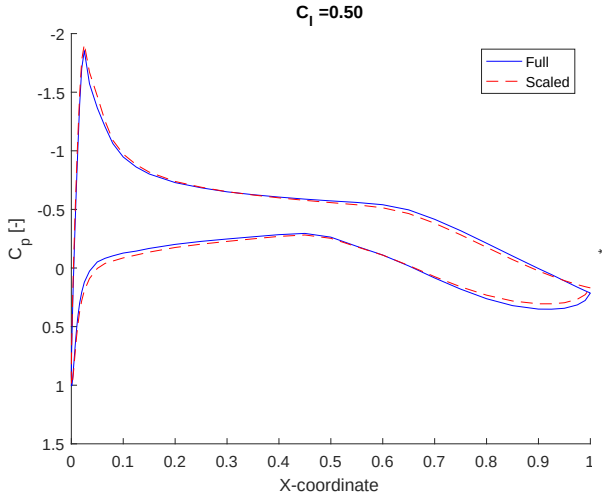


(a) Pressure distribution at the MAC

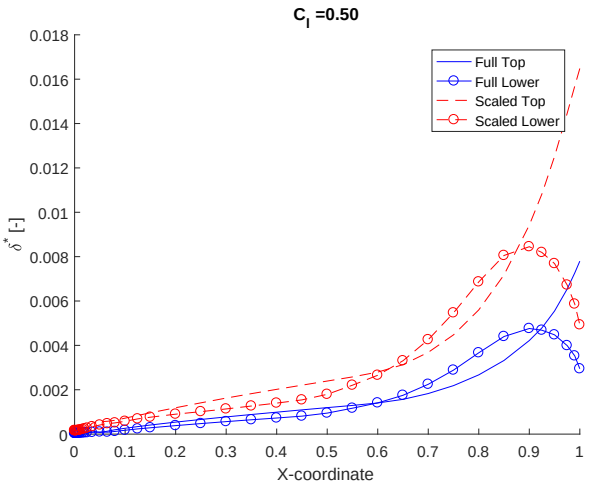


(b) Displacement thickness at the MAC

Figure 6.4: Boundary layer results with forced transition, on the clean airfoil

### 6.1.3. ANALYSIS OF LONGITUDINAL STATIC STABILITY

In this section briefly the static stability is visited, as introduced in Section 2.5. Investigated here is the effect of scaling on the lift curve-slope, $\frac{C_{L\alpha_h}}{C_{L\alpha}}$, from Equation (2.11). In order to do this the lift curve slope of the wing and the horizontal tail is investigated. The lift curve-slope of the main wing shows a decrease of 15% and the horizontal tail of 16% when going from full to scaled. This means an increase of 6.3% in the $\frac{C_{L\alpha_h}}{C_{L\alpha}}$-term.

This cause of this is the non-linear behaviour of aerodynamic properties with scaling, the aerodynamic properties do not scale linearly with the Reynolds number. The Reynolds number for the main wing is higher than that of the horizontal tail, due to its longer chord length.

Further details on the effect of the downwash gradient and velocity deficit are given in Section 7.1.3.

## 6.2. ANALYSIS OF WING WITH FLAP

The following section will have the results of the analysis of the wing with flap, only the wing is modelled, with a 60% slotted fowler flap at 15 deg. First the entire wing as modelled in AVL will be discussed, after that the airfoil and boundary layer will be investigated.

### 6.2.1. WING ANALYSIS

Figure 6.5 has the results for the analysis of the full wing with flaps. Figure 6.5a shows the lift curve and Figure 6.5b shows the moment curve. Similar to the wing without flaps the lift curve of the scaled wing shows both an offset and a decrease in lift curve slope. For the moment curve there is a much clearer difference in slope, however, the offset is smaller than for the clean wing case. The underlying reason is likely a different pressure distribution across the airfoil, this will be investigated in Section 6.2.2. The difference between the lift coefficients for the full and scaled wing, for fixed angle of attack, are between 37% and 18%.

A further investigation on the effect of the Mach number is done for the an angle of attack of 3 degrees. For the standard scaled case this results in a lift coefficient of 1.25. However, when increasing the Mach number to 0.17 and keeping all the other variables the same, the lift coefficient is 1.30, or an increase of 4%. The full scale lift coefficient at this angle of attack is 1.60, or an increase of 28% over the original scaled value. This means that the Reynolds number effect causes a difference of 24%, 6 times more than the Mach number effect.

The sectional, spanwise properties are investigated in Figures 6.5c and 6.5d. These show the local lift coefficient and angle of attack, respectively, at a freestream angle of attack of 5 deg. In Figure 6.5c it is visible that the scaled wing has an overall lower lift coefficient and that the part where the flap is located shows an clear increase in lift. However, the relative lift on the outer part of the wing is, relatively, higher for the scaled case. This can also be seen in Figure 6.5d where the difference of local angles of attack between the inner and outer wing are much higher for the scaled wing. This can also be seen when inspecting the local lift curve slopes, as used by AVL. For the full wing, this is $1.1 * 2\pi$ for the flapped part and $1.08 * 2\pi$ for the clean part. The scaled wing has a slope of $0.97 * 2\pi$ for the wing with flap and $0.99 * 2\pi$ for the clean wing. This is however, not the root cause of the difference, but rather an indication of where the difference stems from. This will, also, be further investigated in the Section 6.2.2. For further investigation the lift curve slope for a fixed lift coefficient of 1.33 is given in Figure 6.6, here a clear difference in spanwise loading is visible. The scaled wing has less inboard lift loading, compared to the full scale case.

The employed method does not include a different decrease in flap angle for different Reynolds numbers, such as described in Section 3.3.2. The (relatively) thicker boundary layer of the scaled wing will result in a lower effective flap angle and thus a further reduction of lift. This effect is, however, taken into account when calculating the lift curve slope of the airfoil, as required by AVL, since this is done using MSES with viscous effects included.

### 6.2.2. AIRFOIL ANALYSIS

The lay-out of the airfoil is as in Figure 2.6b and the analysis is on the MAC airfoil, using MSES. The graphs shown in Figure 6.7 are for the 14.7% scale, as discussed in the use-case (Section 2.6).

A similar trend as for the clean wing is visible here, with the scaled case giving a lower lift for the same angle of attack and a lower lift curve slope. Again the moment curve of the scaled airfoil is above the full size case. Compared to the clean wing, the differences are larger between 7.0 and 8.5% for the $c_l$ and 6.5% and 8.5% for the $c_m$. The drag, Figure 6.7c shows an even larger gap, with differences between 76% and 130%.

Just like for the clean wing, MSES allows for an investigation of the pressure distribution and boundary layer data. Two different situations are shown in Figure 6.8, one for angle of attack of both full and scaled is 5 deg

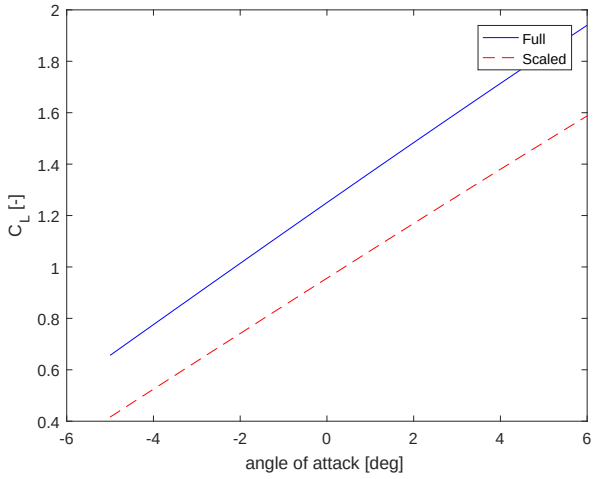


(a) Lift curve for the wing with flap

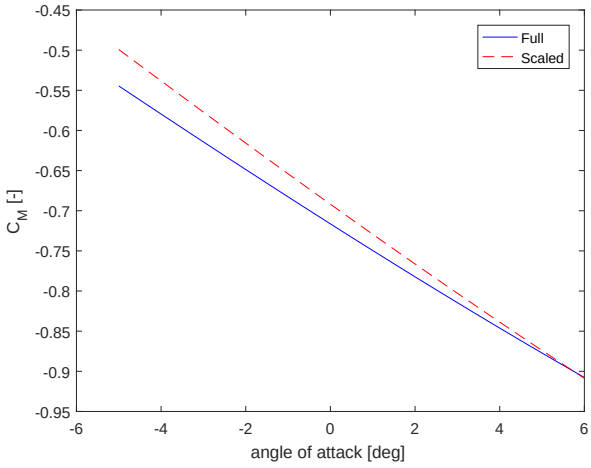


(b) Moment curve for the wing with flap

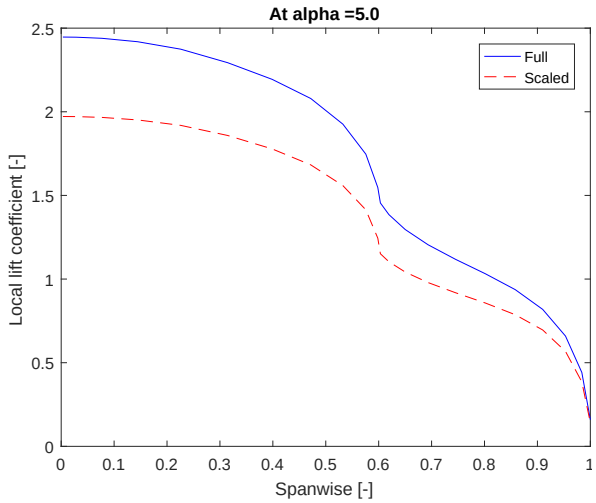


(c) Spanwise distribution of the lift

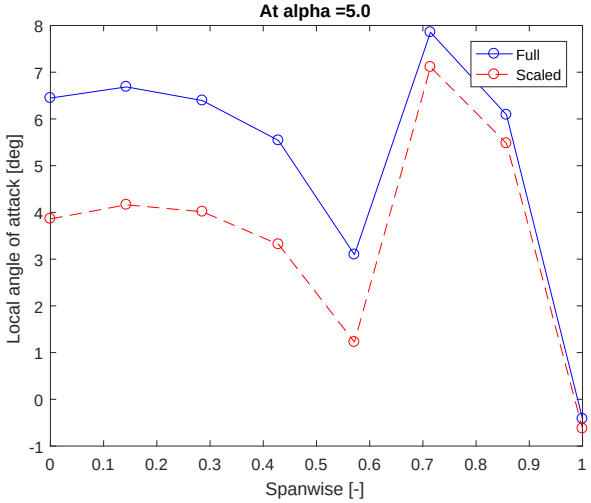


(d) Local effective angle of attack at different spanwise sections

Figure 6.5: The results of the flapped wing analysis at take-off conditions

and one for $c_l = 2.2$, which corresponds to an angle of attack of 4.9 deg for the scaled and 3.0 deg for the full scale airfoil. These analyses were done with the transition left free, to be determined by MSES.

Figure 6.8a shows a larger peak pressure on the full wing and a slightly higher pressure coefficient overall, which is to be expected, since it corresponds to a $c_l$ of approximately 2.4. For the scaled case there is a laminar separation bubble visible in Figures 6.8a and 6.8b at around $0.1x/c$, which is consistent to the data found in Section 6.1. For the same lift coefficient, Figure 6.8b, the largest difference can be seen on the flap, where the full scale case generates more lift here. This also explains the difference found for the moment coefficient, as the full scale case has more aft-loading, leading to a larger negative moment (coefficient).

When looking at the displacement thickness, the scaled case shows a thicker boundary layer, as expected. The bottom of the main wing, or the first element, shows some peculiarities at around $0.8x/c$. When inspecting the pressure distribution a bump can be seen starting at 0.7 chord, which corresponds to the start of the large peak in the displacement thickness. A possible explanation is that a (laminar) separation bubble exists here. Again, the skin friction coefficient is investigated, in Figure 6.8d. On the first element the same bubbles exist as on the clean wing, as expected, at 0.1 and 0.55 to 0.7 x-coordinate. But now for the scaled second element another bubble can be seen for the top side around x-coordinate of 1.1.

The large curve down starting on the bottom at 0.85 x/c in Figure 6.8c, which was also seen to a lesser extent in Figure 6.3c, is likely due to the concave shape of the airfoil around this region.

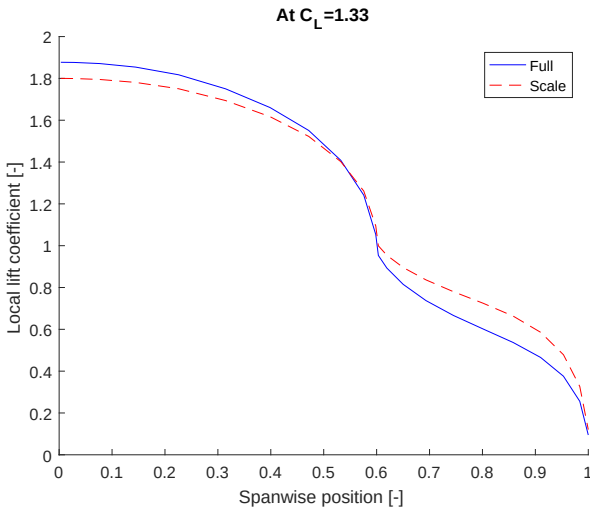


Figure 6.6: Spanwise lift loading of the full and scale wing at fixed lift coefficient

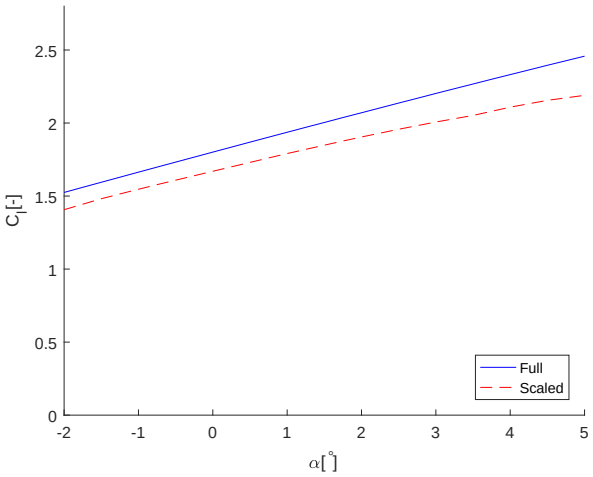


(a) Lift coefficient at the MAC

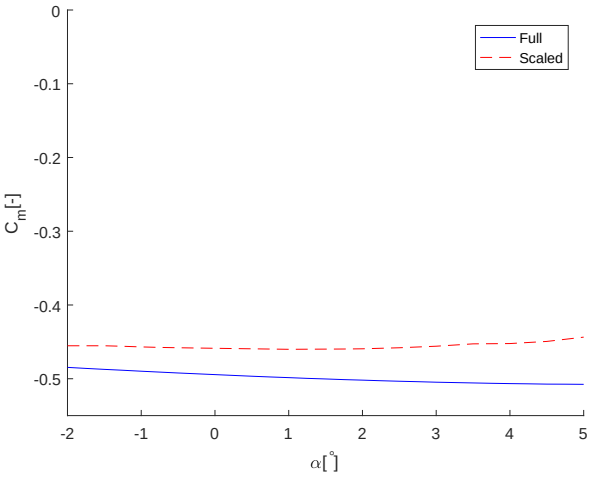


(b) Moment coefficient at the MAC

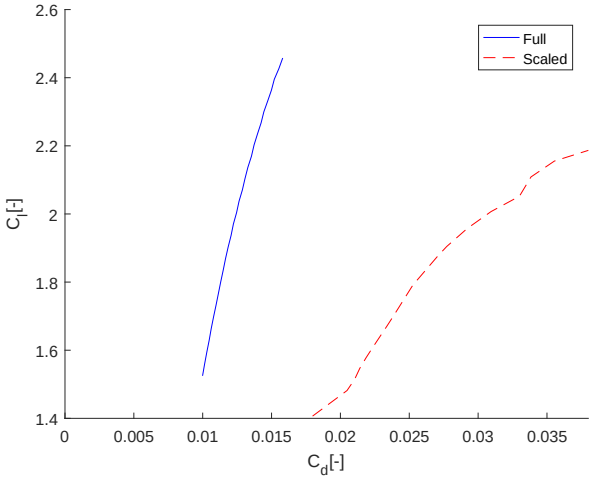


(c) Drag coefficient at the MAC

Figure 6.7: Analysis of the airfoil with 15 deg flap

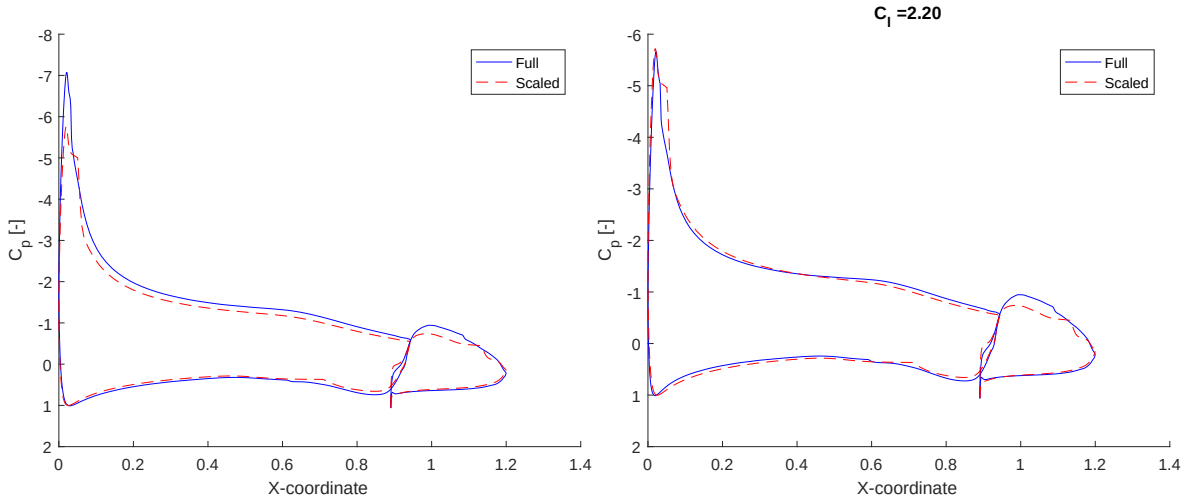


(a) Pressure distribution at the MAC at $\alpha = 5$




(b) Pressure distribution at the MAC

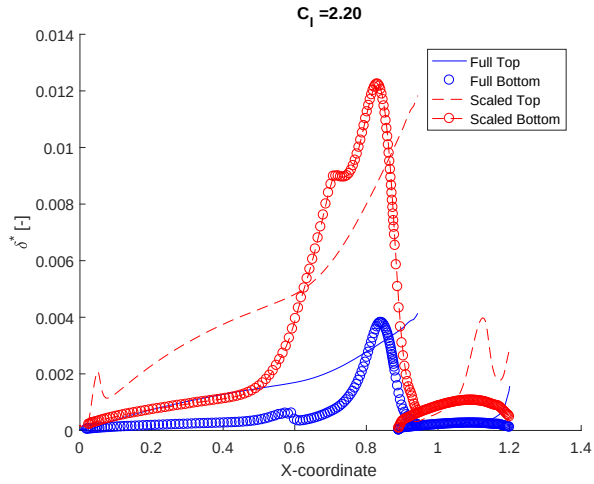


(c) Displacement thickness at the MAC

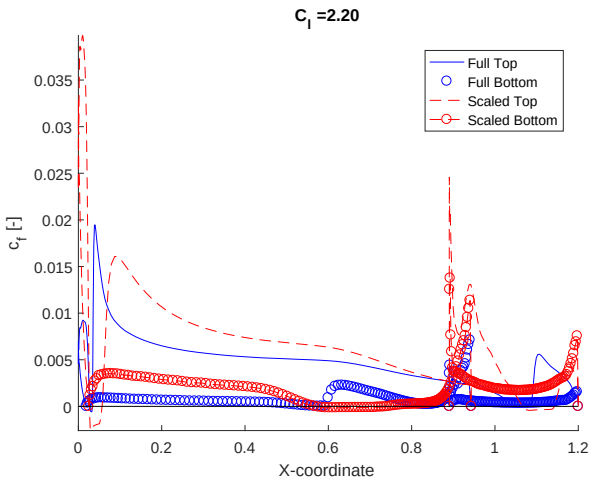


(d) Friction coefficient at the MAC

Figure 6.8: Boundary layer properties of the airfoil with 15 deg flap

### 6.2.3. MAXIMUM LIFT

As another measure of similarity it is relevant to look at the maximum lift coefficient of the wing. Using the pressure difference rule the maximum lift coefficient for different configurations can be calculated. However, since the critical pressure difference is not known for Reynolds number below 1 million and the behaviour seems to be asymptotic, it is not possible to investigate the maximum lift at the scale of 14.7%. To get an idea of what the effect of scaling is on the maximum lift coefficient, it is possible to evaluate other, larger, scale factors and at several different flap settings, these results are shown in Figure 6.9. As is normal, an increase in flap angle leads to an increase in maximum lift, although at low scale factors the increase is very small. The 14.7% scale model will likely give an even lower maximum lift coefficient than the 25% case displayed here. The 25% scaled case shows a reduction in maximum lift coefficient for a flap setting of 15 degrees of approximately 29%. Two areas immediately stand out, the large dip in maximum lift coefficient at around a scale factor of 0.75 and another dip can be seen for the scale factor of 1 and flap 10. Looking at the rest of the curve and what the expectation of the results are, these two dips are likely wrong data. The source of these errors can be found in numerical difficulties in MSES. MSES is not able to generate a converged solution at these specific Reynolds number (of around 6 million) and thus uses only a partially converged solution, which gives the wrong values.

As expected the maximum lift increases with increasing scale factor, for each flap angle. However, all the different flap settings converge to a maximum lift coefficient after a scale factor of about 0.7, whereas it was expected that the maximum lift would increase with increasing Reynolds number.

Two possibilities are considered here, either the method does not fully capture the actual situation and the maximum lift should be increasing, or the maximum lift does, in fact, reach a plateau. When investigating the method it can be seen in Figure 3.14a that for Reynolds number above 2 million and low Mach numbers the maximum pressure difference does not increase by a lot. So the PDR will likely predict similar maximum lift coefficients, as the rest of the method is based on inviscid calculations. It can thus be very well that the PDR does not predict the maximum lift coefficient for these Reynolds numbers correctly. In research it was found that that the maximum lift coefficient does reach a plateau, but this was for higher Reynolds numbers -10 million opposed to the 3.5 million here- than the ones that are in Figure 6.9 [49].

It can still be concluded that there is a large difference in maximum lift coefficient between the scaled and full scale case. The difference is of such magnitude that giving the scaled wing a larger flap deflection is not enough to bridge the gap between the two. Thus representing the small scale case, especially the 14.7% scale model, in terms of maximum lift will be impossible.

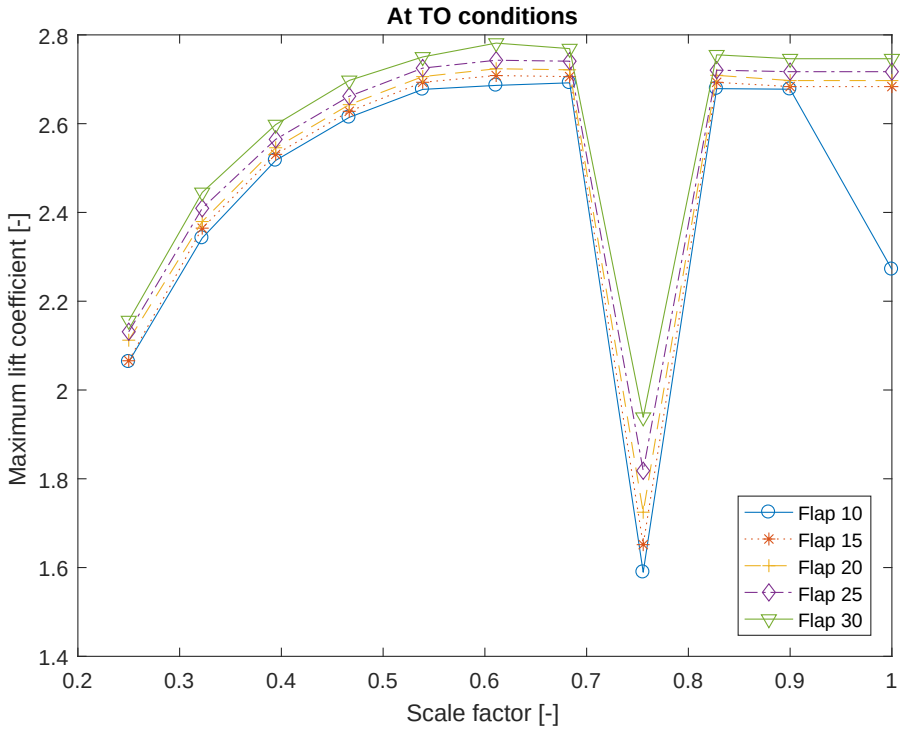


Figure 6.9: Effect of scale on maximum lift

## 6.3. CONCLUSION

Overall a decrease in similarity can be seen when moving from a clean wing to a wing with (trailing edge) flap. Large differences are found for both the wing with and without flap. The lift curves show both a change in slope and an offset, between the full and the scaled case. The moment curve for the clean wing exhibits mainly an offset on the moment curve, whereas the moment curve of the wing with flap shows a change in slope. The scaled wing with flap shows (much) less loading on the part with flap, than the full scale wing, this results in a lower lift coefficient for the same angle of attack. The degradation in aerodynamic coefficients was mainly due to the Reynolds number effect, the effects of the Mach number were within a few percent.

When investigating the 2D properties it was found that the scaled wing showed signs of laminar separation bubbles, which are part of the explanation behind the deterioration of the aerodynamic properties. As expected, the boundary layer for the scaled aircraft was relatively (much) thick for both with and without flaps.

The maximum lift for both cases was also much different, for the clean wing a difference of 33% is found, for the wing with flap this is also above 25%.

Figure 6.9 highlighted the difficulties faced when working with MSES, where convergence issues lead to incorrect results. This means that all the results of the wing with flap must be analysed with caution. The results of scaled flight testing model could be under- or overestimated by MSES. The trends found for the wing with flap are clear, scaling decreases the aerodynamic similarity between the full and scaled aircraft. Just by how much the aerodynamic properties will differ is not something which can be said with complete certainty and thus the results found in this chapter must be seen as being indicative of the type of problems occurring with scaling.

# 7

# WING WAKE RESULTS

In this chapter the results of the wake analysis, for both the full scale and scaled wing are shown. The scaled case is the 14.7% geometric scaled wing, as described in Section 2.6.3. The flight conditions are the take-off conditions. First the clean wing will be discussed, in Section 7.1, followed by the wing with flap, in Section 7.2. After that the influence of the scaling on the longitudinal stability is discussed. Finally, the chapter is ended with an investigation into different scale factors on the wake width, velocity deficit and downwash in Section 7.3. The current chapter contains results for an angle of attack of 5 degrees, in Appendix B results for an angle of attack of zero degrees can be found.

## 7.1. CLEAN WING

The wake at the wake survey plane of the clean wing will be described in this section. In the figures only the half span of the wake survey plane is investigated, as it is assumed that the aircraft is symmetrical with respect to the x,z-plane.

### 7.1.1. FULL SCALE

Figure 7.1 has the results for the full scale clean wing wake analysis. It shows the wake at the wake survey plane, along with a projection of the fuselage and wing. It shows the wake as a contour plot, with the velocity loss ($\frac{V_{loc}}{V_\infty}$). Figure 7.1a shows the results using the ESDU method for determining the wake, Figure 7.1b shows the results for Schlichting method. Both methods are explained in Chapter 4. Figure 7.2 shows the velocity profile, at the same longitudinal location, but looking at the x,z-plane, at a lateral position of 0.13 times the span. At the position where the fuselage ends.

First of all, it is visible that the results of the ESDU and Schlichting method are as good as the same, with the maximum difference being 1%, in Figure 7.2. The core of the wake is the in zero-lift plane, which is at $0.62m$, or 0.27 times the MAC, below the wing, for a zero-lift angle ($\alpha_0$) of $-2.74$ deg. The wake width is $0.60m$, or 0.26 MAC, and the maximum velocity deficit is approximately 4% The velocity profile in Figure 7.2 shows the same data, from a different perspective. There is almost no change in the velocity profile, when looking at it spanwise, since the chord does not change within the investigated region. The drag coefficient is also the same within the investigated region.

### 7.1.2. SCALED WING

In the previous section it was noted that ESDU and Schlichting method for wake calculation give almost the same answers, so only the results from the ESDU method are given in Figure 7.3. Figure 7.3b shows that they are, again, almost the same. All the dimensions for the scaled wing survey plane are scaled with the 14.7% scaling factor. A projection of the fuselage and wing of the aircraft is also given in Figure 7.3a.

The zero-lift angle is $-2.74$ deg, thus the wake core is at the same, albeit scaled, location as the full size case. Due to the higher drag coefficient of the scaled wing, the wake is (relatively) thicker and has a higher velocity loss associated. The wake thickness is $0.12m$ or $0.35MAC$. The maximum velocity deficit is 0.053.

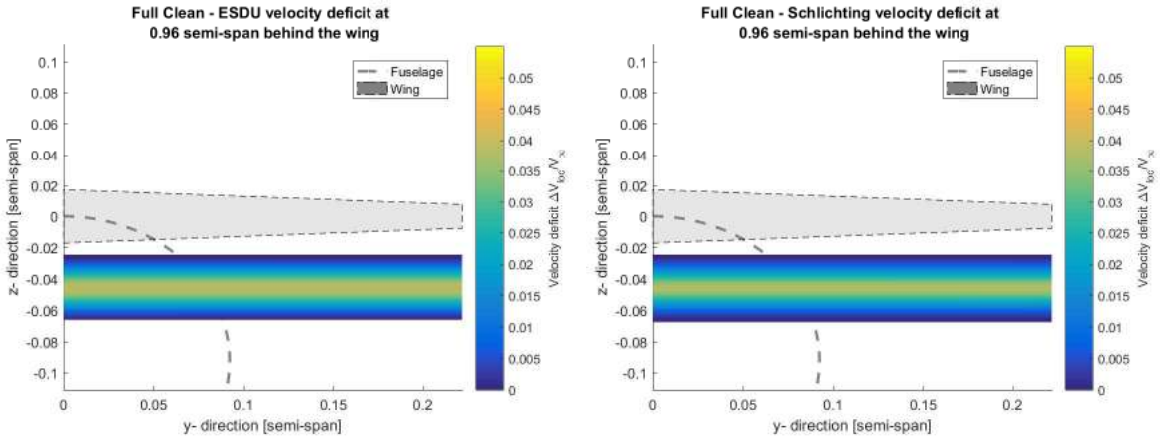


(a) Wake profile of the clean wing, ESDU wake model

(b) Wake profile of the clean wing, Schlichting wake model

Figure 7.1: Wake profile using the two different methods on the full wing

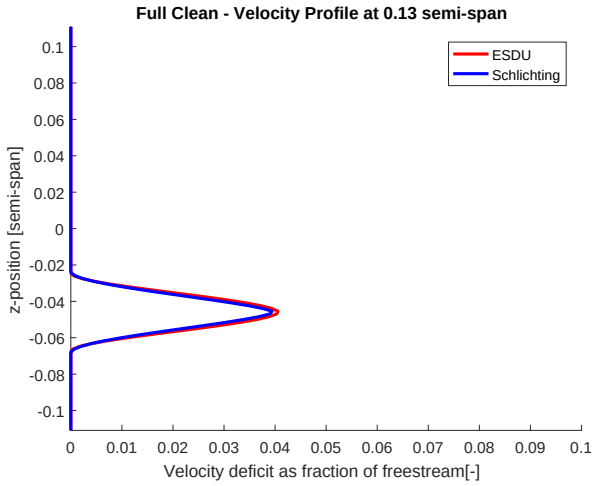


Figure 7.2: Velocity profile of the clean wing, at the wake survey plane

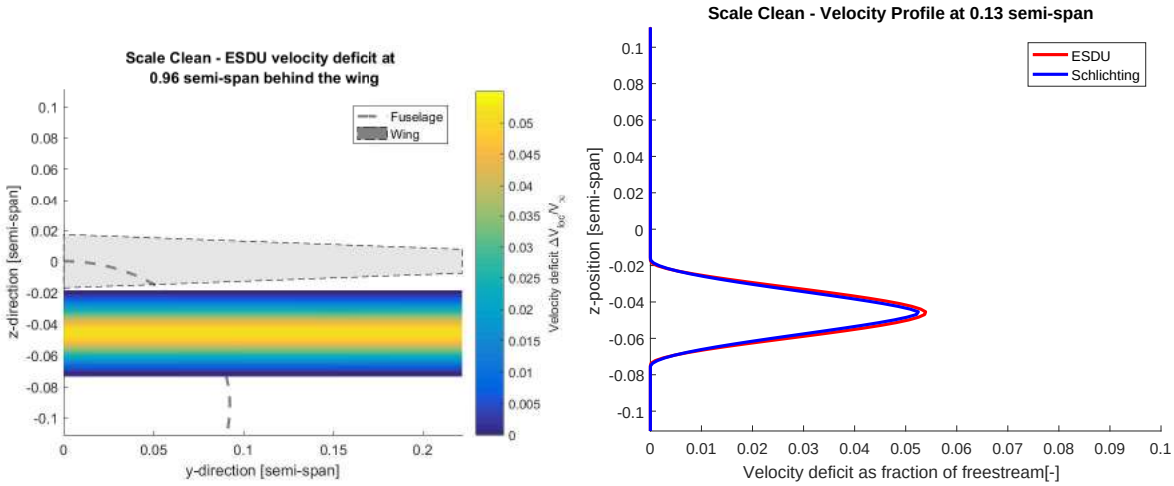


(a) Wake profile of the clean wing, ESDU wake model

(b) Velocity profile of the clean wing

Figure 7.3: Results of the wake calculations for the scaled wing

### 7.1.3. INFLUENCE OF WAKE ON LONGITUDINAL STATIC STABILITY

In this section the influence of scaling has on the longitudinal static stability, due to the wake. This section is a continuation of Section 6.1.3 and Section 2.5. The terms highlighted, from Equation (2.11) here are the downwash gradient, $\frac{d\varepsilon}{d\alpha}$ and the velocity ratio $\frac{V_h}{V}$.

The velocity ratio will change when a tail configuration is selected with the tail located inside the wake, with the scaled wing showing a relative larger velocity deficit and a wider wake.

Unfortunately the model used in this research is limited in that the downwash gradient is not dependant on the Reynolds number and only on (nondimensionalized) position relative to the wing.

### 7.1.4. CONCLUSION

Table 7.1 contains the data for both the scaled and full scale wing. As can be seen in both the table and the figures, the wake for the scaled wing is thicker, relatively, and leads to a greater velocity deficit. Which is what was expected, as the drag coefficient of the scaled wing is higher.

In lieu of a good reference source of an exact wake profile, a comparison can be made with values for the velocity fraction between the free stream and at the horizontal tail ($(V_h/V)^2$), from aircraft design textbooks. It is suggested that a value for the dynamic pressure between 0.85−0.95 be used, with 0.90 as a typical value [60]. This translate to a velocity deficit between 0.03 − 0.08; the values found here for velocity deficit correspond to this range, thus giving more confidence to the validity.

Table 7.1: Results of the clean wing wake

| | Wake width [%MAC] | Maximum velocity deficit [-] | Effective downwash at the tail [deg] |
|---|---|---|---|
| Clean - Full | 26 | 0.040 | 0.321 |
| Clean - Scale | 35 | 0.053 | 0.321 |
| Difference [%] | 35 | 32 | 0 |

## 7.2. WING WITH FLAP

The wing with flap is also investigated. The flap is a 60% span, single slotted Fowler flap at 15 deg, as described in the use-case. Within the wake survey plane-span the wing chord and flap do not change, only the thickness is changed, slightly. Again only the half span is investigated due to symmetry. Here the plot is extended in the negative z-direction, in order to fully display the wake. The bottom of the wake survey plane is indicated with the red-dotted line. Note: the flap is not shown in the projection of the wing.

### 7.2.1. FULL

Compared to the clean wing case, the wake of the wing with flap is more in negative z-direction, thicker and has a higher velocity deficit. As can be seen in Figure 7.4a the wake is nearly completely outside the wake survey plane for an angle of attack of 5 degrees. The location of the vortex core is at $1.79m$, or $0.78MAC$, below the wing, the width is around $0.82m$, or $0.36MAC$, and the velocity loss is 5%. This is an increase of 105%, 30% and 25% over the clean full scale wing, respectively. It was of course expected that the addition of flaps would give these results, the flaps generate increased lift, an increase of $C_L$ of 1.09, and add more drag.

### 7.2.2. SCALED

For the scaled case the trends are very similar, again an increase in distance from the wing for the wake location, an increase in wake width and velocity deficit. The wake is also almost completely outside of the wake survey plane. The wake core is located at $0.27m$, or $0.80MAC$, below the wing, the wake width is around $0.15m$, or $0.44MAC$, and the velocity deficit is around 0.063%. This means an increase of 92%, 9.8% and 19%, respectively. The difference between the full and scaled case are, however, smaller for the flapped case than for the clean case. This is due to the smaller difference in drag coefficient, for the clean wing the full scale average sectional drag coefficient is 0.084 and for scaled 0.0150. For the flapped case it is an average of 0.0153 for the full scale case and 0.0200 for the scaled case. The difference between the clean wing drag coefficients is much greater than that of the flapped wing, thus leading to a larger difference in the wake.

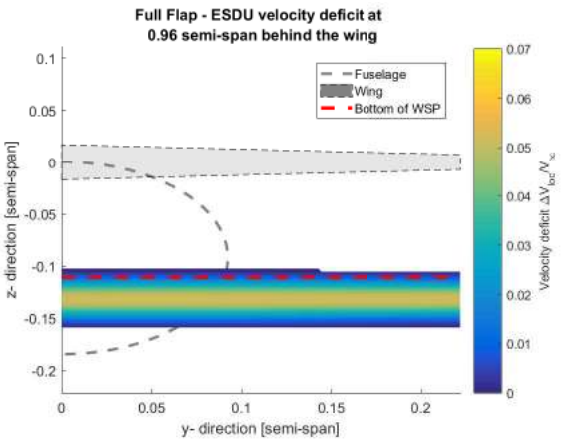


(a) Wake profile of the flapped wing, ESDU wake model

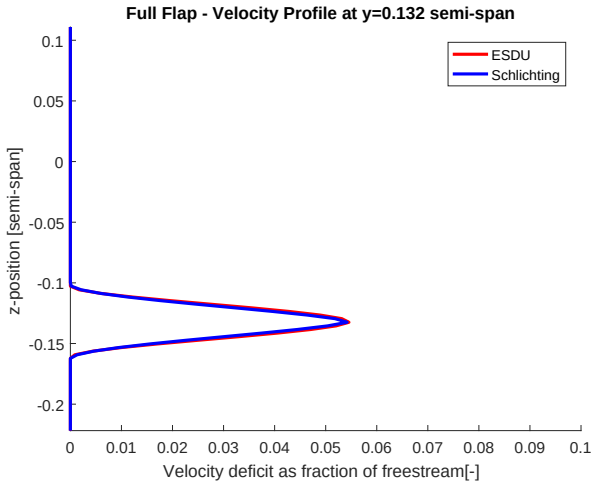


(b) Velocity profile of the flapped wing

Figure 7.4: Results of the wake calculations for the full wing

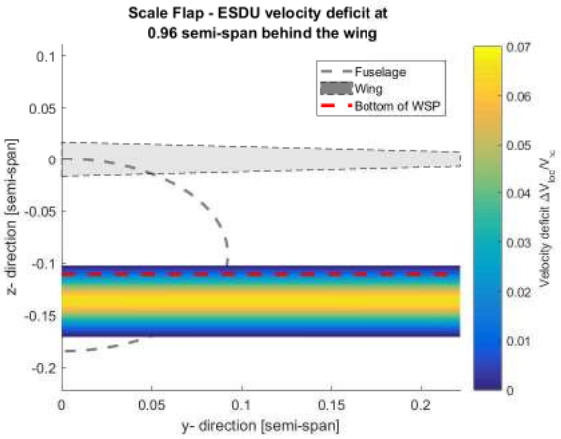


(a) Wake profile of the flapped wing, ESDU wake model

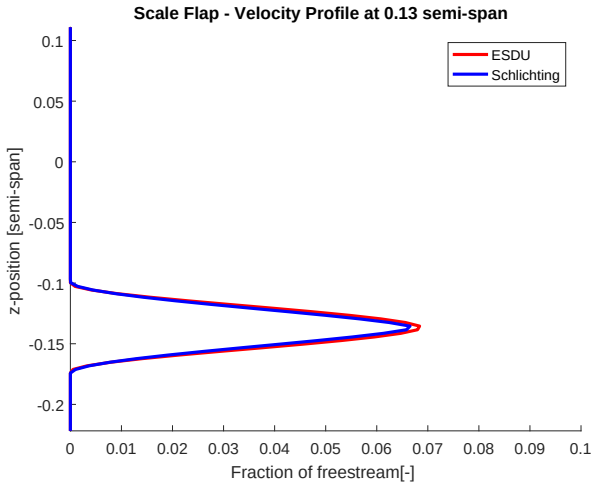


(b) Velocity profile of the flapped wing, at the wake survey plane

Figure 7.5: Results of the wake calculations for the scaled wing

### 7.2.3. CONCLUSION

A comparison of the results can be found in Table 7.2. Again the values found for the velocity deficit correspond that what is expected from general aircraft design rules, as described in Section 7.1.4. The scaled case sees an increase in the wake width of 15%, when scaling it to full size, the wake is located at a slightly different location and the velocity deficit is increased by approximately 19%.

The difference in drag coefficient at the root compared to the tip was greater for the flapped case, but still this results in a wake thickness difference of approximately 1%, still very small. Just like for the clean case, the results of the ESDU and Schlichting model were both in agreement.

Table 7.2: Results for the flapped wing wake

| | Wake width [%MAC] | Maximum velocity deficit [-] | Effective downwash at the tail [deg] |
|---|---|---|---|
| Flap - Full | 36 | 0.053 | 4.8 |
| Flap - Scale | 44 | 0.063 | 3.77 |
| Difference [%] | 22 | 19 | -21 |

## 7.3. EFFECT OF SCALE

Figure 7.6 shows the wake width for both the clean and flapped case. The wing is geometrically, dynamically and Froude scaled, with the velocity set to the take-off conditions for each scale. As expected, the wake width grows with increasing scale factor, as can be seen in Figure 7.6a. However, when looking at the nondimensionalized wake width in Figure 7.6b it shows that the relative wake width is decreasing for the clean wing case. The flapped wing case also shows a decreasing trend, however, the data here is troubled with convergence issues of MSES, especially the values for the drag give irregular results. Which is why the gaps are present in the dataset. Thus for an increasing size of the scale model, the wake grows relatively less. Which is to be expected, as the drag coefficient of a smaller model is higher. It is interesting to note that the wake width and velocity deficit follow a similar trend.

The graph for the flapped case in Figure 7.8 is marked with a dotted line and has markers for each point as the results of this calculation are uncertain, the trend is similar as for the clean wing, however there seem to be two large outliers at a scale factor of approximately 0.3 and 0.75, the rest of the curve is also not smooth as expected. The clean wing does show a smooth curve, as is expected, as the velocity deficit is dependant on the drag coefficient of the wing, and this decreases with increasing scale factor.

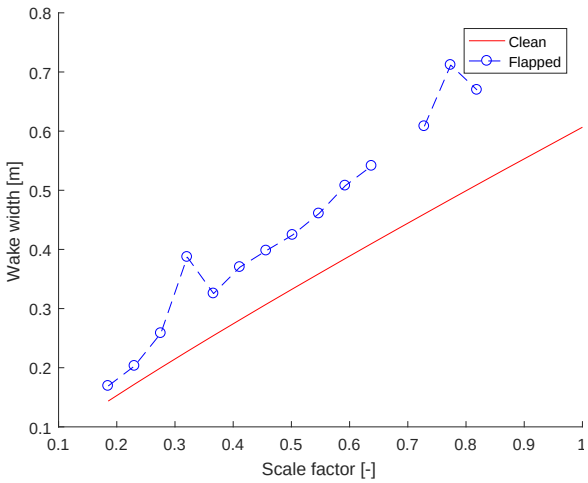


(a) Wake width for different scale factors

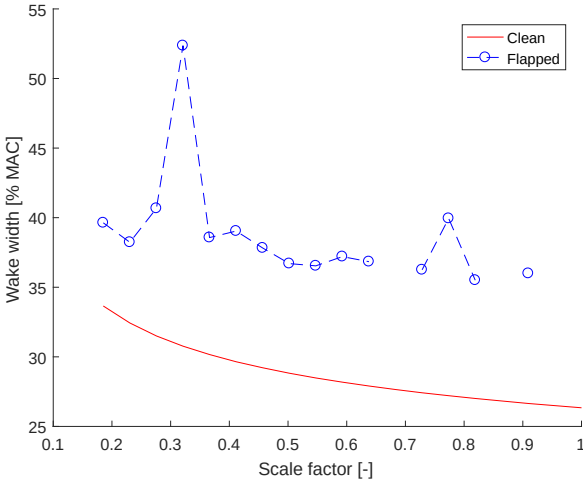


(b) Nondimensionalized wake width

Figure 7.6: Influence of scaling on the wake width

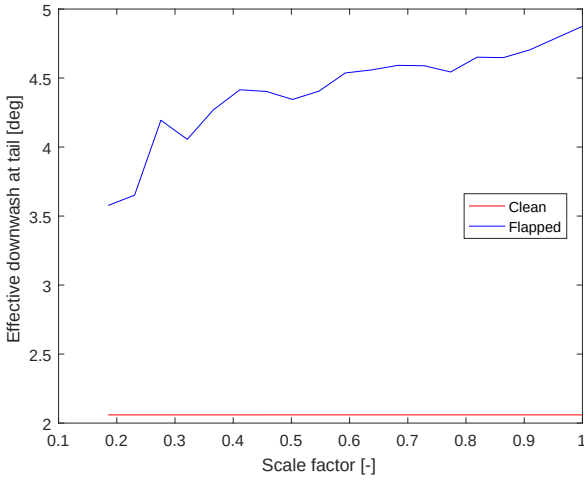


Figure 7.7: Influence of scale on effective downwash at the tail

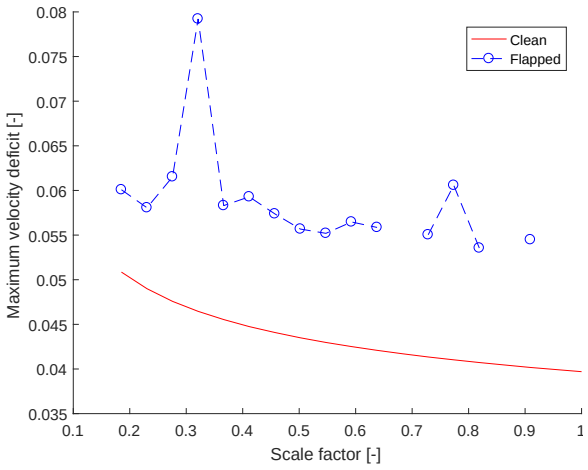


Figure 7.8: Influence of scale on the maximum velocity deficit

The curve for the clean wing in Figure 7.7 shows a clear shortcoming of the wake model used, namely a constant downwash at the tail for increasing scale factor. It is expected that the downwash increases with increasing scale, as the circulation increases with increasing scale factor and the downwash is directly related

to the circulation of the wing [23]. The line for the flapped wing does show this increase of downwash angle with increase in scale.

## 7.4. CONCLUSION

Relatively the wake becomes thicker when scaling the aircraft, this can be seen for both the clean wing and the wing with flap. The velocity loss associated with the scaled wake is also larger than the full scale wake. The differences between the two wakes is larger for the clean wing than for the wing with flap. The basis for this can be found in the drag of the wing, the drag coefficient of the scaled wing is higher, as was seen in the previous chapter. The difference in drag coefficient of the scaled clean wing is relatively higher than the difference in drag coefficient of the flapped wing.

It can then be concluded that the effect of scaling has a clear influence on the wake for both the clean wing and the scaled wing, with the influence of scaling having a greater effect on the clean wing wake than on the flapped wake. This has to be taken into account when tail surface or propulsive unit is placed in the wake of the wing.

The trends when inspecting the effect of different scale factor on some wake parameters are non-linear, with larger relative differences between full and scale shown at smaller scaling factors.

The results for the clean wing were found to be continuous over the spectrum of scaling factors and thus can be seen as giving a reliable indication what will happen to the wake of a scaled wing. The results of the wing with flap did not give a continuous solution over the different scaling factors, like the clean wing. The reason behind this is convergence and computational difficulties with MSES, it is not believed that the actual wake of an aircraft changes in this irregularly. This also means that the results of the wake of the scaled wing must be inspected with caution. Perhaps the results are an overestimation or an underestimation. The general trend can still seen in Figures 7.6 and 7.7, namely that the wake becomes relatively thicker, higher velocity deficit and has a lower downwash angle with decreasing scale factor. The exact extend of these difference cannot safely be concluded from the presented data, but the trend can.

# 8

# OPTIMIZATION RESULTS

As noted in Section 6.1 there are clear discrepancies in the different aerodynamic properties. The following section has the results for the optimization, which has the goal of reducing the aerodynamic differences between the full scale and scaled case. In the previous analysis discrepancies were found for the maximum lift, drag, the lift and moment coefficient. To further enhance the model it will be of interest to see if the improvement in drag and maximum lift do not come at a large reduction in similarity of the lift and moment. As a baseline for comparison first the scaled wing is given, only with an incidence angle, in Section 8.1. After this first an optimization will be performed with drag in included, in Section 8.2, then an optimization is performed without the drag included in the objective, in Section 8.3. In Section 8.4 it is investigated if altering only the thickness of the airfoil will yield better results. Finally, in Section 8.5 the performance of the optimized wings is analysed in another condition than the default take-off condition, namely the cruise condition.

## 8.1. ANALYSIS WITH INCIDENCE ANGLE

To set a baseline, to which the different optimizations can be compared, first the scaled wing is given an incidence angle in order to better match the lift coefficient at an angle of attack of zero. The incidence angle is 2.6 degrees, the results are shown in Figure 8.1. The scaled wing lift coefficient is now between 17% higher and 12% lower than the full wing and the moment coefficient is between 0.2% and 4.5% higher. The drag coefficient is between 80% and 3.3% higher for the same angle of attack and 88% and 37% higher for the same lift coefficient.

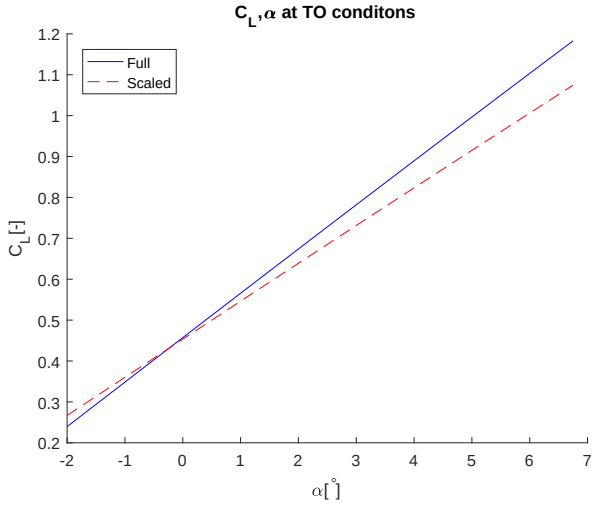


(a) Lift for the wing

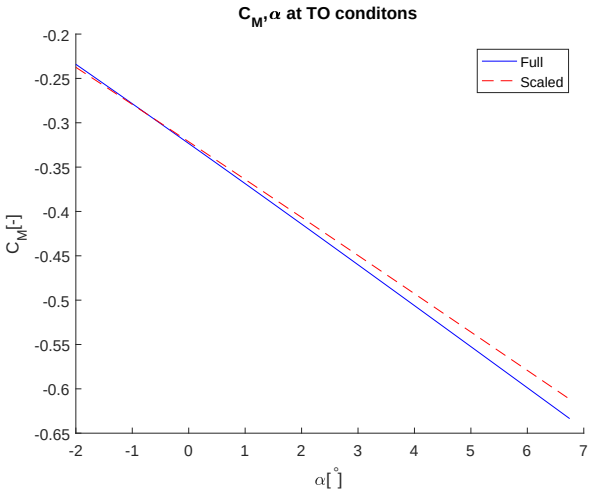


(b) Moment for the wing

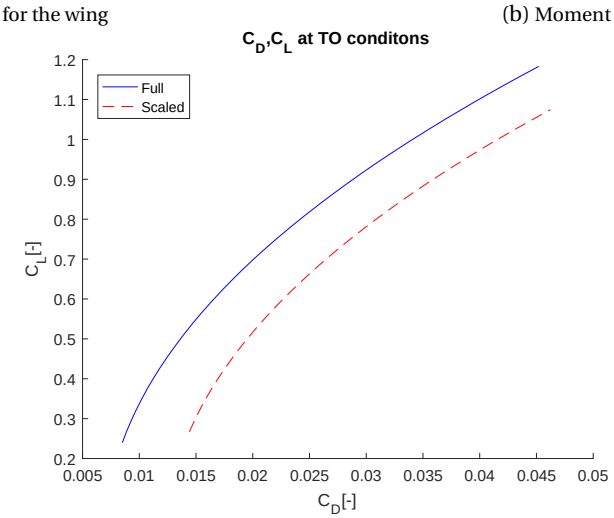


(c) Drag for the wing

Figure 8.1: The results of the optimization with drag

## 8.2. OPTIMIZATION WITH DRAG COEFFICIENT INCLUDED

First an optimization is performed with the drag coefficient included in the objective function. For this optimization the weight factors for lift, moment and maximum lift coefficients are set to 1, the weight factor of the drag is set to 0.5. The weight factor of the drag coefficient in the objective was lowered, since leaving it at 1 proved to give barely any improvement for the lift, moment and maximum lift coefficients. Figure 8.2 shows the optimized airfoils with and without the drag in the objective function. It shows that the nose of the airfoil is similar to that of the original airfoil, however, after 0.1 x/c the airfoil is thinner than the original and remains that way. This is to be expected, as a thinner airfoil leads to less drag. The nose curvature is almost the same, coupled with a thinner profile likely leads to an improvement in maximum lift coefficient.

In this analysis the wing is given an incidence angle of 1.5°, in order to better match the full scale case, at an angle of attack of zero.

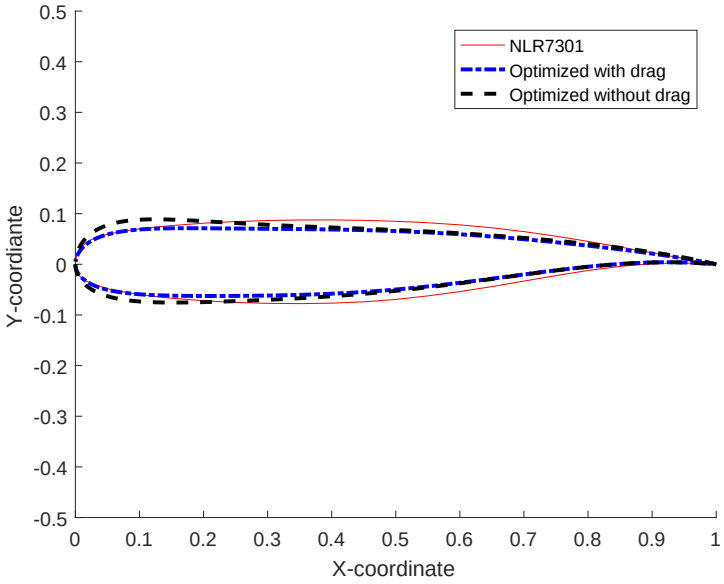


Figure 8.2: Two different optimized airfoils

### 8.2.1. ANALYSIS OF THE OPTIMIZED WING

The results of the optimization with drag can be seen in Figure 8.3. The comparison between the unoptimized (Figure 6.1) and the optimized can be done. The maximum lift is 1.54, which is a difference of 17.5% with the full scale case, which is an improvement of 22% over the non-optimized maximum lift. The lift curve has a difference between 0.37% and 11%. The moment line shows a difference of between 3.8% and 5.5% for a fixed angle of attack. The drag is between 64% more and 1.6% less, for a fixed angle of attack and between 77 and 31% more for a fixed lift coefficient.

More results can be found in Appendix B.2.1, in this appendix graphs for the spanwise lift distribution are given.

### 8.2.2. BOUNDARY LAYER ANALYSIS

Next the pressure distribution and boundary layer can be investigated, see Figure 8.4. The pressure distribution and displacement thickness both indicate a laminar separation bubble at 0.1 x/c on the top and one around 0.7 x/c on the lower side. The difference between the pressure distribution of the full scale and scaled and optimized airfoil is clear, in Figure 8.4a. It shows a very different pressure distribution with a wider pressure peak.

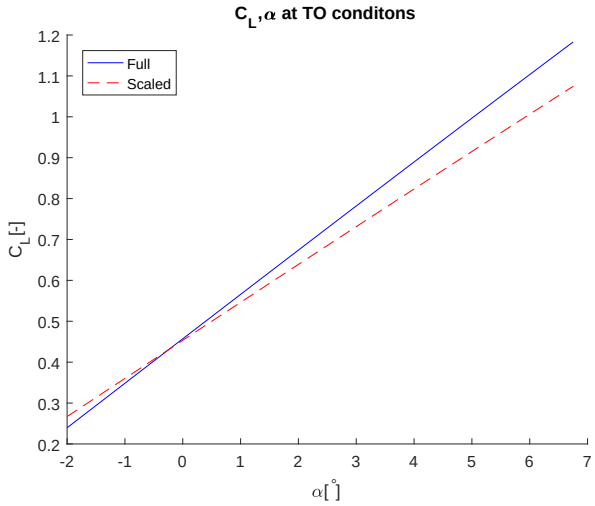


(a) Lift for the wing

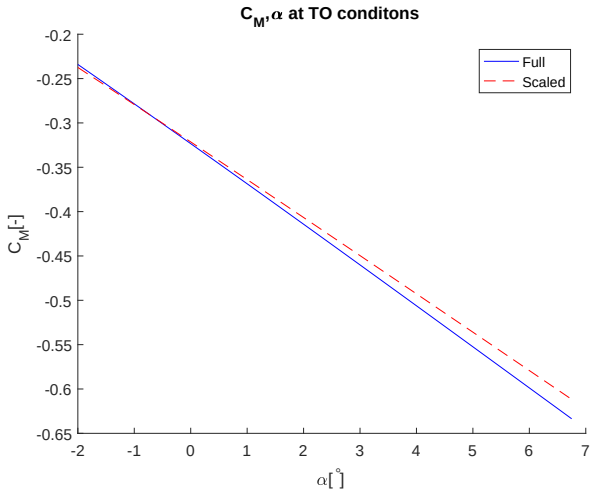


(b) Moment for the wing

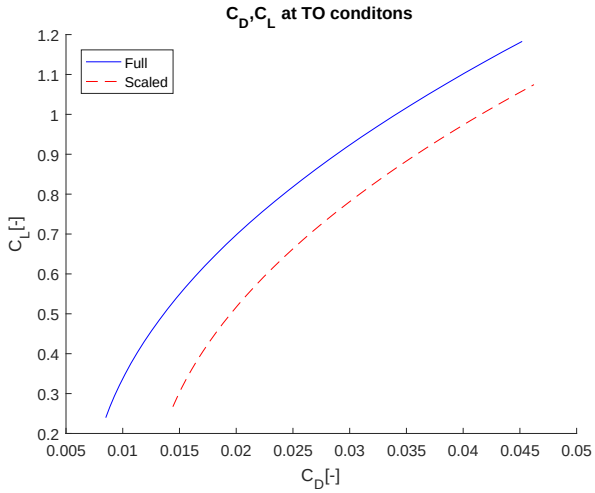


(c) Drag for the wing

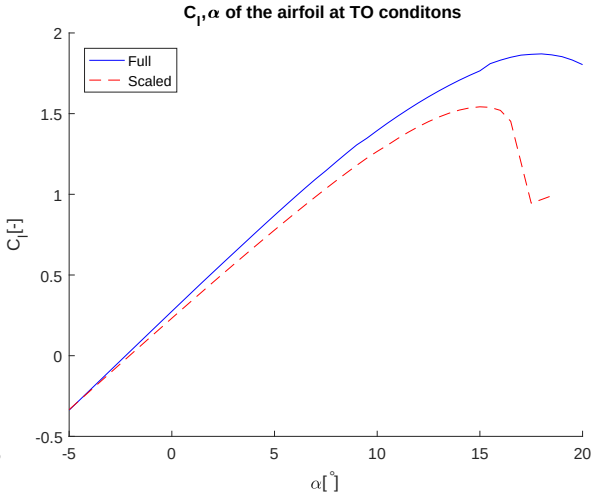


(d) The curve of the MAC airfoil

Figure 8.3: The results of the optimization with drag

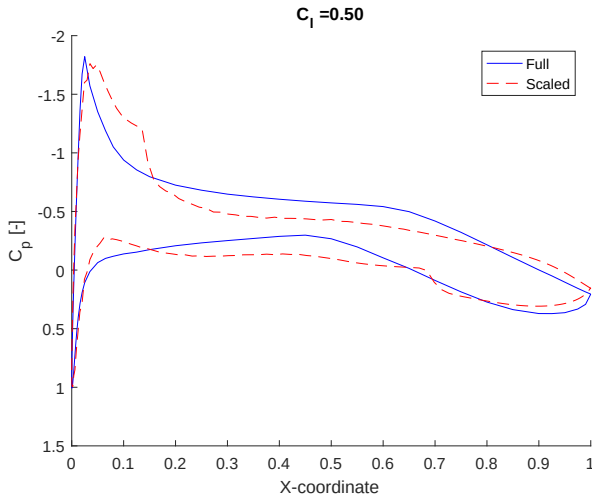


(a) Pressure coefficient

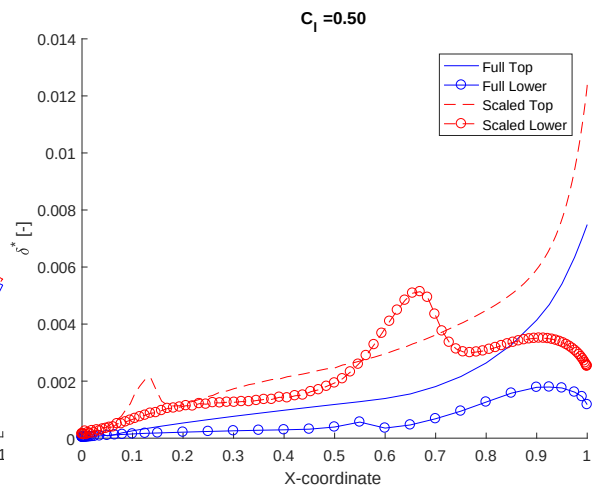


(b) Displacement thickness

Figure 8.4: The results of the optimization with drag

## 8.3. OPTIMIZATION WITHOUT DRAG COEFFICIENT

The method used for the optimization was the same as for the previous section, however now the difference in drag coefficient is not taken into account in the error calculation. The airfoil is also shown in Figure 8.2, it shows a thicker front of the airfoil, however, after 0.2 x/c it becomes thinner than the original airfoil. This larger nose likely leads to an increase in lift coefficient. The results are shown in Figure 8.5. The difference for the lift curve is between 8.1% and -7.1%, the moment curve has a difference between 5.7% and -1.8%. The drag is between 79% and 7.9% higher, for a fixed angle of attack. And between 91% and 36.5% higher for the same lift coefficient. The maximum lift of the scaled airfoil is 1.56, which is 24% more than the non-optimized, but still 16.6% below the full scale case. It does look like the stall behaviour changes, as the curve does not show a nice rounded maximum lift coefficient region as the one found in Figure 8.3d.

In conclusion, excluding the drag coefficient from the optimization does not give a large improvement for the (maximum) lift and moment coefficient.

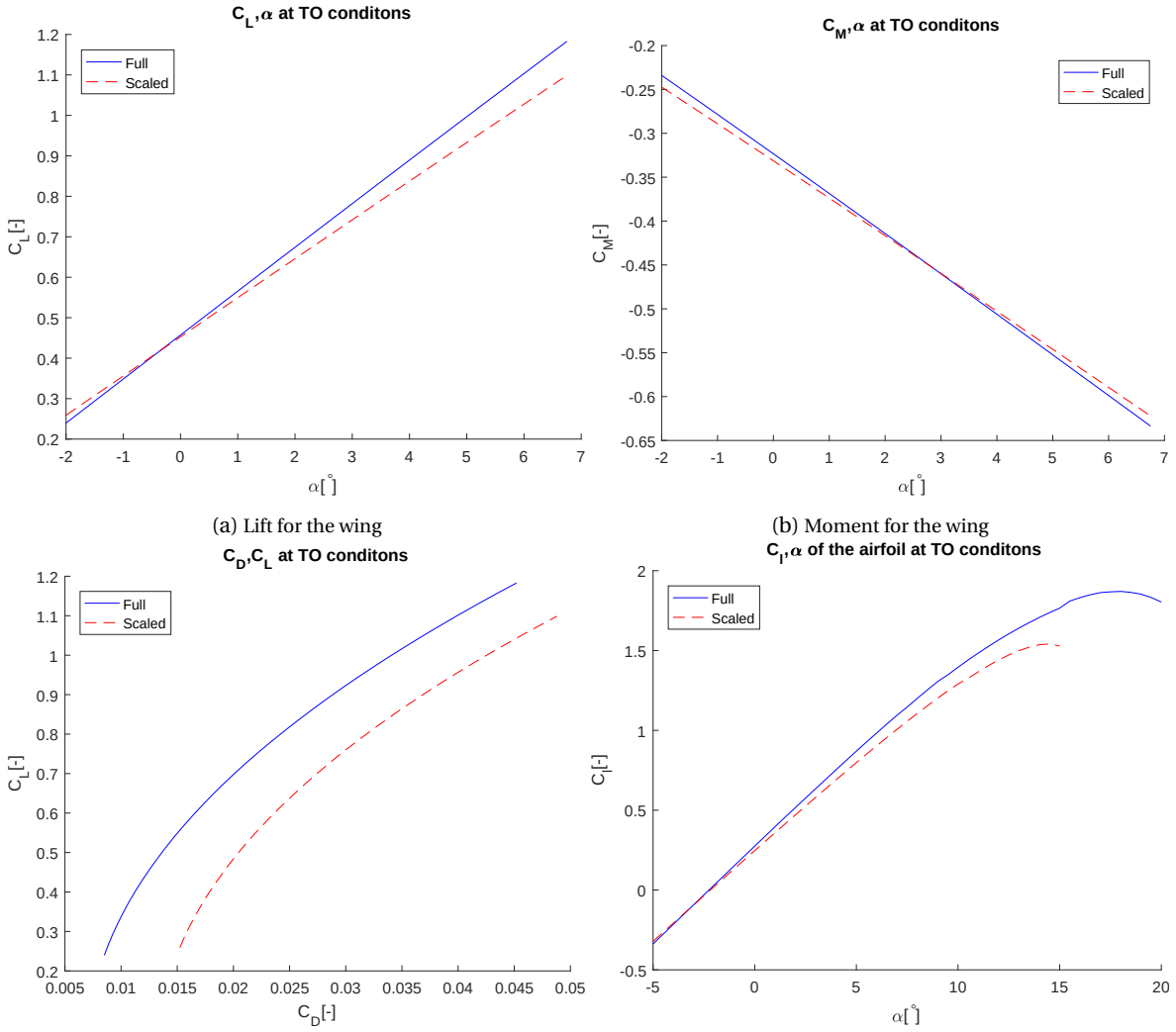


(a) Lift for the wing

(b) Moment for the wing

(c) Drag for the wing

(d) The curve of the MAC airfoil

Figure 8.5: The results of the optimization without drag

## 8.4. THICKNESS OPTIMIZATION

Initial investigations found that all the solutions of the optimization tended towards making a thinner airfoil profile. Thus another investigation into the effect of solely reducing the thickness of the profile was performed. The thickness ratio between the root and tip of the wing has been left the same, as for the ATR72. Since there is only one variable, the thickness of the airfoil, the optimization is somewhat simpler, as a full

exploration of the design space can be done. For a number of difference thickness-to-chord ratios between the upper and lower bound of the thickness the objective functions, as described in Section 5.1, is evaluated. In this design space the point with the lowest error can then be selected, for further analysis. The thickness of the used NLR7301 airfoil is 16.5% at the thickness ratio is between the root and the tip is (13/18). The ratio of thickness between the root and tip are left the same, since this leads to better similarity.

It was chosen to only include the lift, moment and maximum lift coefficient in the objective function. This was done because when the drag was included in the objective, the resultant thickness proved no (real) improvements for the lift, moment and maximum lift coefficient. The weight factors for each coefficient were left at 1.

The results of the thickness optimization can be seen in Figure 8.6. As this is a one-dimensional optimization it is possible to look at the complete design space, in Figure 8.6a, here the change in objective value with a change in thickness is shown. The lower values of thickness have a large objective value associated with them, as these are too thin, and thus will likely exhibit different stalling behaviour. This explains the large drop in objective value at thickness-to-chord of 0.11, as the error value for airfoils with the wrong stall behaviour have an associated objective value of 10. A clear minimum is shown, which is at a thickness-to-chord ratio of 12.1%. The resultant airfoil is visible in Figure 8.6b. The aerodynamic analysis of the wing is given in Figure 8.7. The differences between the lift coefficient at fixed angle of attack range from 13% to -12%, the moment coefficient is between -14% and -9%. The drag coefficient, for fixed lift coefficient, is between 67% and 30%. The maximum lift coefficient is 1.32, which is 30% less than the full scale case. Again, further results such as spanwise lift distributions can be found in Appendix B.

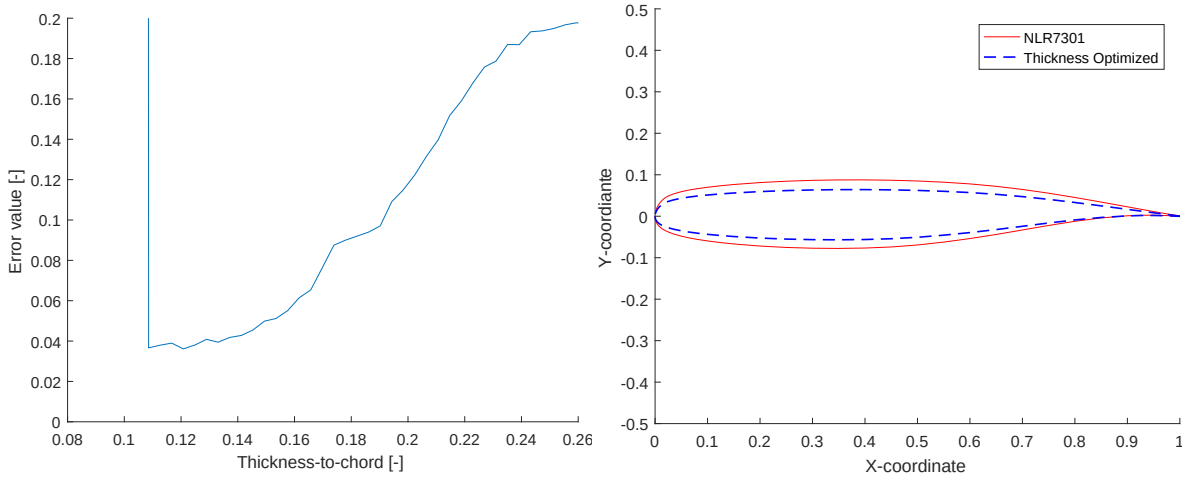


(a) Change in error with thickness

(b) Original and optimization airfoil

Figure 8.6: Results of the thickness optimization

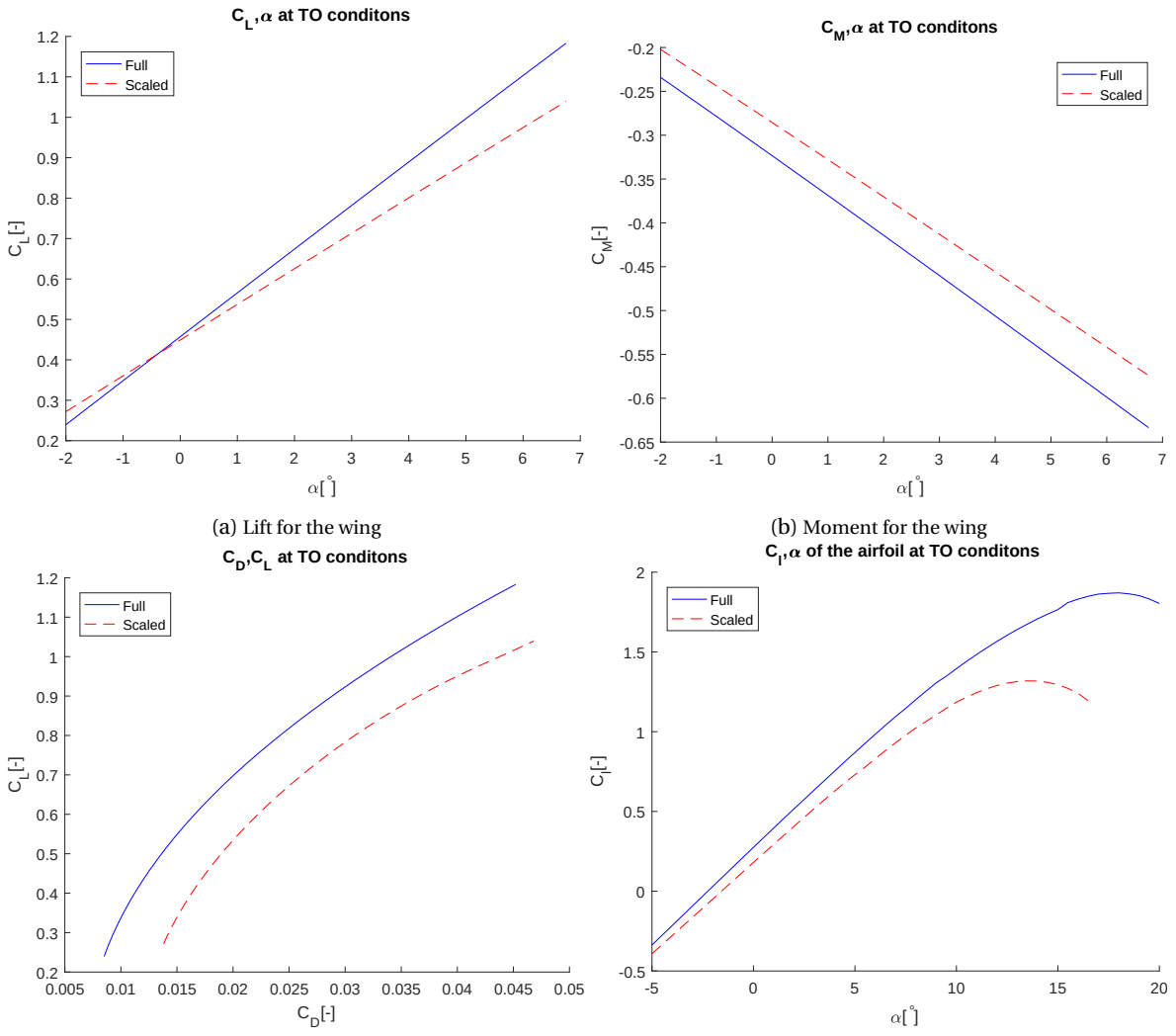


(a) Lift for the wing

(b) Moment for the wing

(c) Drag for the wing

(d) The curve of the MAC airfoil

Figure 8.7: The results of analysis of the thickness optimized airfoil

### 8.4.1. PERFORMANCE FOR WING WITH FLAP

While solely scaling the thickness may gave a better solution for the clean wing, there still is the question about the performance for the wing with flap. The thickness optimized case is selected for this, since it still has the same shape as the original airfoil and thus the same shape can be used for the wing with flap. Figure 8.8 shows the results for the full and scaled use case with flap 15 deg. As can be seen, the thickness optimized airfoil performs worse for all these three curves, it is further away from the full scale case than the simply scaled case. The maximum lift coefficient, which is where the clean case has an increase, can unfortunately not be calculated in this study.

It can then be concluded that the decreasing of thickness does not result in a better performance for the wing with flap and that there thus must be searched for an integrated optimal solution for both the clean and wing with flap case. This is, however, outside of the scope of this study.

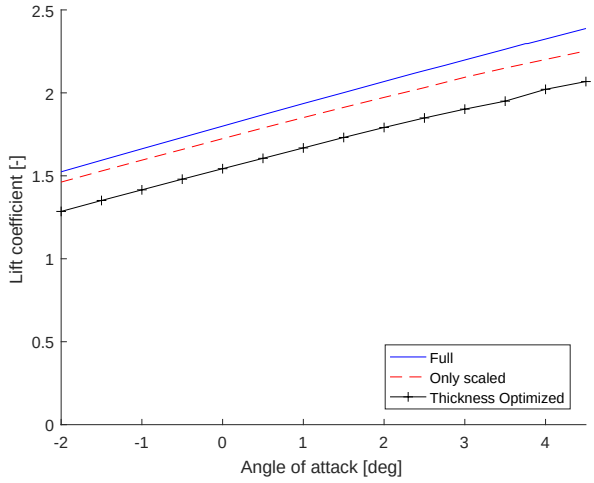


(a) Lift curve

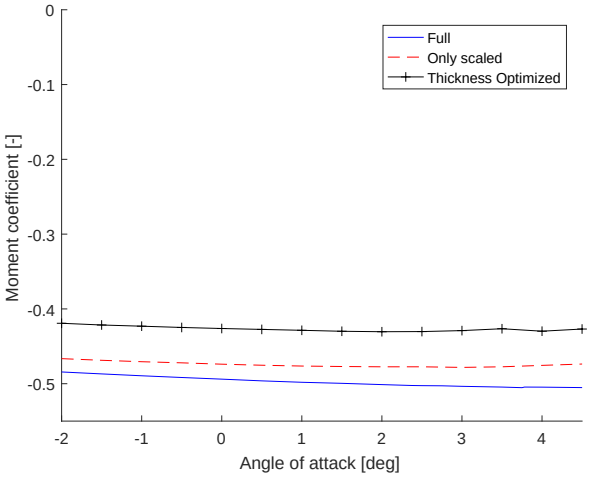


(b) Moment curve

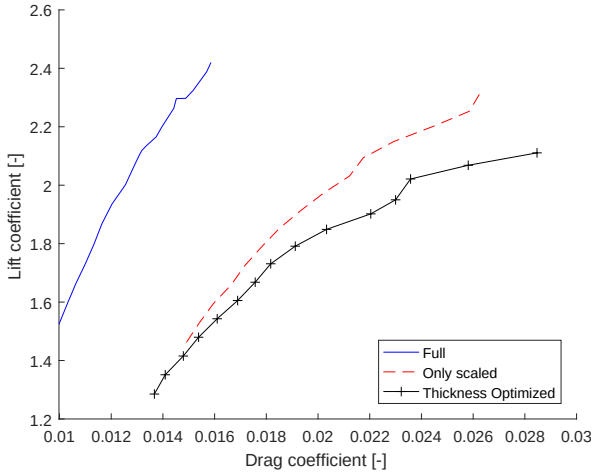


(c) Drag curve

Figure 8.8: Performance of the thickness scaled airfoil with flap

## 8.5. OFF-CONDITION PERFORMANCE

Until now only the performance in the take-off conditions have been investigated. In the following section the performance during the cruise conditions will be investigated, to see how the difference between the full and scaled model changes and if the optimized design also provides a higher degree of similarity.

The data for the cruise condition for both the scaled and full scale case are found in Table 8.1. The cruise conditions for the full scale aircraft are at $6096m$ (or $20000ft$) at approximately $250kts$, the mass is the maximum landing weight. For the scaled aircraft, it is not possible to just apply the scaling laws. Dutch aircraft law states that a remotely piloted vehicle may not fly above $450m$ [61] and needs to remain within visual range of the operator. Based on data found on other testing programs [4, 10, 62] an altitude of $150m$ is assumed and the aircraft is scaled accordingly. The cruise speed is set according to the Froude scaling. this gives a cruising velocity of $49m/s$. The Reynolds number for the full-scale case is 18.5 million and for the scaled case it is 0.853 million. As the optimized case the *Optimized with drag coefficient* is selected.

Table 8.1: Cruise condition parameters

| | Full | Scaled |
|---|---|---|
| Mass $[kg]$ | 19000 | 111.7 |
| Altitude $[m]$ | 6096 | 150 |
| Velocity $[m/s]$ | 128 | 49 |
| Reynolds number $[-]$ (million) | 18.5 | 0.853 |

The results of the analysis of the wing at cruise conditions are shown in Figure 8.9. The previously shown results for take-off conditions are also shown in these figures, they are marked with an asterisk ($*$). As can be seen, the lines for the two different conditions are close to each other.

For the lift in Figure 8.9a the differences between the full and scaled & optimized are greater. The optimized airfoil wing still provides a better result than the scaled, but the difference between the full and optimized have increased.

The moment of the different wings have also moved further apart under the cruise conditions, as can be seen in Figure 8.9b. Where the moment curves of the optimized and the full case are almost on top of each other for the take-off conditions, the lines are apart for the cruise conditions. Again, the performance of the optimized wing is better than the (just) scaled case.

Finally, for the drag it shows a shift in the curve to lower drag coefficients, which is to be expected when the Reynolds number increases. It can be concluded that the wings with the optimized airfoils perform better than the wings with the original airfoil, also in the cruise condition.

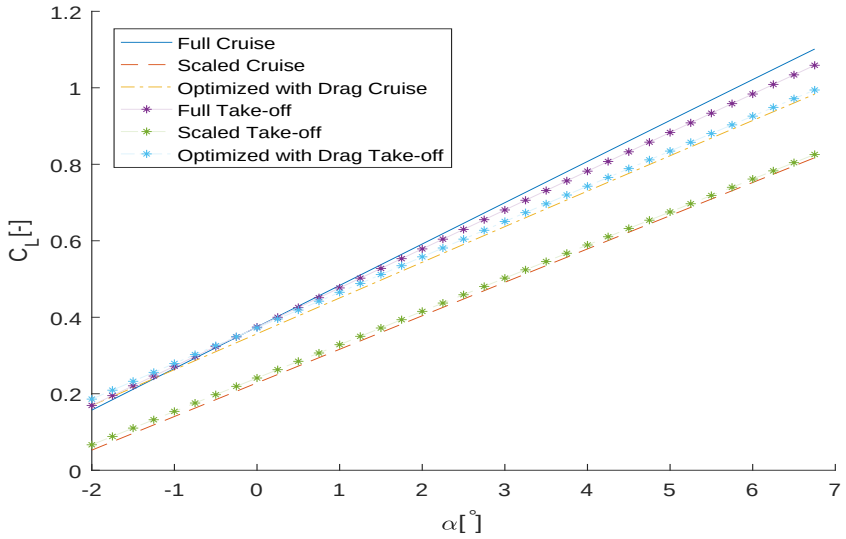


(a) Lift for the wing

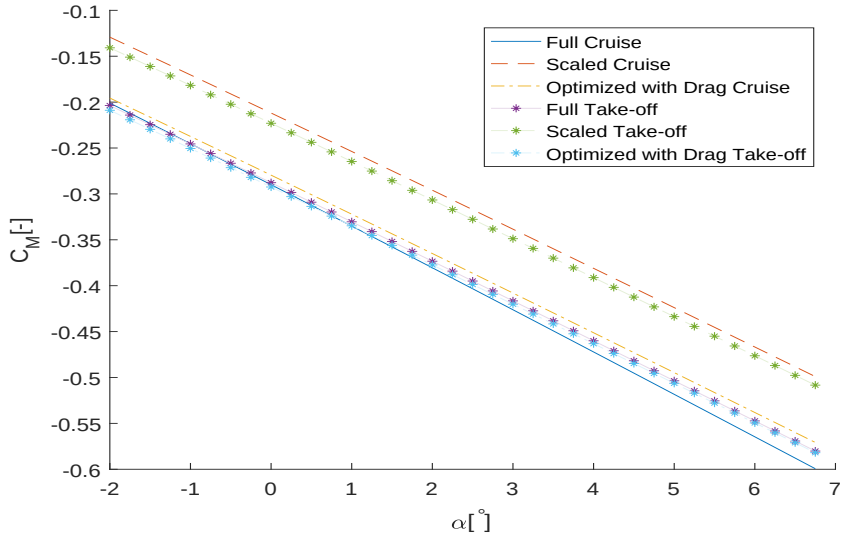


(b) Moment for the wing

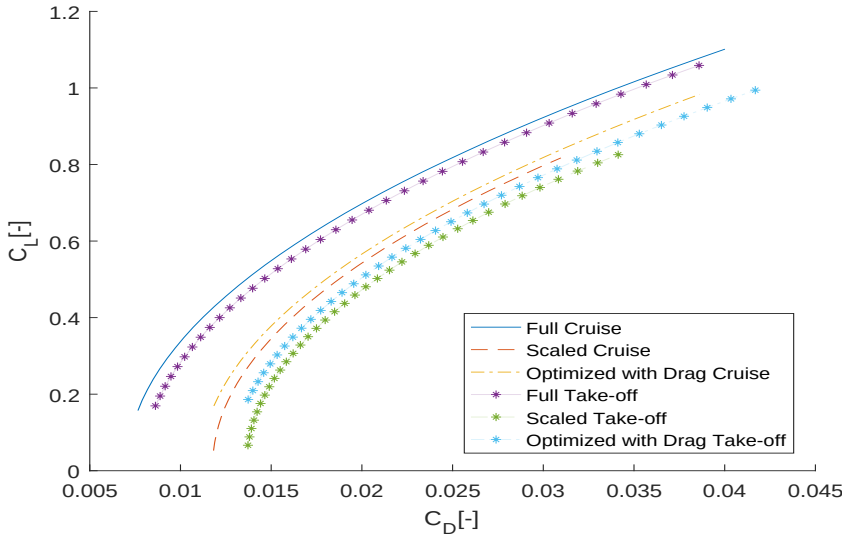


(c) Drag for the wing

Figure 8.9: Results of the scaled and optimized wing at cruise conditions

## 8.6. CONCLUSION

The various different optimized airfoils provide improvements in the similarity for the lift, moment, maximum lift and drag curve. An overview of the maximum differences for each of the aerodynamic properties, of the scaled with respect to the full scale is given in Table 8.2. Here, and in the preceding graphs, it is shown that already giving an incidence angle to the wing improved the similarity, however, further improvements are made when the airfoil shape is optimized. No large improvements are visible when excluding the drag coefficient from the objective, the reason behind this would require further investigation.

The maximum lift coefficient did not change significantly, when scaling with or without the drag included. Because all the solutions trended towards a thinner airfoil, an investigation was done into the effect of just changing the thickness of the airfoil, whilst keeping the overall shape as it was. Solely changing the thickness does result in a slightly better performance, however, it is not as good as those of the optimized airfoil shapes.

Table 8.2: Maximum differences found for the different wings

| *Maximum difference w.r.t full* | **Scaled** | **Scaled with incidence** | **Optimization with $C_D$** | **Optimization without $C_D$** | **Thickness Optimization** |
|---|---|---|---|---|---|
| $C_L$, same $\alpha$ | 60% | 17% | 11% | 8.1% | 13% |
| $c_{l,max}$ | 33% | 33% | 17.5% | 16.6% | 30% |
| $C_M$, same $\alpha$ | 30% | 4.5% | 5.5% | 5.7% | 14% |
| $C_D$, same $\alpha$ | 61% | 80% | 64% | 79% | 64% |
| $C_D$, same $C_L$ | 73% | 88% | 77% | 91% | 67% |

When the thickness optimized airfoil was tested with flaps the performance turned out to be poor, worse than the just scaled airfoil. Thus for the situation with flaps an integrated optimization solution must be employed, which was outside the scope of this study.

The optimized and scaled wing were also analysed in the cruise conditions. Here the gaps between the full size and the scaled and optimized increased when going from take-off to cruise conditions. However, the optimized airfoils did prove to be closer to the full case than the scaled case.

This chapter has shown that methods exist to improve the similarity between the full scale case, even though it does not (yet) lead to a full match. Only the airfoil shape has been used in this optimization, but other possibilities still exist, such as the washout or altering the planform itself, this is to be decided in future studies. Another next step is to verify if the improvements found here still exist if other aerodynamic analysis methods are used. On initial inspection the results do not seem like a numerical minimum, with no physical basis. The larger nose will lead to a higher lift and the the thinner airfoil does lead to lower drag, as the optimization with drag concluded.

# 9

# CONCLUSIONS

This final chapter is split in two parts, first the work done in the preceding thesis is concluded and after that the recommendations for future research are noted.

## 9.1. CONCLUSION

Atmospheric scaled free flight testing is an affordable way to quantify the dynamic properties of an aircraft. It enables different kind of test possibilities than a windtunnel. The additional possibilities and affordability make scaled flight testing an interesting complement to windtunnel testing. Several different scaled flight testing programs currently exist worldwide, most with a focus on dynamic flight testing. It is known that the aerodynamic properties change when an aircraft is scaled. However, most of the studies into the scaled flight testing models do not pay any attention to this, while this can be important. This can be especially relevant when new aircraft configurations are tested, for example a new tail set-up. The current research is a first step in the development of a scaled flight testing model and will highlight the differences between a full size and a (small) scale wing. This study has investigated the effect of scaling on the aerodynamic properties of a wing. This study had the objective of investigating the effect of scaling on the aerodynamic properties and of the flow field at the tail location. With the focus on take-off conditions. The take-off conditions are at sea level, international standard atmosphere and a velocity of 59 $m/s$ or Mach of 0.17.

Various different scaling techniques can be selected, for this study geometric, Froude and dynamic scaling is applied. The geometric scaling defines the dimensions of the aircraft, the Froude scaling determines the velocity and the dynamic scaling determines the mass of scaled model. The scale factor was decided on a maximum wing span, which still allows the model to be manageable in operations. The full scale case is analogous to a regional aircraft, the ATR72, with an unswept and slightly tapered wing and an optional 15° slotted Fowler flap. The scaled case is 14.7% geometric scaled. The take-off velocity becomes 23 $m/s$ or Mach 0.067.

The analysis of the aerodynamic properties was split between the clean wing and the wing with flap. The aerodynamic properties investigated were the lift, moment and drag curve, and the maximum lift coefficient. The clean wing was analysed using a quasi-3D analysis called Q3D, which is a combination of a vortex-lattice method (AVL) for the wing and a vortex panel method (XFOIL) for the airfoil. A modification of XFOIL, called RFOIL, is used to analyse the difference in maximum lift coefficient between the airfoil of the scaled and full scale case. RFOIL was selected because of the better prediction of the behaviour near and post-stall. The wing with flap is investigated using a vortex lattice method, in this case again AVL, where the (slotted) flap is modelled as an additional surface at the location of the flap, where the gap between the wing and the flap is filled with an extension of the flap surface. The airfoil with flap is investigated using the vortex panel implementation MSES, because it is able to correctly handle multi-element airfoils. Finally the maximum lift for the wing with flap is analysed with the semi-empirical Pressure Difference Rule. The pressure difference rule states that there is a ratio between the peak pressure and the trailing edge pressure, on a surface, at which maximum lift occurs.

The scaling of the wing proved to change the aerodynamic properties and thus the similarity was no longer present, for all the investigated aerodynamic properties. For both the wing with and without flap this

was the case. The clean wing showed a difference for the lift coefficient of up to 60% for equal angle of attack, the moment coefficient was offset by up to 30%. The drag coefficient of the clean wing showed difference up to 73% for a fixed lift coefficient. The 2D maximum lift coefficient was reduced by 33%. The wing with flap shows a difference in lift coefficient, for fixed angle of attack, of up to 37% and the lift distribution tended towards more outboard loading. The maximum lift of the wing with flap saw a reduction of approximately 29%. A basis for this was found in the different boundary layer properties, the scaled wing exhibited a relatively thicker boundary layer, leading to a decambering effect, and laminar separation bubbles were found to occur. The decambering causes the change in lift and moment curve. The thicker boundary along with the laminar separation bubbles cause the increase in drag.

An analysis of the wake field is done using methods developed by the ESDU. The wake properties of both the scaled as well as the full scale are calculated using ESDU80020 and ESDU97021, for clean and flapped wing respectively. Both methods use semi-empirical methods to determine the location of the vortex sheet. The dimensions and velocity loss of the wake itself can be calculated using either a method by ESDU or a method by Schlichting.

The scaled wing exhibited a thicker wake, with a larger associated velocity loss. The wake of the scaled wing was 46% wider and had a 32% higher velocity deficit associated with it. The scaled wing with flap showed an increase of 14% in the wake thickness and 19% greater velocity deficit. The difference between the full and scaled clean wing was thus larger than the difference between the full and scaled wing with flap. The reason for the difference between the full and scaled wing can be found in the increased drag (coefficient) of the clean scaled wing, this difference was larger for the clean wing than for the scaled wing. The downwash model used predicted an equal downwash for both the scaled and full clean wing and showed a reduction in downwash angle for the wing with flap. For the clean wing this exhibits the limit of the model used in this study. It is expected that the downwash for the clean wing will change when scaling down, as the lift generated by the wing will change.

In order to increase the similarity between the full and scaled wing it was investigated to change the airfoil shape. Due to the numerical difficulties that were found when using MSES for the wing with flap, this optimization was only performed on the clean wing. The input of the optimization was the shape of the airfoil, which was parametrized using the Class/Shape Transformation (CST). The objective to minimize was the sum of the difference between the full scale and scaled values for the lift, moment and drag coefficient at two different angles of attack. The optimization was performed using a combination of a genetic algorithm, in order to fully capture the whole design space, and a SQP-algorithm in order to ensure a (local) minimum.

Improvements were visible for the optimized airfoil, on all the aerodynamic properties. The difference between the full and scaled case were reduced to a maximum difference of 11% for lift coefficient and 5.5% for moment coefficient, at a fixed angle of attack. The 2D maximum lift coefficient was improved by 22% compared to the scaled case. The optimized airfoil shapes tended towards a thinner airfoil and thus an investigation into solely optimizing the thickness of the airfoil was also done. This also proved to give better results than the original airfoil, however, the airfoil shape optimized wings gave better results, for lift, moment and maximum lift coefficients. It showed a slight improvement for the lift and moment coefficients. The maximum lift coefficient was improved by only 5%. This thinner profile also proved to decrease the performance of the wing with flap. In cruise conditions the optimized airfoils still performed better than the original airfoil, however, the difference between the full and scaled wing did increase for the lift and moment curves. For the drag curve the difference remained about equal.

The results were found using low fidelity methods, it is believed that these methods still provide a definite indication of the phenomena that will occur when scaling is applied. While modification of the airfoil shape can provide a better similarity of the clean wing, when investigating the flapped case it proved that solution actually decreased the performance there. This means that in order to achieve good similarity throughout the regime an integrated solution must be found for all the different configurations and flight conditions.

All of the methods are already validated at both low and high Reynolds number and for straight tapered wings, in literature. While the low fidelity methods do allow for a wide range of configurations and conditions, with low computational times, complete accuracy is not guaranteed. The differences found between the full and scaled wing will still exist when actual testing is performed, but the magnitude of the differences found may be different to those found in this study. An example of this are the results found in this study for an airfoil with

flap under certain Reynolds numbers. In this case MSES did always not reach a proper converged solution and as a result gives incorrect solutions and care must be taken when analysing the results.

At this point, the scale factor used in the analysis was determined based on a maximum wing span of $4m$, however, this is perhaps not the best base on which the sizing is done. Other, important, factors also come into play, such as cost, instrumentation and control. With cost, it can be said, that bigger becomes more expensive, but as size decreases, the manufacturing tolerances also decrease, so that could make it in turn more expensive. With respect to instrumentation and control, there is the question of what is the resolution your instruments can still measure and what are the dimensions in which full control can still be achieved.

This research is the first step into the development of a scaled flight testing model and as such has highlighted the difficulties and discrepancies which will be faced when scaling is performed. The next step in research is to determine how these difference between the full and the scaled model and determine what the influence on the actual tests are. An atmospheric free flight scaled model is not the proper tool to investigate the exact aerodynamic properties of a new configuration, as this research made clear. The results will be different, due to the difference in Reynolds number. When attempting to do a dynamic flight testing campaign scaled flight testing is useful, since it allows for large manoeuvres which use a lot of (air) space. Further research is needed to investigate how the difference in aerodynamic properties influence the dynamic tests.

Scaled flight testing is a powerful tool, but consideration must be given to the design in order to guarantee the similarity of the results.

## 9.2. RECOMMENDATIONS

There are several different types of suggestions after this research, suggestions pertaining to the methods used and suggestions that apply to further research.

The results of a research are only as good as the assumptions it is based on and for this research this is no different. Numerous (implicit) assumptions have been made in this study, in order to be able to model a wing (with flap), but still being able to do that within the fixed amount of time and resources in a master's thesis.

**Investigate different methods of boundary layer tripping** Initial investigations, in Section 6.1.2, showed that forcing transition did get rid of the laminar separation bubbles. However, what the best location or best method for this transition and the further implications are has not yet been investigated.

**Transition method in XFOIL/RFOIL/MSES, lower Reynolds numbers could lead to different turbulence models** Currently the aerodynamic analysis modules have been ran with the $e^n$-transition model, with $n = 9$ as a default value. For atmospheric scaled flight testing this value will likely be different, due to the turbulence in the air, however no reliable source could readily be found. The influence of different values of $n$ also is something which is still to be investigated.

**Maximum lift for flaps at lower Reynolds and Mach number** The pressure difference rule is currently limited to Reynolds numbers above 1 million, however, of interest in this study is also flight below this Reynolds number. Either the method must be expanded or another method must be selected for the maximum lift coefficient.

**Expand the methods with higher fidelity models such as CFD for the aerodynamic analysis** The analyses in this study have been done with fairly basic methods, the benefit of this was that these methods are rapid, robust and allow for a wide range of configurations, the downside is that the accuracy is not optimal. Other analytical tools can increase this accuracy, however, they are slower and less robust.

**Expand the methods with higher fidelity models with physics based models for the wake** The model used for the wing with flap is partly physics based, while the method used for the clean wing uses only empirical methods. This means that there is room for improvement here

**Investigate the effect of the optimization on the wake** Currently the optimized airfoils have not been included in the wake analyses. Since the optimization also proved to give reductions in drag, it is likely that the similarity of the wake should also increase. This has not been investigated yet and is an interesting next step to take.

**Integrated optimization for flapped and clean wing** As was shown, the better results for the clean wing do not necessarily translate to the flapped wing. In fact, it was found that in this case it lead to worse performance of the wing with flap. This is why the next is to integrate the optimization of the clean wing with an optimization of the wing with flap, to get better results. To investigate if there exist certain ways to improve the similarity of the scaled wing with flap, a different analysis method must be selected. Currently, the stability and convergence issues with MSES do not make it suitable for a design loop.

**Incorporate the effects of the body into the analyses** Currently the body is only taken into account, to a limited degree, in the wake models. The other methods have excluded the effects of the body. It is likely that the effects of the body are not the same for the full scale case as for the scaled case. Better methods have to be found in order to incorporate this.

The following recommendations are the larger steps that have to be taken before the actual building of a scaled flight testing model can be done.

**Determining the exact goals of a scaled flight testing program** As has been seen, the difference between the full and scaled model is dependant on the scale and flight conditions. In order to be able to verify a design of scaled flight testing model, first it must be known what kind of tests are to be flown with a scaled flight testing model. In this study the longitudinal static stability was briefly investigated and it was found that scaling definitely has an influence on that. This will likely also be the case on other stability and control parameters, however the extent is not known. In order to properly design a new scaled flight testing model, first the testing campaign which it will be subjected to must be known, to be able to predict performance.

**Determining the influence of scaling on the results of experimental flight tests** Once the kind of tests are known the scaled flight testing model and full scale case can both be simulated in these situations and verify if the outcomes match. If not, then steps can be taken to ensure a correct response. This does require the complete knowledge of the response of the full scale aircraft to these test conditions as well, to make sure the baseline configuration performs the same. After that tests can be performed on new configurations.

**Windtunnel testing of the complete wing and aircraft** The final step, before actually performing the test program, would be to validate the design in a windtunnel, in order to check if all the effects have been properly accounted for, to see if the predicted results are correct.

# BIBLIOGRAPHY


[1] J. R. Chambers, *Modeling Flight: The Role of Dynamically Scaled Free-Flight Models in Support of NASA's Aerospace Programs*. US National Aeronautics and Space Administration, 2009.

[2] D. Cox, K. Cunningham, and T. Jordan, "Subscale Flight Testing for Aircraft Loss of Control: Accomplishments and Future Directions," in *AIAA Guid. Navig. Control Conf.* Reston, Virigina: American Institute of Aeronautics and Astronautics, Aug 2012.

[3] M. J. Hinton and C. N. Eastlake, "The construction and flight testing of a scaled, remotely-piloted, flight-test vehicle," in *ASEE Annu. Conf. Expo. Eng. Educ. to Serve World*, Charlotte, NC, 1999, pp. 4855–4861.

[4] L. Eveleens and F. Bremmers, "Free flying scale model flight testing - future or fiction?" in *SFTE-EC Symp.*, Nürnberg, 2016.

[5] K. Pettersson and A. Rizzi, "Aerodynamic scaling to free flight conditions: Past and present," *Prog. Aerosp. Sci.*, vol. 44, 2008.

[6] R. Vos and S. Farokhi, *Introduction to Transonic Aerodynamics*, 1st ed., ser. Fluid Mechanics and Its Applications. Dordrecht: Springer Netherlands, 2015, vol. 110.

[7] M. Scherberg and R. Rhode, "Mass Distribution and Performance of Free Flight Models," NACA, Tech. Rep., 1927.

[8] T. Jordan, W. Langford, and J. Hill, "Airborne Subscale Transport Aircraft Research Testbed - Aircraft Model Development," in *AIAA Guid. Navig. Control Conf. Exhib.* Reston, Virigina: American Institute of Aeronautics and Astronautics, Aug 2005.

[9] T. Jordan and R. Bailey, "NASA Langley's AirSTAR Testbed: A Subscale Flight Test Capability for Flight Dynamics and Control System Experiments," in *AIAA Guid. Navig. Control Conf. Exhib.* Reston, Virigina: American Institute of Aeronautics and Astronautics, Aug 2008.

[10] D. Kuehme, N. R. Alley, C. Phillips, and B. R. Cogan, "Flight Test Evaluation and System Identification of the Area-I Prototype-Technology-Evaluation Research Aircraft (PTERA)," in *AIAA Flight Test. Conf.*, no. June. Reston, Virginia: American Institute of Aeronautics and Astronautics, Jun 2014.

[11] N. Alley, J. Steele, J. Neidhoefer, R. Englar, and G. Blaylock, "Development of a Cruise-Efficient Extreme-STOL Capable Demonstrator UAV," in *AIAA Infotech@aerosp. 2010*, no. April. Reston, Virigina: American Institute of Aeronautics and Astronautics, apr 2010.

[12] P. Schmollgruber, J.-L. Gobert, P.-E. Gall, Z. Goraj, H. W. Jentink, A. Näs, and R. Voit-Nitchmann, "An innovative evaluation platform for new aircraft concepts," *Aeronautical Journal*, vol. 114, no. 1157, pp. 451–456, Jul 2010.

[13] J. Frota, K. Nicholls, J. Whurr, M. Müller, P.-E. Gall, J. Loerke, K. Macgregor, P. Schmollgruber, J. Russell, M. Hepperle, S. Rodriguez, K. Taupin, J.-L. Godard, S. Dron, K. Plötner, and G. Gallant, "NACRE Final Activity Report 2005-2010," no. Sixth Framework Program Aeronautics and Space FP6-2003-AERO-1, 2011.

[14] M. Richards, J., Suleman, A., Canfield, R., Blair, "Design of a Scaled RPV for Investigation of Gust Response of Joined-Wing Sensorcraft," *50th AIAA/ASME/ASCE/AHS/ASC Struct. Struct. Dyn. Mater. Conf.*, May 2009.

[15] J. Heeg, C. Spain, and J. Rivera, "Wind Tunnel to Atmospheric Mapping for Static Aeroelastic Scaling," in *45th AIAA/ASME/ASCE/AHS/ASC Struct. Struct. Dyn. Mater. Conf.* Reston, Virigina: American Institute of Aeronautics and Astronautics, Apr 2004.

[16] J. Richards, T. Aarons, J. Garnand-Royo, A. Suleman, R. Canfield, and C. Woolsey, "Airworthiness Evaluation of a Scaled Joined-Wing Aircraft," in *53rd AIAA/ASME/ASCE/AHS/ASC Struct. Struct. Dyn. Mater. Conf.* Reston, Virigina: American Institute of Aeronautics and Astronautics, Apr 2012.

[17] C. A. Eger, A. Ricciardi, R. A. Canfield, and M. Patil, "Design of a Scaled Flight Test Vehicle Including Linear Aeroelastic Effects," in *54th AIAA/ASME/ASCE/AHS/ASC Struct. Struct. Dyn. Mater. Conf.* Reston, Virginia: American Institute of Aeronautics and Astronautics, Apr 2013.

[18] T. Risch, G. Cosentino, C. Regan, M. Kisska, and N. Princen, "X-48B Flight Test Progress Overview," in *47th AIAA Aerosp. Sci. Meet.* Orlando, Florida: American Institute of Aeronautics and Astronautics, Jan 2009.

[19] N. Van Arnhem, "DUUC aircraft with the innovative 'Propulsive Empennage' concept," 2016. [Online]. Available: https://www.youtube.com/watch?v=VDbJBkcQBPI

[20] C. H. Wolowicz and J. S. Bowman, "Similitude Requirements and Scaling Relationships as Applied to Model Testing," *NASA Tech Rep*, Aug 1979.

[21] Z. Wan and C. E. Cesnik, "Geometrically Nonlinear Aeroelastic Scaling for Very Flexible Aircraft," in *54th AIAA/ASME/ASCE/AHS/ASC Struct. Struct. Dyn. Mater. Conf.*, no. AIAA 2013-1894. Reston, Virginia: American Institute of Aeronautics and Astronautics, Apr 2013.

[22] D. Lundström and K. Amadori, "RAVEN – A SUBSCALE RADIO CONTROLLED BUSINESS JET DEMONSTRATOR," in *26th Int. Congr. Aeronaut. Sci.*, 2008.

[23] J. D. Anderson, *Fundamentals of Aerodynamics*, international ed. McGraw-Hill, 2007.

[24] C. L. Ladson, "Effects of Independent Variation of Mach and Reynolds Numbers on the Low-Speed Aerodynamic Characteristics of the NACA 0012 Airfoil Section," Tech. Rep., 1988.

[25] H. Schlichting, *Boundary Layer Theory*, 3rd ed. McGraw-Hill, 1979.

[26] R. Rudnik and E. Germain, "Re-No. Scaling Effects on the EUROLIFT High Lift Configurations," in *45th AIAA Aerosp. Sci. Meet. Exhib.* Reston, Virigina: American Institute of Aeronautics and Astronautics, Jan 2007.

[27] L. Veldhuis, "Aircraft Aerodynamic Lecture Notes," Delft University of Technology, Delft, Tech. Rep., 2014.

[28] B. Heine, S. Mack, A. Kurz, A. Gross, and H. Fasel, "Aerodynamic Scaling of General Aviation Airfoil for Low Reynolds Number Application," in *38th Fluid Dyn. Conf. Exhib.* Reston, Virigina: American Institute of Aeronautics and Astronautics, Jun 2008.

[29] D. E. Gault, "A Correlation of low-speed, airfoil-section stalling characteristics with Reynolds number and airfoil geometry - Technical Note 3963," National Advisory Committee for Aeronautics, Tech. Rep., 1957.

[30] Anonymous, "ATR72 Flight Crew Operating Manual," ATR, Tech. Rep., 1999.

[31] Anon., "WikiMedia Commons," 2012.

[32] Anonymous, "Jane's All the World's Aircraft," IHS, Tech. Rep., 2017. [Online]. Available: http://Janes.ihs.com/JAWADevelopmentProduction/Reference [Accessed: 2017-03-15]

[33] W. Molyneux, "Aeroelastic Modelling," Tech. Rep. Structures 353, 1964.

[34] J. Katz and A. Plotkin, *Low-Speed Aerodynamics*, international edition ed. McGraw-Hill, Inc, 1991.

[35] H. Garner, "The maximum lift coefficient of plain wings at subsonic speeds," Tech. Rep. October 1989, 1993.

[36] C. P. Van Dam, "The aerodynamic design of multi-element high-lift systems for transport airplanes," *Prog. Aerosp. Sci.*, vol. 38, no. 2, pp. 101–144, 2002.

[37] A. Smith, "High-Lift Aerodynamics," *Journal of Aicraft*, vol. 12, no. 6, pp. 501–530, Jun 1975.

[38] R. Pepper, C. van Dam, and P. Gelhausen, "Design methodology for high-lift systems on subsonic transport aircraft," *6th Symp. Multidiscip. Anal. Optim.*, pp. 707–723, 1996.

[39] C. Werner-Spatz, W. Heinze, and P. Horst, "Improved Representation of High-Lift Devices for a Multidisciplinary Conceptual Aircraft Design Process," *Journal of Aicraft*, vol. 46, Nov 2009.

[40] F. Dorbath, B. Nagel, and V. Gollnick, "Physics-Based Wing Mass Estimation in Early Design Stages," in *28th Int. Congr. Aeronaut. Sci.*, Bistbane, Australia, 2012.

[41] E. Moerland, "Development of an aeroelastic analysis tool for structural sizing of high-lift devices during preliminary design," Delft University of Technology, Tech. Rep., 2011.

[42] B. Singh, "A Medium-Fidelity Method for Rapid Maximum Lift Es- timation," Delft University of Technology, Tech. Rep., 2017.

[43] J. Mariens, A. Elham, and M. J. L. van Tooren, "Quasi-Three-Dimensional Aerodynamic Solver for Multidisciplinary Design Optimization of Lifting Surfaces," *Journal of Aicraft*, no. 2, 2014.

[44] M. L. Purser, Paul E., Spearman, "Wind- Tunnel Tests At Low Speed Of Swept And Yawed Wings Having Various Plan Forms," Tech. Rep., 1951.

[45] M. Drela and H. Youngren, "Athena Vortex Lattice 3.36," 2017. [Online]. Available: http://web.mit.edu/drela/Public/web/avl/

[46] J. L. van Ingen, "Historical review of work at TU Delft," *38th Fluid Dyn. Conf. Exhib.*, no. June, pp. 1–49, 2008.

[47] M. Drela and M. B. Giles, "Viscous-inviscid analysis of transonic and low Reynolds number airfoils," *AIAA Journal*, Oct 1987.

[48] R. van Rooij, "Modification of the boungary layer calculation in RFOIL for improved airfoil stall prediction IW-96087R," Delft University of Technology, Tech. Rep., 1996.

[49] W. Valarezo and V. D. Chin, "Method for the prediction of wing maximum lift," *Journal of Aicraft*, vol. 31, no. 1, pp. 103–109, 1994.

[50] P. Jones, "ESDU 80020 - Average downwash at the tailplane at low angles of attack and subsonic speeds," ESDU, Tech. Rep., 2012.

[51] F. Vaessen, "Improved aerodynamci analysis to predict wing interactions of high-subsonic three-surface aircraft," Delft University of Technology, Tech. Rep., 2013.

[52] H. Garner, "ESDU 97021 - Effect of trailing-edge flap deployment on average downwash at the tailplane at low speeds," ESDU, Tech. Rep. September, 2012.

[53] Anonymous, "ESDU AERO 05.01.01 Kinetic Pressure in the Wake Behind a Wing," ESDU, Tech. Rep., 1981.

[54] EASA, "Certification Specifications for Large Aeroplanes CS25," 2007. [Online]. Available: http://www.easa.europa.eu/agency-measures/docs/certification-specifications/CS-25/CS-25{_}Amdt3{_}19.09.07{_}Consolidatedversion.pdf

[55] B. Kulfan and J. Bussoletti, ""Fundamental" Parameteric Geometry Representations for Aircraft Component Shapes," *11th AIAA/ISSMO Multidiscip. Anal. Optim. Conf.*, 2006.

[56] K. Lane and D. Marshall, "A Surface Parameterization Method for Airfoil Optimization and High Lift 2D Geometries Utilizing the CST Methodology," *47th AIAA Aerosp. Sci. Meet. Incl. New Horizons Forum Aerosp. Expo.*, no. January, 2009.

[57] "MATLAB - How the Genetic Algorithm Works." [Online]. Available: https://nl.mathworks.com/help/gads/how-the-genetic-algorithm-works.html [Accessed: 2017-03-16]

[58] Anonymous, "Constrained Nonlinear Optimization Algorithms." [Online]. Available: https://nl.mathworks.com/help/optim/ug/constrained-nonlinear-optimization-algorithms.html{#}bsgppl4 [Accessed: 2017-03-16]

[59] P. Y. Papalambros and D. J. Wilde, *Principles of Optimal Design*, 2nd ed. Cambridge University Press, 2000.

[60] D. P. Raymer, *Aircraft Design: A Conceptual Approach*, 2nd ed. Washington, DC: AIAA Education Series, 1992, vol. 128, no. 4.

[61] Anonymous, "Regeling Modelvliegen," 2015. [Online]. Available: http://wetten.overheid.nl/BWBR0019147/2015-11-07

[62] J. P. Fielding, C. P. Lawson, R. Pires, and G. Monterzino, "Development of the Demon Technology Demonstrator UAV," *Icas 2010*, pp. 1–7, 2010.

# A

# ESDU DOWNWASH MODEL BACKGROUND

The following appendix aims to provide further background on the ESDU models used in this research to calculate the downwash; it is an expansion of the text given in Chapter 4. In the following text the notation of a horizontal tail will be used, but in the used methods it is not relevant what is actually at the location of this tail, as the tail itself has no influence on the downwash in this method.

## A.1. ESDU 80020

The downwash for the clean wing is calculated using Equation (4.1), given here again in Equation (A.1). This calculates the average downwash over the width of a horizontal tail and is dependant on the zero wing-body lift and the downwash gradient. It is assumed that the wake lies in the aircraft's zero-lift plane, as indicated in Figure 4.2. All the dimension used by this method are given in Figure A.1 and all the following text has been based on the manual, accompanying the software model [50]. Note that with tailplane height the distance from the wake to the tailplane (or location in the wake survey plane) is meant, not the height above the wing, so $\zeta$ in Figure A.1.

$$\varepsilon = \varepsilon_0 + (\frac{d\varepsilon}{d\alpha})(\alpha - \alpha_0) \tag{A.1}$$

The calculation of the downwash is done by determining the following properties and taking the following steps:

- Downwash gradient at zero tailplane height (i.e. the tailplane is directly in the wake)
- Effect of tailplane height on downwash gradient
- Downwash at zero-lift
- Effect of compressibility

#### DOWNWASH GRADIENT AT ZERO TAILPLANE HEIGHT

First the downwash in the wake is determined, based on spanwise loadings from a lifting line theory, corrected with empirical factors. The starting point is the downwash of an elliptical loaded wing at an infinite distance behind the wing, based on lifting line theory. That value is then corrected for a tail surface at finite distance ($\xi$) and non-elliptical loading, by using empirically derived factors. Finally a correction is made, based on empirical data, for the presence of the body.

#### EFFECT OF TAILPLANE HEIGHT ON DOWNWASH GRADIENT

The effect of the tailplane height with the downwash gradient is a linear effect, derived from experimental data. As Figure 4.1 illustrates, the downwash decrease with height above the wake core.

#### DOWNWASH AT ZERO-LIFT

The average downwash at zero-lift is influenced by a number of things, such as tailplane location (both $\xi$ and $\zeta$), body geometry, wing twist and Reynolds number. However, in this method it is assumed, based on experimental that the main factor of influence is the tailplane height and the rest is neglected. This, however, does lead to a large uncertainty of this value, the uncertainty is approximately 1 degree.

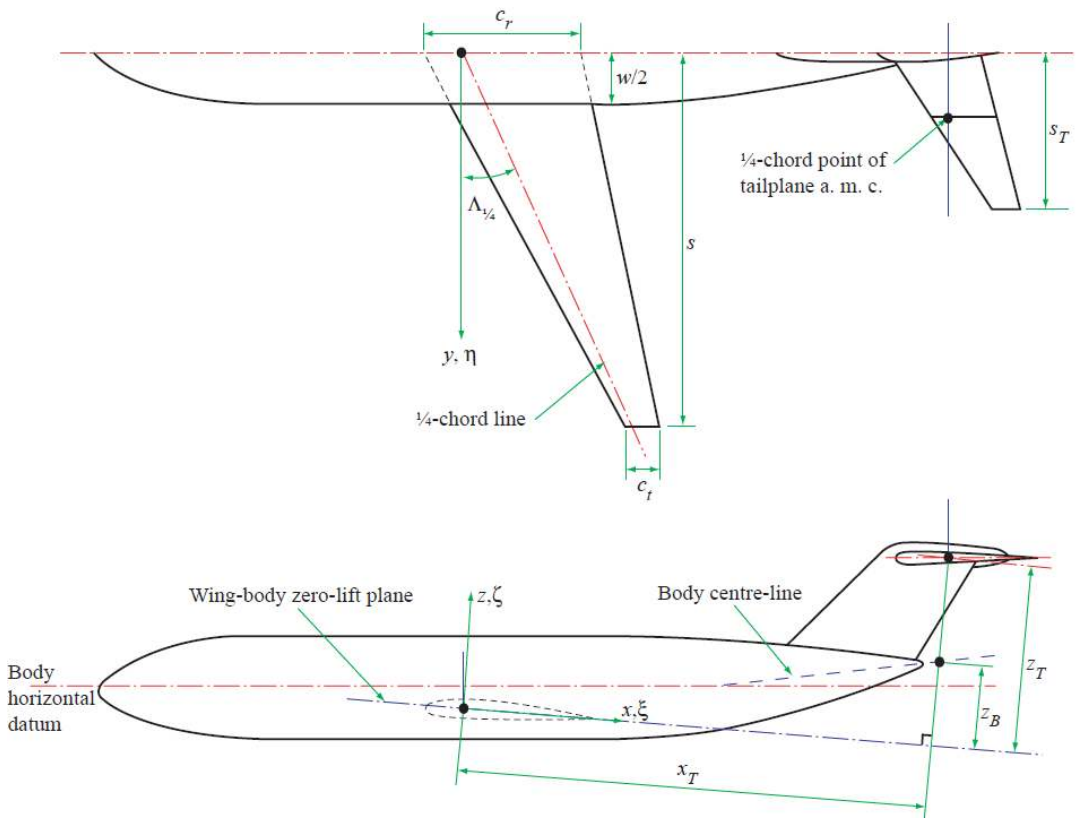


Figure A.1: Dimensions used in ESDU80020 [50]

#### EFFECT OF COMPRESSIBILITY

The effect of compressibility is relatively small, until the Mach divergence number, after that the results start to diverge rapidly. The current study is not concerned with tests in this region, thus it is of no worry. Below the drag divergence number a correction factor for the Mach is calculated using experimental data.

## A.2. ESDU 97021

The ESDU97021 software is used to calculate the additional downwash component due to flap extension. It uses empirical factors to go from a inviscid theoretical method of a straight-tapered wing with plain flaps, to a generic wing, within the limits of the model. The downwash behind a wing with flap is approximated by the use of a system of horeshoe vortices, which are shed as a plane from the wing quarter-chord line. However, two fixes have to be applied to this method, as the vortex is not shed from the wing quarter-chord point, but from the flap trailing edge and the vortex curves as it moves downstream. This is why an equivalent vortex sheet is used, this vortex sheet has a vertical displacement, from the wing quarter chord point.

The method predicts the values of the average downwash over the tailplane with a margin of ±15%, as can be seen in Figure A.2.

The model takes the following steps [52]:

- Calculation of the theoretical downwash
- Determination of vortex core
- Determination of the downwash value

#### THEORETICAL DOWNWASH

As the basis for this method a database of values has been calculated using the theoretical method and a set of datum values. These datum values are $\lambda = 0.3$, $c_f/c = 0.25$, $\eta_T = 0.4$ and $M = 0.2$. For wings which are not exactly equal to this standard wing, correction factors are applied in the subsequent steps, based on experimental data.

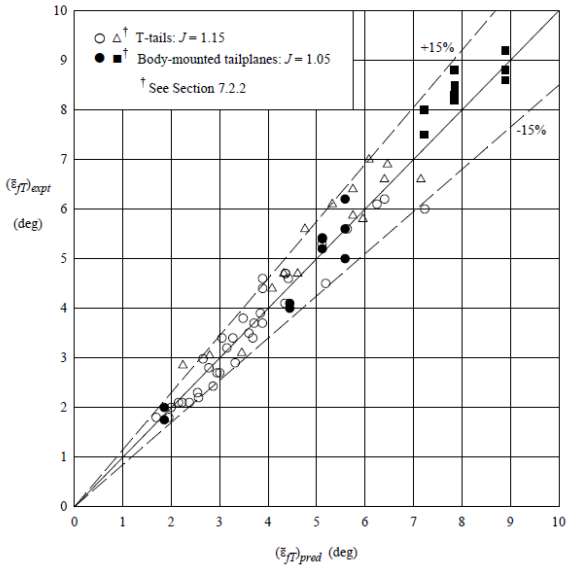


Figure A.2: The predicted downwash values compared with the average values [52]

**VORTEX CORE LOCATION**

The vortex core is placed vertically down from the wing quarter-chord in two steps. First it is displaced by the vertical position of the trailing edge of the flaps. Next it is displaced by the curvature of the vortex sheet, to replicate the vertical movement of the vortex at the location of the tail. The vertical displacement is mainly dependant on the lift generated by the flaps and the aspect ratio of the wing, and to a lesser degree on taper ratio, flap chord, and tailplane location.

The vortex location is proportional to the lift coefficient of the flaps and inversely proportional to the aspect ratio. The other factors are accounted for by using empirical value to relate those values to the datum values.

**DOWNWASH VALUE**

The calculation of the actual average downwash value over the tail is roughly analogous to the vortex core location, it is proportional to the lift coefficient of the flaps and inversely proportional to the aspect ratio. And again the other factors are accounted for by using empirical correction factors. The exact value of the correction factors will of course differ from that of the vortex core. However, for the downwash value it was found that below $M = 0.4$ there were very minor effects of the Mach number, so for the downwash value the effect of Mach is neglected.

Another difference for the downwash value is an additional correction factor for the tail location, with respect to the body. There was a clear difference found in

# B

# ADDITIONAL RESULTS

This appendix has further graphs showing results of the wake analysis at a different angle of attack and of the analysis of optimized wings.

## B.1. EXTRA RESULTS WAKE ANALYSIS

The following section has the results of the analysis of the wake at an angle of attack of zero degrees. The results are similar to those found in Chapter 7. It shows a slightly thinner wake, with a smaller associated velocity deficit, as expected.

### B.1.1. CLEAN FULL

Figure B.1 has the results of the wake analysis of the full scale clean wing. With a lower velocity deficit and a slightly thinner wake. This is because the wing generates less drag and produces less lift. The wake core is in the same location as the angle of attack 5 degrees case.

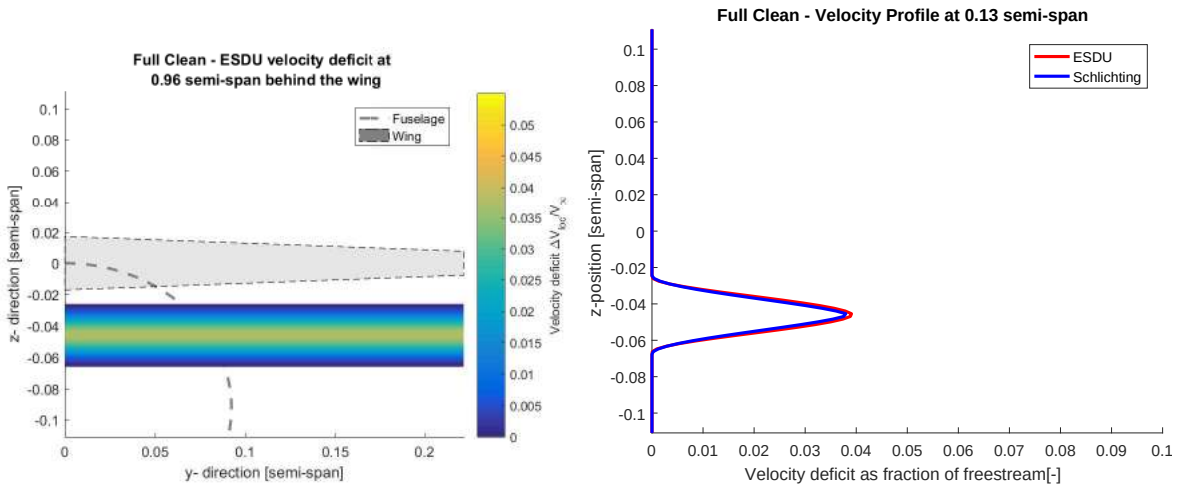


(a) Wake profile of the clean wing, ESDU wake model

(b) Clean wing velocity profile, at wake survey plane

Figure B.1: Results of the wake calculations for the full clean wing

### B.1.2. CLEAN SCALE

Figure B.2 has the results of the wake analysis of the scaled clean wing. The same trend can be seen here as when comparing the full scale case of 0 and 5 degrees.

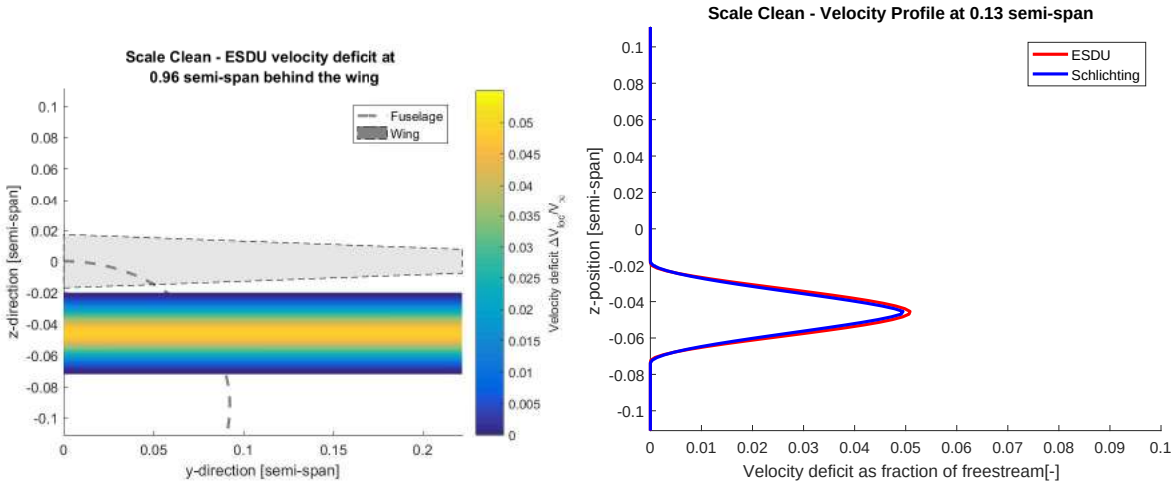


(a) Wake profile of the clean wing, ESDU wake model

(b) Velocity profile of the clean wing

Figure B.2: Results of the wake calculations for the scaled clean wing

### B.1.3. FLAP FULL

In Figure B.3 the results of the full wing with flap are shown, at an angle of attack of zero degrees. Now the core is located somewhat higher than the core of the wake at an angle of attack of 5 degrees, as was expected. Other than that, the trend is the same as for the clean wing, a thinner wake with less velocity deficit.

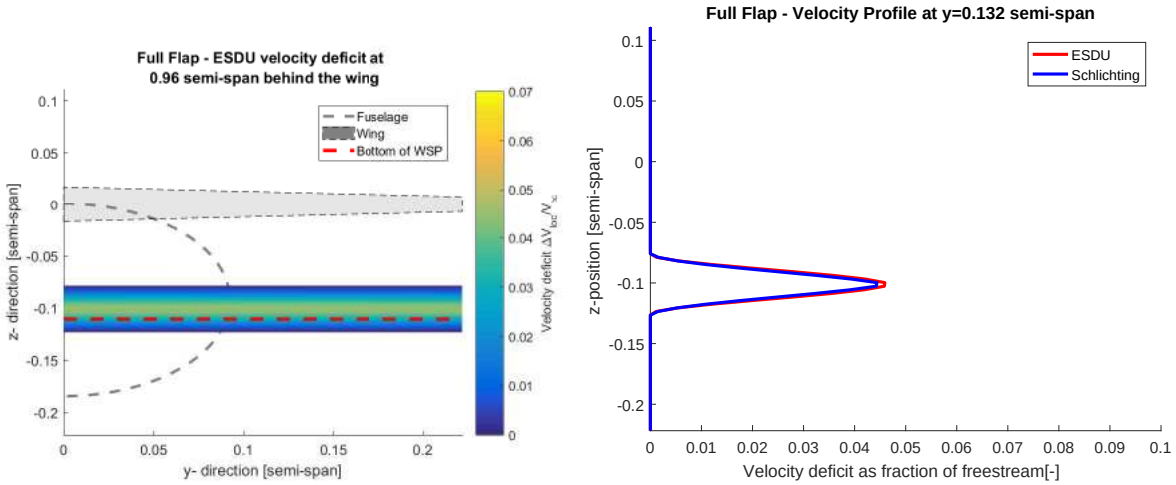


(a) Wake profile of the flapped wing, ESDU wake model

(b) Velocity profile of the flapped wing

Figure B.3: Results of the wake calculations for the full wing

### B.1.4. FLAP SCALE

Here the results of the scaled wing with flap are shown, in Figure B.4. The trend here is the same as for the full wing with flap, a reduction in angle of attack leads to a thinner wake, with a smaller velocity deficit, and located at a higher z-position.

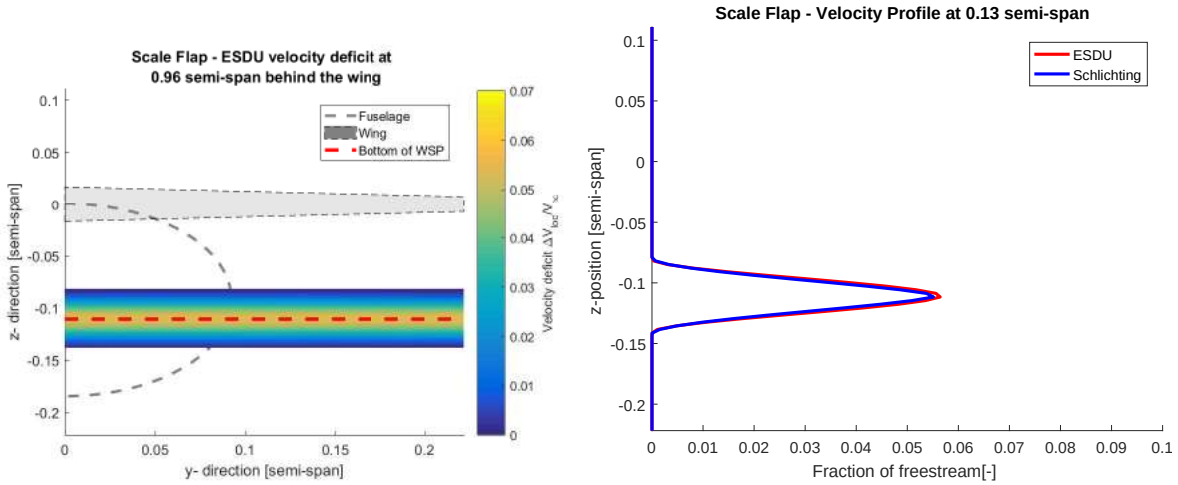


(a) Wake profile of the flapped wing, ESDU wake model

(b) Velocity profile of the flapped wing, at the wake survey plane

Figure B.4: Results of the wake calculations for the scaled wing

## B.2. ADDITIONAL OPTIMIZATION RESULTS

In this section additional graphs for the analysis of the optimized wings can be found.

### B.2.1. OPTIMIZATION WITH DRAG COEFFICIENT

Below are some further graphs from the optimization of the wing, with the drag in included. The results show some similarity to that of the non optimized wing, with the relative error increasing towards the tip. The spanwise lift distribution is slightly different for the scaled wing, with more outboard loading.

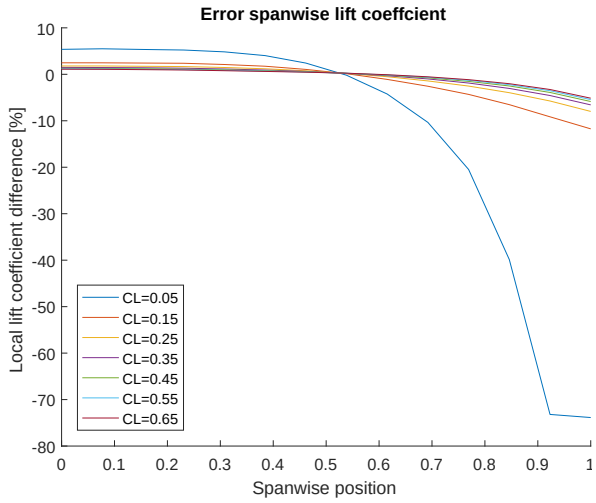


(a) The spanwise difference with fixed lift coefficient

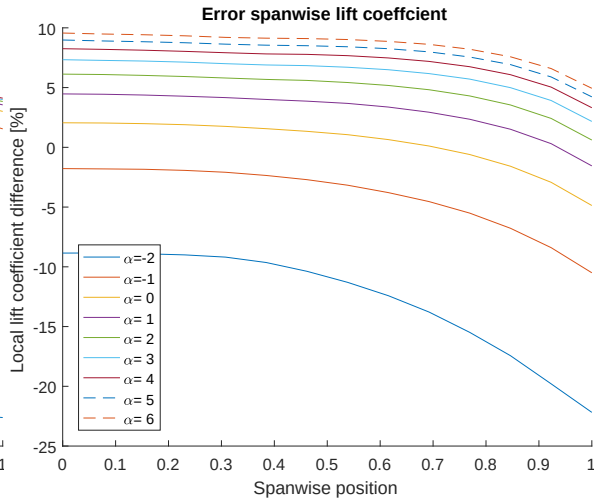


(b) The spanwise difference with fixed angle of attack

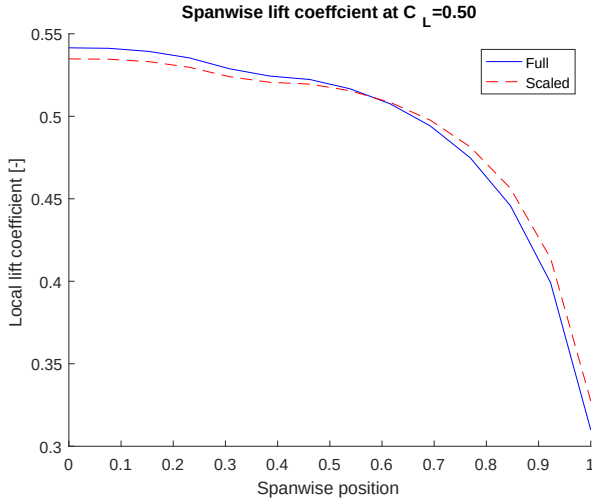


(c) Spanwise lift coefficient at fixed lift coefficient

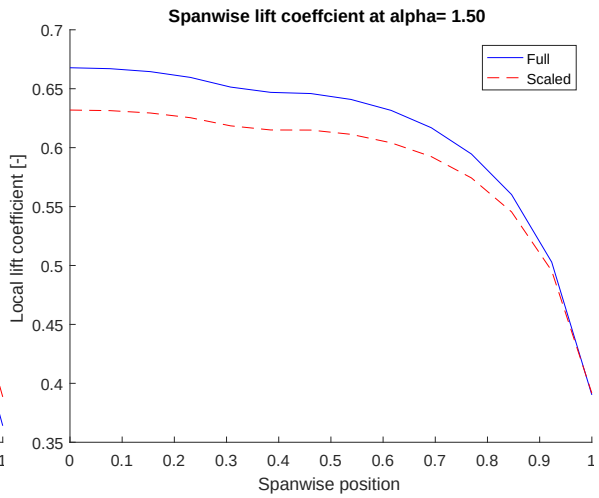


(d) Spanwise lift coefficient at fixed angle of attack

Figure B.5: Results of the optimization with drag

### B.2.2. OPTIMIZATION WITHOUT DRAG COEFFICIENT

The spanwise loading graphs are shown in Figure B.6. They are very similar to those found in Figure B.5, only that the relative errors are slightly smaller.

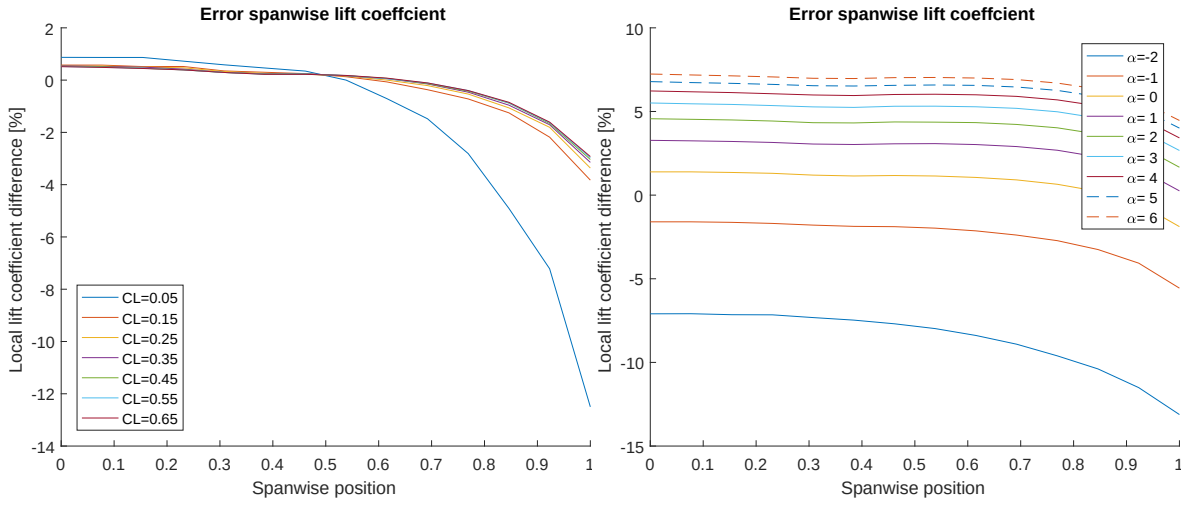


(a) The spanwise difference with fixed lift coefficient




(b) The spanwise difference with fixed angle of attack

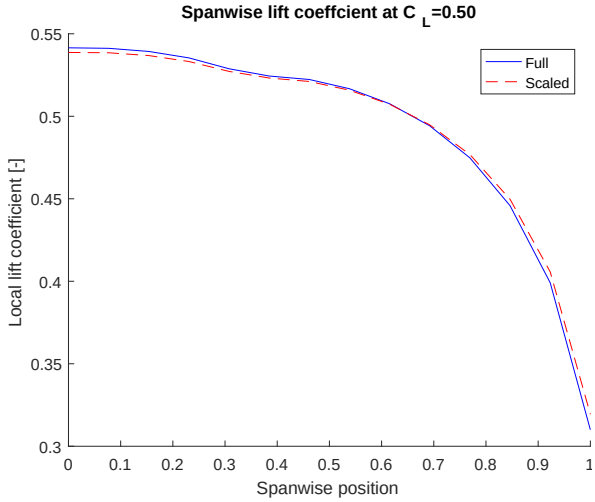


(c) Spanwise lift coefficient at fixed lift coefficient

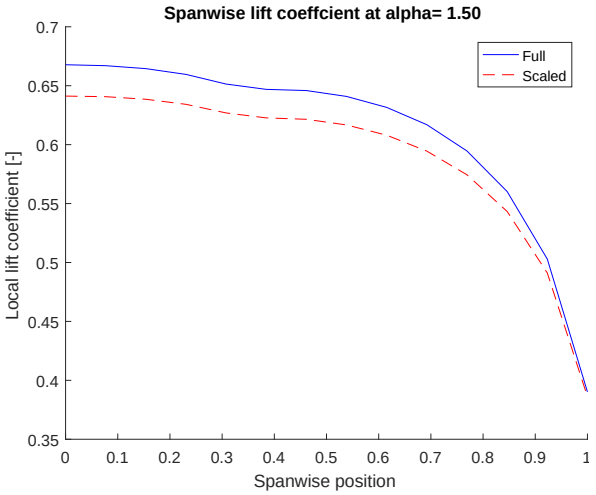


(d) Spanwise lift coefficient at fixed angle of attack

Figure B.6: Results of the optimization without drag

### B.2.3. THICKNESS OPTIMIZATION

Here further results of the thickness optimization can be found. Figure B.7c shows that the spanwise loading is different for the thinner wing, different also from the previous optimized wings, it shows a more distinct tip loading.

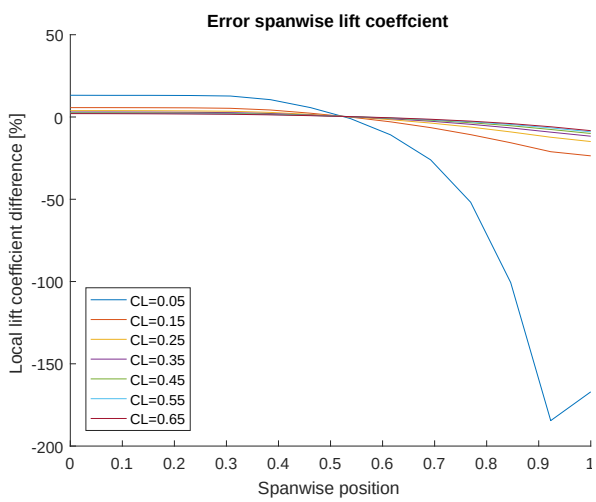


(a) The spanwise difference with fixed lift coefficient

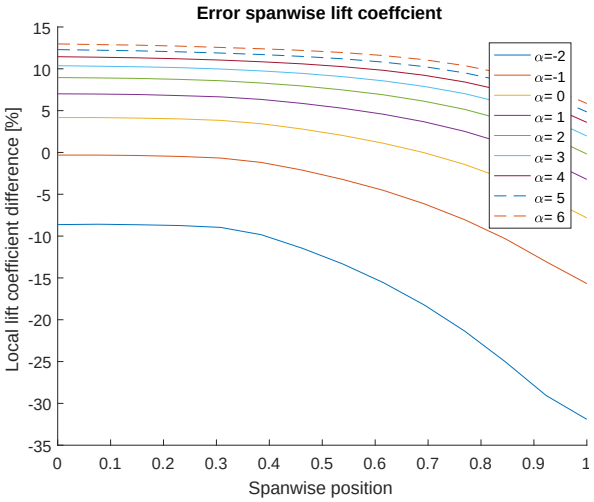


(b) The spanwise difference with fixed angle of attack

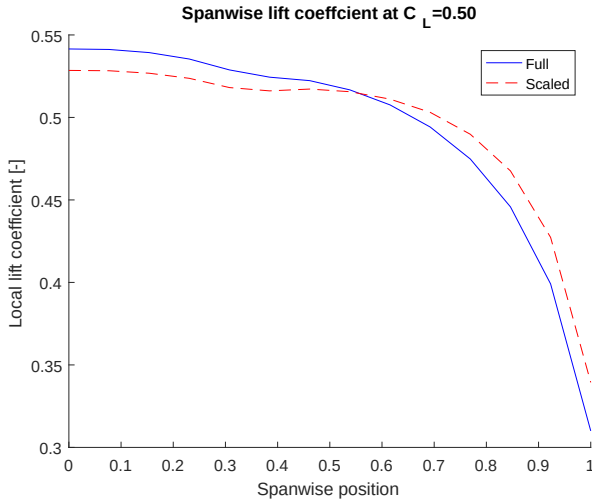


(c) Spanwise lift coefficient at fixed lift coefficient

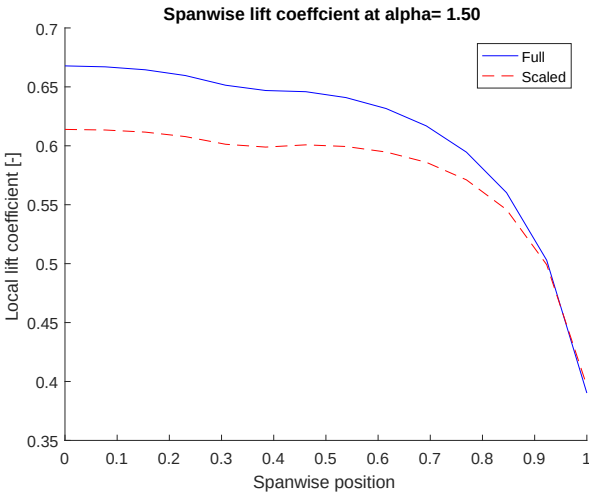


(d) Spanwise lift coefficient at fixed angle of attack

Figure B.7: Further results of the thickness optimization